The University Of Sheffield.

Department of Mechanical Engineering

Two-phase flow in straight pipes and across 90 degrees sharp-angled mitre elbows

Author:

WAMEEDH TURKI MOHAMMAD AL-TAMEEMI

Registeration No:130263351

Supervisors:

Dr. Pierre Ricco

Dr. Robert Woolley

A thesis submitted in partial fulfilment of the requirements for the degree of **Doctor of Philosophy**

June 2018

Abstract

Pressure drop of single-phase flow across 90° sharp-angled mitre elbows connecting straight circular pipes is studied in a bespoke experimental facility by using water and air as working fluids flowing in the range of bulk Reynolds number $500<\mathcal{R}e<60000$. To the best of our knowledge, the dependence on the Reynolds number of the pressure drop across the mitre elbow scaled by the dynamic pressure, i.e. the pressure-loss coefficient $\mathcal{K}$, is reported herein for the first time. The coefficient is shown to decrease sharply with the Reynolds number up to about $\mathcal{R}e$=20000 and, at higher Reynolds numbers, to approach mildly a constant $\mathcal{K}$=0.9, which is about 20% lower than the currently reported value in the literature. We quantify this relation and the dependence between $\mathcal{K}$ and the straight-pipe friction factor at the same Reynolds number through two new empirical correlations, which will be useful for the design of piping systems fitted with these sharp elbows. The pressure drop is also expressed in terms of the scaled equivalent length, i.e. the length of a straight pipe that would produce the same pressure drop as the elbow at the same Reynolds number.

Air-water flow in horizontal and vertical straight pipes and through 90° sharp-angled mitre elbows, is investigated visually by using high-speed high-resolution camera. The flow is studied in pipes with three diameters for about 600 conditions of air-water flows, characterized by superficial velocities in the ranges of j_L^*=0.297-1.015 m/s for water and j_G^*=0.149-33.99 m/s for air. The portion of the pipe upstream of the elbow is always positioned horizontally, while the portion of the pipe downstream of the elbow is oriented horizontally or vertically with the flow moving upward. Plug, slug, slug-annular and annular flows are observed in horizontal straight pipes, while slug, churn and annular regimes are recorded in vertical straight pipes. These flow patterns are well predicted by the Mandhane

et al. [1] map for horizontally oriented straight pipes and by the Hewitt and Roberts [2] map for vertically oriented straight pipes. The prediction of the flow patterns along the straight portions of the pipe improves by expressing the maps in non-dimensional form. The changes of the flow patterns as the fluids pass through the mitre elbows are thoroughly discussed. A multiple membrane flow structure is observed in the vertical upward flow at much higher Reynolds numbers, based on the water superficial velocity, than in the vertical downward case previously reported in the literature. The flow patterns through the elbows are expressed for the first time in terms of rescaled Mandhane et al. [1] maps, which simultaneously represent the flow patterns both upstream and downstream of the elbows. The dimensional analysis proves that a rigorous way to present the flow regimes of an incompressible isothermal air-water flow for a given geometry is a map in the space of the Reynolds numbers based on the superficial velocities of air and water for fixed Froude number.

The pressure drop generated by air-water flows was measured in horizontal and vertical straight pipes and across 90° sharp-angled mitre elbows for the same flow conditions of visual investigations.Two new pattern-based values of the Lockhart-Martinelli parameter $\mathcal{C}$ are found for the pressure drop in horizontal pipes with the presence of mitre elbows. A dimensional analysis is employed to scale the pressure drop data for straight pipes and across the elbows. New pattern-based empirical correlations are proposed to fit the scaled frictional pressure drops for the flows through the straight portions of the pipe and across the elbows.

The flow perturbation length upstream of the elbow is located at less than $32.5D^*$ for single-phase and two-phase flows, while the flow recovery length downstream of the elbow was less than $32.5D^*$ and $60D^*$ for single-phase and two-phase flows, respectively. The peripheral pressure upstream and downstream of the elbow is found to be axially symmetric farther than $7D^*$ upstream and downstream of the elbow for horizontal orientation in single-phase and two-phase flows.

Acknowledgements

This study has been conducted at the Department of Mechanical Engineering, The University of Sheffield, under the supervision of Dr. Pierre Ricco.

The study has been supported financially by the Iraqi Ministry of Higher Education and Scientific Research (MOHESR), which is gratefully acknowledged.

I would like to thank my supervisor Dr. Pierre Ricco for his advice and support along my study. His availability for fruitful research discussions and guidance during this period were a beneficial contribution to this study.

I would like to thank my second supervisor Dr. Robert Woolley for his advice and support.

Special thanks to the technicians in the Mechanical Engineering Department for their help and support along my experimental work, especially Mr. Malcolm Nettleship, Mr. Oliver Cooper, Mr. Jamie Booth, Mr. Michael Herbert and Mr. Ben Kitchener.

Last but not least, many thanks to my family for their support and patient along my study, and of course to my friends for their support along this time.

Thank you!

Contents

List of Figures

List of Tables

Nomenclature

A_1	Empirical parameter in Friedel's model	
A_2	Empirical parameter in Friedel's model	
A_3	Empirical parameter in Friedel's model	
$\mathcal{A}^*$	Pipe cross sectional area	m^2
Δl^*	Variation in length	m
Δp^*	Pressure drop	Pa
$\dot{m}^*$	Mass flow rate	kg/s
$\dot{V}^*$	Volumetric flow rate	m^3/s
$\mathcal{K}$	Elbow pressure-loss coefficient	
$\mathcal{C}$	Experimental constant	
$\mathcal{L}$	Equivalent length to diameter ratio l^*_{eq}/D^*	
$\mathcal{R}e$	Reynolds number	
$\mathcal{U}_b$	Mean-flow velocity	m/s
BSL	Best straight fit line	
D^*	Pipe diameter	m
De	Dean number	

Fr	Froude number	
FS	Full scale	
G^*	Mass velocity	$kg/m^2\,s$
g^*	Gravitational acceleration	m/s^2
$G^{'}$	Muller parameter	
j^*	Superficial velocity	m/s
p^*	Pressure	Pa
R^*	Bends curvature radius	m
u^*	Phase-velocity	m/s
U_b^*	Fluid bulk velocity	m/s
We	Weber number	
X	Martinelli parameter	
x	Gas-phase quality	
Y	Chisholm's parameter	
C	Elbow curvature ratio	
SLA	Second Law Analysis	

Greek symbols

α^*	Empirical parameter in Ito's correlations	
ϵ^*	Void fraction	
λ	Homogeneous volumetric void fraction	
μ^*	Viscosity	$Pa.s$
ν^*	Kinematic viscosity of the fluid	m^2/s
Φ	Two-phase pressure drop multiplier	

ρ^*	Density	kg/m^3
σ^*	Surface tension	N/m
θ^*	Bend's angle in Ito's correlations	

Scripts

f	Frictional
mom	Momentum
st	Head or level difference
tp	Two-phase
Ch	Chisholm
GO	Gas only
k	Flow phase
LO	Liquid only
n	Experimental constant in Chisholm's model
t	Turbulent
v	Viscous or laminar
Fri	Friedel
b	Bend
G	Gas-phase
L	Liquid-phase
av	Average
ch	Chordal
cs	cross-sectional
e	Elbow

eq	Equivalent
H	Homoheneous
mod	Modified
vol	Volumetric

Publications

Published papers

- W. Al-Tameemi and P. Ricco, "Pattern–based pressure drop of air–water flow across a 90° sharp mitre elbow," *Int. J. Comp. Meth. Exp. Meas.*, vol. 6, no. 1, pp. 198–207, 2018. [1]

- W. Al-Tameemi and P. Ricco, "Pressure-loss coefficient of 90 deg sharp-angled miter elbows," *ASME J. Fluids Eng.*, vol. 140, no. 6, p. 061102, 2018.

Submitted manuscripts

- Water-air flow in straight pipes and across 90 degrees sharp-angled mitre elbows. Submitted to the Int. J. Multiphase flow.

[1] This paper presented in the Wessex Institute 9th International Conference on Computational and Experimental Methods in Multiphase and Complex Flow and the paper has been chosen to publish in the Int. J. Comp. Meth. Exp. Meas instead of the conference transactions.

Chapter 1

Introduction

The importance of sharp-angled elbows

Two-phase flow is common in many industrial applications, such as refrigeration, chemical and oil industries. These systems employ many types of pipe fittings, like pipe bends, elbows, and sharp-angled elbows to direct the flow according to the system's route design. Bends are classified according to the ratio between the curvature radius of the bend and the pipe diameter $C{=}R^*/D^*$. (The symbol * henceforth indicates a dimensional quantity, while quantities with no symbols are dimensionless). Bends with curvature radii are classified as elbows or pipe bends, while they are identified as a mitre bends when two pipes join together without any curvature, as illustrated in Figure 1.1.

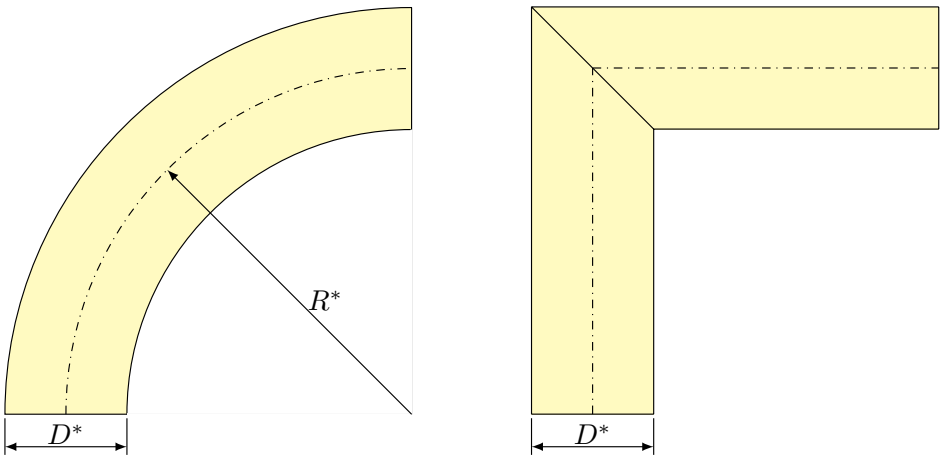

(a) Pipe bends and round elbows. **(b)** Sharp-angled mitre elbows.

Figure 1.1: Comparison between round elbows and sharp-angled mitre elbows.

Sharp-angled elbows are used in many applications due to the space limitations and, to achieve an optimum use of them, it is crucial to predict the pressure drop across these types of bends in single-phase and two-phase flows.

In single-phase flow, the prediction of the pressure drop across 90° sharp-angled mitre elbows is more complicated than that across round elbows because the additional pressure drop generated by the flow separation in 90° sharp-angled mitre elbows.

In two-phase flow, the interaction between the working fluids leads to form different regimes, which are known as flow patterns. The prediction of two-phase flow patterns through pipe fittings is important for the design of industrial piping systems because the flow regimes regulate relevant flow properties like pressure drop and heat transfer. The effect of mitre elbows on the flow patterns is expected to be more than the effect of round elbows because the flow separation in the mitre elbows.

Pressure drop of two-phase flow consists of three components, the pressure drop due to the change in elevation or head pressure drop Δp^*_{st}, which is called the static pressure drop, the pressure drop due to kinetic energy change as a consequence of phase change, which is known as the momentum pressure drop $\Delta p^*_{\mathrm{mom}}$, and the pressure drop due to the frictional forces between the flow and the pipe walls and between the working fluids Δp^*_{f}.

$$\Delta p^*_{\mathrm{tp}} = \Delta p^*_{\mathrm{st}} + \Delta p^*_{\mathrm{mom}} + \Delta p^*_{\mathrm{f}}. \tag{1.1}$$

The two-phase pressure drop across elbows is affected by many factors, such as the flow characteristics, like the phase velocities, physical properties of the working fluids and flow direction (upward or downward), the structural factors such as the pipe diameter D^*, curvature ratio C and the elbow orientation. The two-phase pressure drop across sharp-angled mitre elbows is expected to be more than that across round elbows because the pressure drop increases as the curvature ratio decreases.

Although there are many prediction models for two-phase pressure drop in straight pipes and across elbows, most of these methods are limited to special conditions

and cannot cover wide ranges of flow conditions. Furthermore, there is no available study in the literature has been conducted to investigate the behaviour of two-phase flow patterns through 90° sharp-angled mitre elbows and to predict the single-phase and two-phase pressure drop across these types of fittings.

This work studies the pressure drop of single-phase flow across 90° sharp-angled mitre elbows by employing air and water as working fluids at $500<\mathcal{R}e<60000$. Flow patterns are visualized in straight pipes and through the sharp elbows in horizontal and vertical orientations. Pressure drop measurements are employed along straight pipes and across mitre elbows to investigate the effect of the elbow on the two-phase pressure drop, to measure the perturbation length upstream and downstream of the elbow and to examine the effect of the elbow on the pressure distribution around the pipe periphery. New test facility has been designed and built for this work to accomplish the visual and the pressure measurements investigations.

Motivations

The motivations of this study are:

- There is no available study in the literature to investigate the single-phase pressure drop across 90° sharp-angled mitre elbows for $\mathcal{R}e<30000$.
- Flow pattern maps cannot predict the flow patterns accurately for different flow conditions and most of the available pattern maps were proposed in terms of dimensional parameters.
- There is no available study in the literature to investigate the behaviour of two-phase flow patterns across 90° sharp-angled mitre elbows.
- There is no reliable method in the literature to predict the two-phase pressure drop across 90° sharp-angled mitre elbows.
- Most of the two-phase pressure drop prediction models were proposed in terms of dimensional parameters without considering the effect of the flow patterns on the pressure drop of two-phase flow along straight pipes and across pipe fittings, like elbows and pipe bends.

Objectives

The objectives of this study are:

- Design and build a new test facility to study the pressure drop of single-phase and two-phase flows and to visualize the behaviour of two-phase flow patterns along straight pipes and through 90° sharp-angled mitre elbows for different flow conditions.

- Express the pressure loss coefficient of 90° sharp-angled mitre elbows in terms of $\mathcal{R}e$ in the range of $500<\mathcal{R}e<60000$.

- Investigate the two-phase flow patterns in straight pipes for horizontal and vertical orientations and express them in terms of non-dimensional pattern maps.

- Scaling the existed flow pattern maps of Mandhane et al. [1] and Hewitt and Roberts [2] in terms of non dimensional parameters by using simple dimensional analysis of Π theorem.

- Study the behaviour of two-phase flow patterns through the horizontal and horizontal to vertical 90° sharp-angled mitre elbows with upward flow and express the behaviour in terms of non-dimensional Mandhane et al. [1] maps.

- Investigate the pressure drop of two-phase flow along horizontal and vertical straight pipes and across the horizontal and horizontal to vertical 90° sharp-angled elbows with upward flow.

- Find appropriate values of the parameter $\mathcal{C}$ in Lockhart and Martinelli model to fit the scaled pressure drop data of two-phase flow along straight pipes with the presence of horizontal 90° mitre elbows in terms of Lockhart and Martinelli [5] multiplier for different flow patterns.

- Propose new pattern-based correlations for pressure drop of two-phase flow in straight pipes and across elbows for horizontal and vertical orientations in terms of non-dimensional parameters by using dimensional analysis Π theorem.

- Locate the flow perturbation length upstream and downstream of 90° sharp-angled mitre elbows for single-phase and two-phase flows in the horizontal and vertical orientations.

- Examine the effect of horizontal 90° sharp-angled mitre elbows on the pressure distribution at different angles (0°, 90°, and 270°) around the pipe periphery for single-phase and two-phase flows.

Thesis structure

The thesis is divided into eight chapters and three appendixes as follows: Chapter 2 illustrates the fundamentals and definitions of the two-phase flow parameters and flow patterns classification in horizontal and vertical straight pipes. Chapter 3 reviews the literature studies of single-phase flow across elbows, two-phase flow patterns, two-phase pressure drop measurements, the prediction maps of flow patterns and the two-phase pressure drop prediction models. The specifications of the experimental test facility, the experimental procedure and the uncertainty analysis are illustrated in Chapter 4.

The results and discussions of single-phase flow measurements are included in Chapter 5. Chapter 6 reviews the results and discussions of two-phase flow visualization in straight pipes and across 90° sharp-angled mitre elbows in horizontal and vertical orientations. The results and discussions of two-phase pressure drop measurements in straight pipes and across 90° sharp-angled mitre elbows for horizontal and vertical orientations are included in Chapter 7. The conclusions and the recommendations are found in Chapter 8.

Three appendixes are added at the end of the thesis. Appendix A reviews the prediction results of single-phase and two-phase pressure drop in straight pipes and across 90° round elbows. Appendix B depicts the calibration data of the measurement instruments, while Appendix C illustrates the dimensional analysis, which are used to scale the experimental data for two-phase flow and two-phase pressure drop in straight pipes and across 90° sharp-angled mitre elbows.

Chapter 2

Fundamentals and definitions of two-phase flow

This Chapter illustrates the two-phase flow fundamentals and definitions.

Fundamentals and definitions

Gas-phase quality:

Gas-phase quality x is defined as the ratio between the mass flow rate of the gas-phase and the total mass flow rate. The gas-phase quality varies from zero for liquid only flow to one for gas only flow.

$$x = \frac{\dot{m}_{_G}^*}{\dot{m}_{_G}^* + \dot{m}_{_L}^*}, \tag{2.1}$$

where $\dot{m}_{_G}^*$ is the gas-phase mass flow rate and $\dot{m}_{_L}^*$ is the liquid-phase mass flow rate.

Void fraction:

Void fraction ϵ is used to express the gas-phase ratio in the two-phase flow geometry such as chordal (ch), cross-sectional (cs) and volumetric (vol) as:

$$\epsilon_{\text{ch}} = \frac{l_{_G}^*}{l_{_G}^* + l_{_L}^*}, \tag{2.2}$$

where $l_{_G}^*$ is the length of the gas-phase and $l_{_L}^*$ is the length of the liquid-phase.

$$\epsilon_{\text{cs}} = \frac{\mathcal{A}_{_G}^*}{\mathcal{A}_{_G}^* + \mathcal{A}_{_L}^*}, \tag{2.3}$$

where $\mathcal{A}_G^*$ and $\mathcal{A}_L^*$ are the cross-sectional areas occupied by the gas-phase and the liquid-phase respectively.

$$\epsilon_{\text{vol}} = \frac{V_G^*}{V_G^* + V_L^*}, \tag{2.4}$$

where V_G^* and V_L^* are the volume flow rates of the gas-phase and the liquid-phase respectively. The cross-sectional void fraction ϵ_{cs} is the most common used definition in two-phase flow, which can be estimated by using different methods.

Two-phase velocity:

The phase velocity in two-phase flow is defined according to the assumption of the two-phase flow phenomena.

- Mass velocity: The mass velocity G_k^* of the phase k is defined as the ratio between the mass flow rate and the cross-sectional area:

$$G_k^* = \frac{\dot{m}_k^*}{\mathcal{A}^*}, \tag{2.5}$$

  where $\dot{m}_k^*$ is the mass flow rate of the phase k, and $\mathcal{A}^*$ is the cross-sectional area of the pipe. The total mass velocity of the two-phases is equal to the summation of the mass velocities for the liquid-phase G_L^* and the gas-phase G_G^*.

- Superficial velocity: The superficial velocity is defined as the ratio between the volume flow rate of the fluid-phase and the whole cross-sectional area of the pipe as:

$$j_k^* = \frac{\dot{V}_k^*}{\mathcal{A}^*}, \tag{2.6}$$

$$j_L^* = \frac{\dot{V}_L^*}{\mathcal{A}^*}, \qquad j_G^* = \frac{\dot{V}_G^*}{\mathcal{A}^*}, \tag{2.7}$$

  where $\dot{V}_k^*$ is the volumetric flow rate of the phase k.

- Mixture velocity: This velocity is known as the ratio between the total volumetric flow rate and the pipe cross-sectional area:

$$U_{tp}^* = \frac{\dot{V}^*}{\mathcal{A}^*} = j_L^* + j_G^*. \tag{2.8}$$

- Average velocity: This velocity is defined as ratio between the volumetric flow rate $\dot{V}_k^*$ of the phase k and the area of the pipe which is occupied by the phase $\mathcal{A}_k^*$:

$$U_{k,av}^* = \frac{\dot{V}_k^*}{\mathcal{A}_k^*}, \tag{2.9}$$

$$U_{G,av}^* = \frac{\dot{V}_G^*}{\mathcal{A}^* \epsilon_{\text{cs}}^*}, \qquad U_{L,av}^* = \frac{\dot{V}_L^*}{\mathcal{A}^* (1 - \epsilon_{\text{cs}}^*)}. \tag{2.10}$$

Reynolds number:

Reynolds number $\mathcal{R}e$ is defined as the ratio between the inertial and viscous forces:

$$\mathcal{R}e = \frac{\rho^* U_b^* l^*}{\mu^*}, \tag{2.11}$$

where ρ^* is the fluid density, U_b^* is the fluid bulk velocity and l^* is the length while μ^* is the fluid kinematic viscosity. For pipe flow, $\mathcal{R}e$ is defined in terms of pipe diameter D^* as:

$$\mathcal{R}e = \frac{\rho^* U_b^* D^*}{\mu^*}. \tag{2.12}$$

In two-phase flow, $\mathcal{R}e$ is defined in terms of superficial velocities as:

$$\mathcal{R}e_k = \frac{\rho_k^* j_k^* D^*}{\mu_k^*}, \tag{2.13}$$

where the subscript k=L for liquid-phase and k=G for gas-phase. Another definition of the two-phase flow $\mathcal{R}e$ is given in terms of mass velocity G^* as:

$$\mathcal{R}e_k = \frac{G_k^* D^*}{\mu_k^*}. \tag{2.14}$$

Froude number:

Froude number Fr represents the ratio between the inertia force and the gravity, and it can be defined for single-phase flow as:

$$Fr = \frac{\mathcal{U}_b^*}{\sqrt{g^* l^*}}, \tag{2.15}$$

where $\mathcal{U}_b^*$ is the flow velocity, g^* is the gravitational acceleration and l^* is the unit length and it is equal to the pipe diameter D^* in pipe flow. For two-phase pipe flow, Fr_k for the phase k is defined in terms of superficial velocity j_k^* as:

$$Fr_k = \frac{j_k^*}{\sqrt{g^* D^*}}. \tag{2.16}$$

Weber number:

Weber number for single-phase flow is defined as the ratio between the inertia force and the surface tension as:

$$We = \frac{\rho^* \mathcal{U}_b^{*2} D^*}{\sigma^*}, \tag{2.17}$$

where σ^* is the surface tension of the working fluid. In two-phase flow We_k for the phase k is defined in terms of superficial velocity j_k^* as:

$$We_k = \frac{\rho_k^* j_k^{*2} D^*}{\sigma^*}. \tag{2.18}$$

Dean number:

Dean number De is known for single-phase flow as the ratio between the viscous force and inertia of the flow in curved pipes:

$$De = \frac{\rho^* \mathcal{U}_b^* D^*}{\mu^*} \sqrt{\frac{D^*}{2R^*}} = \mathcal{R}e \sqrt{\frac{D^*}{2R^*}}, \tag{2.19}$$

where R^* is the curvature radius of the bend or the elbow. In two-phase flow, De_k of the phase k is defined in terms of $\mathcal{R}e_k$ as:

$$De_k = \mathcal{R}e_k \sqrt{\frac{D^*}{2R^*}}. \tag{2.20}$$

Two-phase flow patterns

The structure of the two-phase flow in the flow region is known as the flow patterns. In pipe flow, different flow patterns could form and their types depend on many conditions, like the pipe diameter D^*, the physical properties of the working fluids, the flow direction and the flow rates of the fluids. The wellknown flow regimes in horizontal and vertical pipes are illustrated in this Section.

Flow patterns in horizontal pipes

The common observed flow patterns in horizontal pipe flow, which are shown in Figure 2.1, are:

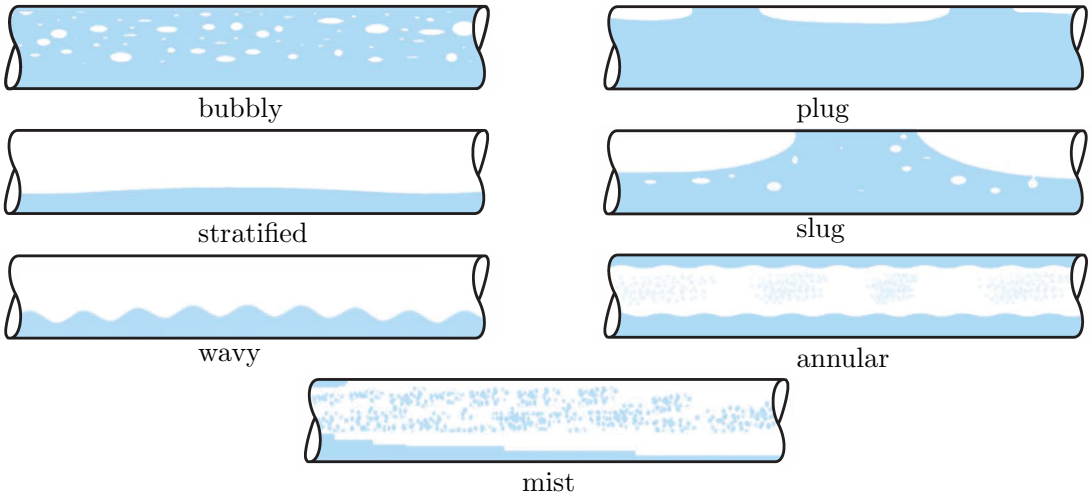

Figure 2.1: Flow patterns in horizontal pipe flow [6]

- Bubbly flow: This type of flow is usually recognized at high liquid-phase flow rates and low gas-phase flow rates. Gas bubbles occupy the top side of the pipe because of the density difference between the phases.

- Stratified flow: This regime forms when both liquid and gas phases flow at low flow rates. The gas-phase flows at the top side of the pipe separated from the liquid-phase, because the effect of the gravity.

- Stratified wavy flow: When the gas-phase flow rate in stratified flow increases slightly more than the liquid-phase flow rate, the liquid flow at the bottom of the pipe forms waves with different amplitudes, which is known as stratified wavy flow. The amplitude of the liquid waves depends on the velocity difference between the phases, and it cannot reach to the top wall of the pipe.

- Intermittent flow: This pattern forms at further increase in the gas-phase flow rate relative to the liquid-phase flow rate of the stratified wavy flow. This increase in the gas-phase flow rate leads to an increase in the amplitude of the liquid-phase waves until they touch the top wall of the pipe. The intermittent flow can be classified into two different flow patterns:

    1. Plug flow: This regime is distinguished as elongated bubbles flowing at the top side of the pipe due to the gravity, while the liquid-phase flows at the bottom side of the pipe. The length and the diameter

of the bubbles are controlled by the flow conditions, nevertheless, the bubble diameter is always smaller than the pipe diameter.

2. Slug flow: At higher gas-phase flow rates, the elongated bubbles of plug flow change to a gas-phase slugs separated by liquid-phase slugs, forming the slug flow regime. The diameter of the gas-phase slugs in this flow pattern is approximately equal to the pipe diameter. Gas-phase slugs move at the top side of the pipe separated from the bottom wall of the pipe by a thin liquid-phase layer. This type of flow is not stable and not recommended in many two-phase flow applications.

- Annular flow: At very high gas-phase flow rates and low liquid-phase flow rates, the flow of gas-phase occupies the core of the pipe surrounded by a thin layer of liquid-phase which is known as annular flow. The thickness of the liquid layer at the bottom side of the pipe is larger than the upper layer due to the gravity. This regime is stable and recommended in many two-phase flow applications.

- Mist flow: At very high gas-phase flow rates, the liquid layers of the annular flow separate from the pipe walls as small liquid-phase droplets flowing in a continuous gas-phase, to form the mist flow.

Flow patterns in vertical pipes

In two-phase flow through a vertical pipe, the effect of the gravity and the buoyancy generates many differences between the flow patterns of the horizontal and the vertical pipe flows. Figure 2.2 depicts the common observed flow patterns in vertical pipe flow.

- Bubbly flow: This regime is generated at very low gas-phase flow rates and high liquid-phase flow rates. The gas-phase bubbles take a spherical shape with different sizes much smaller than the pipe diameter.

- Slug flow: At higher gas-phase flow rates, the bubbles size increases to generate gas-phase slugs separated by liquid-phase slugs, which is known as slug flow. The diameter of the gas-phase slugs is approximately equal

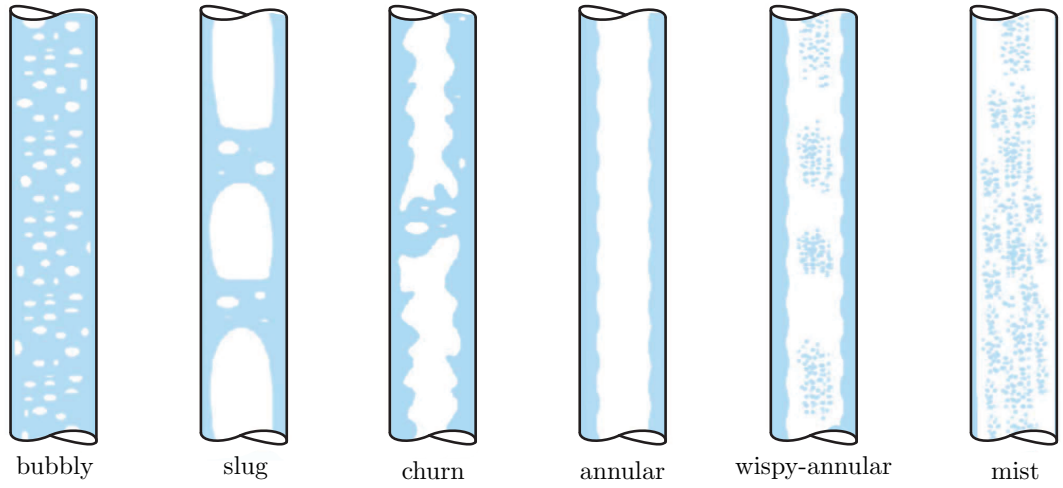

Figure 2.2: Flow patterns in vertical pipe flow [6]

to the pipe diameter and they flow at the centre of the pipe with a thin liquid layer between them and the pipe wall. The liquid-phase slugs in this regime may include some small bubbles.

- Churn flow: This regime represents a transition regime between the slug and the annular flows. The flow is recognised as an up and down oscillating motion of the liquid layer between the gas-phase slugs and the pipe wall, during the general flow.

- Annular flow: The only difference between the annular flow in vertical and horizontal pipes is the thickness of the liquid-phase layers around the gas-phase core. The liquid layer at the bottom side of the pipe in horizontal flow is thicker than the top layer due to the gravity, while the layers in vertical pipe flow are symmetric around the flow axis.

- Mist flow: At further increase in the gas-phase flow rate of the annular flow, the liquid-phase layers separate from the pipe walls and form a small liquid droplets flow within the continuous gas-phase flow, which is known as a mist flow.

Chapter 3

Literature review

This Chapter reviews the studies of single-phase and two-phase flows through different pipe fittings. Section 3.1 includes the investigations of single-phase pressure drop across elbows. The two-phase flow visualization studies are found in Section 3.2, while the two-phase pressure drop investigations are included in Section 3.3. Section 3.4 illustrates the prediction maps of flow patterns in adiabatic two-phase flow and the prediction models of two-phase pressure drop.

Single-phase flow through elbows and pipe bends

Pipe fittings like elbows and pipe bends are essential in many industrial applications and the estimation of the pressure drop across these fittings is crucial in piping systems design. The prediction of the pressure losses across elbows and pipe bends is more complicated than the straight pipe flow because the local pressure drop across these fittings is affected by the additional factors generated by the elbows, like the secondary flow and the flow separation [7]. The pressure drop across the elbows augments with the decrease of the elbow's curvature ratio $C{=}R^*/D^*$, where R^* is the curvature radius of the elbow and D^* is the pipe diameter [8]. Sharp-angled mitre elbows generate more local pressure drop than the round elbows because the even more intense flow separation [9, 10].

Numerous studies in the literature have investigated the pressure loss across round elbows in terms of pressure loss coefficient $\mathcal{K}$. Schmandt and Herwig [11] used the numerical simulation (Second Law Analysis SLA) method and experimental

investigations to examine the validity of the SLA-model in computing the pressure loss coefficient $\mathcal{K}$ of 90° round elbows with square cross section for laminar flow conditions at $\mathcal{R}e$<200. The study proved that this numerical method can be employed to evaluate $\mathcal{K}$ of pipe fittings accurately. Schmandt and Herwig [12] proved that the pressure loss coefficient in 90° round elbow is a function of Reynolds number $\mathcal{R}e$ for steady and unsteady laminar flows for $\mathcal{R}e$<200. Ito [13] proposed an empirical model to evaluate the pressure loss coefficient of smooth pipe bends for turbulent flow depending on many factors, like the bend angle, the curvature radius, the pipe diameter and the flow Reynolds number $\mathcal{R}e$ as:

- For $\mathcal{R}e\,(D^*/2R^*)^2 < 91$:

$$\mathcal{K} = 0.00068967\ \alpha^*\ \theta^*\ \mathcal{R}e^{-0.2}\ \left(\frac{2R^*}{D^*}\right)^{-0.9}. \tag{3.1}$$

- For $\mathcal{R}e\,(D^*/2R^*)^2 > 91$:

$$\mathcal{K} = 0.00241\ \alpha^*\ \theta^*\ \mathcal{R}e^{-0.17}\left(\frac{2R^*}{D^*}\right)^{0.84}, \tag{3.2}$$

where R^* is the curvature radius, D^* is the pipe diameter, θ^* is the angle of the bend and α^* is an empirical parameter and it can be evaluated depending on the curvature ratio of the bend $2R^*/D^*$ as:

- For $(2R^*/D^*)$ <19.7:

$$\alpha^* = 0.95 + 17.2(2R^*/D^*)^{-1.96}. \tag{3.3}$$

- For $(2R^*/D^*)$ >19.7:

$$\alpha^* = 1. \tag{3.4}$$

The elbow equivalent length l^*_{eq}, which is the length of a straight pipe that would produce the same pressure drop as the elbow at the same flow conditions, represents another way to express the pressure drop across elbows and pipe bends. Based on wide ranges of experimental data for different working fluids, Wilson et al. [14] expressed the pressure drop across 90° round elbow with C=1 in terms of the ratio between the equivalent length of the elbow and the pipe diameter

$\mathcal{L}$=l^*_{eq}/D^* for wide range of laminar and turbulent flow conditions. In laminar flow, the $\mathcal{L}$ is highly affected by the Reynolds number, while this effect is negligible in turbulent flow conditions. The study showed that $\mathcal{L}$ varies between 20 and 30 for $\mathcal{R}e$>2000. Depending on experimental data, Beij [15] proposed a graphical model to predict the equivalent length to diameter ratio $\mathcal{L}$ of 90° round elbows in terms of the curvature ratio of the bend C as shown in Figure 3.1. Perry [16]

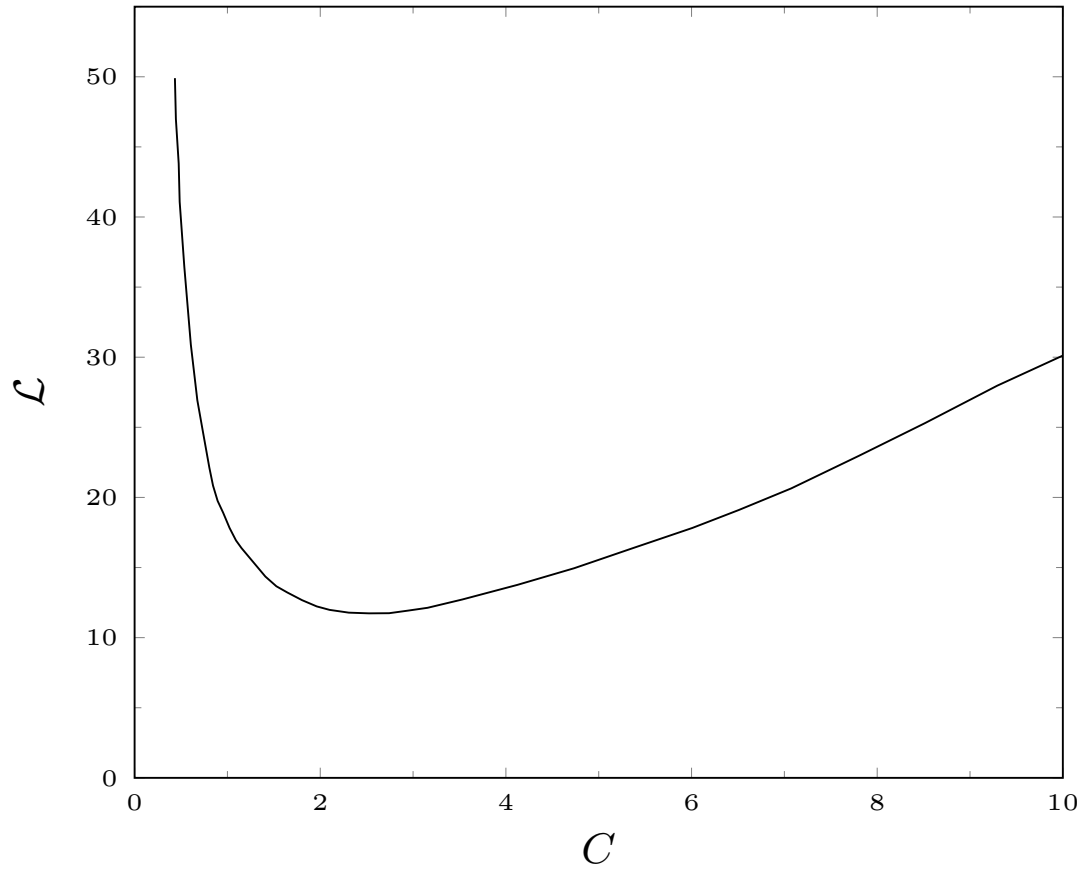

Figure 3.1: Equivalent length to diameter ratio for bends in terms of curvature ratio $C = R^*/D^*$ [15]

suggested that the value of $\mathcal{L}$ for 90° round bends is varied between 20 and 60 for turbulent flow conditions. Depending on experimental data, Spedding et al. [17] found that the $\mathcal{L}$ ratio of 90° round bend with C=0.65 varies between 43 and 60 for different turbulent flow conditions. Crawford et al. [9, 10] found that the $\mathcal{L}$ ratio of 90° sharp-angled elbow (they used a T shape junction with one blocked end) is approximately equal to 43 for turbulent flow conditions. Further more, the study proposed an empirical correlation to fit the experimental data of the pressure drop across 90° round elbows with small curvature ratios C for

turbulent flow as:

$$\mathcal{L} = 2.4792\,\mathcal{C}_f\,\mathcal{R}e^{0.25}\left(\frac{2R^*}{D^*}\right) + 1.25\left(\frac{2R^*}{D^*}\right)^{-1.5}\mathcal{R}e^{0.35}, \tag{3.5}$$

where $\mathcal{C}_f$ if the Darcy friction factor of straight pipes, which is computed for the same flow conditions.

Although there are many researchers studied the single-phase pressure drop across 90° round elbows, only three researchers have presented experimental results in sharp-angled mitre elbows. Kirchbach [18] studied the pressure drop across single and multiple smooth mitre elbows for turbulent water flow at $\mathcal{R}e$>28000. The study found that the pressure loss coefficient is a function of the elbow angle for this range of $\mathcal{R}e$, and it is approximately equal to 1.1 for 90° sharp-angled mitre elbow. Further investigations were conducted by Schubart [19] to examine the effect of the surface roughness on the pressure drop of the turbulent flow across mitre elbows for $\mathcal{R}e$>20000. The study reported some increase in the pressure loss coefficient for rough elbows than the smooth ones. For the 90° sharp-angled mitre elbows there is no significant difference in the $\mathcal{K}$ values between the smooth and the rough surface for $\mathcal{R}e$<60000 (the range of interest in the present study). The pressure loss coefficient of mitre elbows for compressible air flow expressed by Haidar [20] in terms of elbow's angle. The study proposed an empirical correlation to fit the experimental data of pressure loss coefficient in terms of elbow's angle. By using STAR-CD computational fluid dynamics, Moujaes and Aekula [21] investigated the pressure distribution of turbulent air flow through a 90° sharp-angled mitre duct with a rectangular cross section. The study found that the pressure loss coefficient $\mathcal{K}$ varies between 1.22 and 1.3 for $\mathcal{R}e$>10^5.

Books on fluid mechanics, for example Munson et al. [22], White [23], and Rennels and Hudson [24], and engineering manuals, for example Crane [25], rely on Kirchbach [18]'s and Schubart [19]'s data and do not report any dependence of the pressure-loss coefficient of 90° mitre elbows on the bulk Reynolds number $\mathcal{R}e$. Crane [25] used the experimental data of Kirchbach [18] to correlate the pressure-loss coefficient with the friction factor in straight pipes at the same Reynolds number.

It is evident that there is a dearth of studies relating minor pressure-loss coefficients for pipe fittings, especially 90° sharp-angled mitre elbows, with the Reynolds number. A symptomatic sentence on this point is found in White [23]: "Although $\mathcal{K}$ is dimensionless, it is often not correlated in the literature with the Reynolds number...".

In the present work, we have carried out an experimental investigation of the pipe flow through 90° sharp-angled circular mitre elbows by varying the bulk Reynolds number $\mathcal{R}e = \mathcal{U}_b^* D^*/\nu^*$ (where $\mathcal{U}_b^*$ is the mean velocity and D^* is the pipe diameter) between 500 and 60000. Both air and water have been utilized as working fluids in the same experimental facility and we have employed three diameters for each fluid.

Two-phase flow visualization

This Section reviews the visual investigations of the flow patterns behaviour through different types of pipe bends and elbows. The flow patterns observations studies are reviewed in Section 3.2.1, while the investigations of the influence of the gravity and the centrifugal force on the flow patterns are found in Section 3.2.2. Studies of the flow patterns behaviour through different types of bends and the flow perturbation length location due to the elbow are reviewed in Section 3.2.3.

Flow patterns observations

The identification of the flow patterns is important in two-phase flow systems design because the flow patterns control the local pressure drop and heat transfer [26]. Numerous studies have been conducted to identify the two-phase flow patterns, with the presence of elbows and pipe bends, and express them graphically in terms of different parameters as flow patterns maps.

Six flow patterns (bubbly, stratified, plug, slug, wavy and annular) were observed by Usui et al. [27, 28, 29] for air-water flow through vertical C-shaped 180° bends. The observed flow patterns were expressed in flow patterns maps in terms of j_L^* and j_G^* for upward and downward flows.

Gas-water and air-water Upward and downward flows through a vertical 180°

bends with ∪ and ∩ shapes were employed by Takemura et al. [30] to investigate the behaviour of the flow regimes across the bends for different flow conditions. Four flow patterns (bubbly, slug, annular and froth) were observed and expressed in pattern maps in terms of liquid-phase and gas-phase superficial velocities.

Five patterns (bubbly, dispersed, intermittent, stratified and annular) were observed by Wang et al. [31, 32] in air-water flow through a horizontal 180° bends with different curvature ratios C. The observed regimes were expressed in diameter-based flow pattern maps in terms of j_L^* and j_G^* for different flow conditions. The maps illustrate the effect of the bends curvature ratios C on the transition zones between annular and stratified regimes.

Six flow patterns (stratified-wavy, slug-stratified wavy, intermittent, annular, dry out and mist) were identified visually by Da Silva Lima [33] in refrigerant R-134a two-phase flow through a horizontal and vertical C-shaped 180° bends with upward and downward flows for different flow conditions. The study reported that the observed flow patterns through the bends were similar to the flow regimes in straight pipes with minor differences due to the bend. Padilla et al. [34] remarked three flow patterns (slug, intermittent and annular) in two-phase refrigerant R-1234yf downward flow through vertical C-shape 180° bends. The flow visualization data at the entrance of the bend have good agreement with Wojtan et al. [35]'s flow patterns map.

Visual investigations by De Oliveira et al. [36] distinguished three patterns (stratified, intermittent and annular) in refrigerant R-134a two-phase flow through 180° bends. The flow regimes are well expressed in terms of Wojtan et al. [35]'s flow patterns map.

A study by Saidj et al. [37] used air-water two-phase flow to investigate the effect of horizontal to vertical 90° bend with upward flow on two-phase flow patterns. Three different flow regimes were recognized in the horizontal portion of the pipe upstream of the bend (plug, slug and stratified wavy) and two different patterns in the vertical portion of the pipe downstream of the bend (slug and churn). The study showed that the length of the air slugs increased downstream of the bend.

Hsu et al. [38] remarked three patterns (slug, stratified and stratified wavy) in air-water flow through 90° round elbow by using different elbow diameters, cur-

vature radii and different orientations. Ma et al. [39] employed power spectral density (PSD) and multiscale entropy (MSE) techniques to identify air-water flow patterns through vertical C-shape 180° bend for different air and water superficial velocities in upward and downward flow orientations. Five flow regimes (plug, stratified, slug, annular and dispersed) were observed for upward and downward flows and expressed in flow pattern maps in terms of air and water superficial velocities. Dang et al. [40] distinguished five regimes (bubbly, plug, slug, pseudo slug and stratified) in air water flow across 90° round elbow for different flow conditions. The observed patterns are well presented in terms of Mandhane et al. [1] map.

The effect of gravity and centrifugal forces on two-phase flow patterns

The effect of the gravity and the centrifugal force on two-phase flow patterns through pipe bends has been reported by many researchers for different bends orientations.

Usui et al. [27, 28, 29] proposed a modified Froude number Fr_{mod} to express the domination forces on the air-water flow through vertical C shape bends for upward and downward flows. The study showed that gravity overcame the centrifugal force for (Fr_{mod}<1), the centrifugal force is the dominant for (Fr_{mod}>1) and both forces have equivalent action for (Fr_{mod}=1). Takemura et al. [30] studied the effect of gravity and centrifugal force on upward and downward air-water flows through a vertical 180° bends with ∪ and ∩ shapes. They identified the ranges of flow conditions to dry the top surface of the ∩-shape bends and the inner wall of the ∪-shape bends, due to the gravity, and express them in terms of superficial velocities of the working fluids.

Da Silva Lima [33], Da Silva Lima and Thome [41] investigated the effect of the gravity and the centrifugal forces on two-phase refrigerants flow through 180° bends visually. The studies found that the influence of the centrifugal force on the flow patterns through the bend was more than the effect of the gravity, for the employed flow conditions in these studies. Padilla et al. [34] used the gas-phase Froude number Fr_{G} to express the effect of the gravity and the centrifugal force

on two-phase refrigerants R-410A, R-134a and R-1234yf flows across 180° bend. The study reported that the centrifugal force overcomes the gravity for $Fr_G \gg 1$, while the gravity effects the patterns more than the centrifugal force for $Fr_G \ll 1$, similar to the results of Usui et al. [27, 28, 29].

Flow patterns behaviour through elbows and pipe bends

The action of different factors on the two-phase flow through elbows and pipe bends, like the flow separation, the secondary flow and the gravity, perturbs the flow patterns through the elbow. Consequently, different phenomenon of the two-phase flow behaviour through elbows and pipe bends have been distinguished by many researchers for horizontal and vertical orientations.

Flooding and reverse flow, water-phase flow downward in general upward two-phase flow, reported by Usui et al. [27], Luo and Wu [42] and Wang et al. [43] for air-water flow through vertical C-shape 180° bends with upward flow and by Hsu et al. [38] for air-water flow through horizontal to vertical 90° round elbow with upward flow. These phenomena were not observed in downward flows for the same flow conditions.

Chen et al. [44, 45], Wang et al. [32, 43] and Wang et al. [46] found that the stratified flow regime changes suddenly to annular through horizontal and vertical 180° bends with low curvature ratios, because the centrifugal force overcomes the effect of the gravity.

The air slug division has been reported by Chen et al. [44], Luo and Wu [42] and Wang et al. [43] through a vertical ∪ shape 180° bends, and by Hsu et al. [38] through a 90° round elbows with upward flow. The divided bubbles coalesce downstream of the elbow and form a membrane flow, which is a two-phase flow structure defined by Milan et al. [47] in a vertical downward flow, for different flow conditions.

The increase in the slug velocity through the bends has been reported by Luo and Wu [42] for air-water flow through a vertical ∪ shape 180° bends and by Hsu et al. [38] for a 90° round elbows with upward flow.

Flow perturbation length

The location of the flow perturbation length, i.e. the length required by the flow to recover the patterns observed well upstream of the bend, or the distance upstream of the bend, downstream of the bend where the flow is not affected by the bend, represents an important aim of many studies. Although there is no available study in the literature to locate the perturbation length duo to the presence of 90° sharp-angled mitre elbows, many studies have been conducted to find the perturbation length upstream and downstream of round elbows and pipe bends by using visual investigations.

Kim et al. [48] studied air-water bubbly flow through a horizontal 90° elbows visually. The study found that the perturbation length is 43.9 times the pipe inside diameter D^* downstream of the elbow. Da Silva Lima [33] and Da Silva Lima and Thome [41] reported that the effect of 180° bends on refrigerant R-134a two-phase flow lasts longer downstream of the bend, in vertical orientation with downward flow, than horizontal and vertical orientation with upward flow. The studies did not remark any effects on the flow patterns upstream of the bends for all orientations. De Kerpel et al. [49] investigated the refrigerant R-134a two-phase flow through vertical ∪ shape return bend to locate the flow recovery length downstream of the bend. The experimental results showed that the effect of the elbow on the flow patterns lasted up to 30 times the pipe diameter D^* downstream of the bend. An experimental study by Padilla et al. [34] used two-phase refrigerants (R-1234yf, R-410A and R-134a) flows across C-shape 180° bends with downward flow to locate the flow perturbation length upstream and downstream of the bend. The maximum perturbation length upstream and downstream of the bend were located at $10D^*$ and $20D^*$ respectively. De Oliveira and Barbosa [50] used air-water flow through vertical C-shape 180° bend with different curvature ratios for wide range of upward and downward flow conditions to examine the effect of the bend on the frictional pressure drop. The effect of the bend on the two-phase pressure was located at $15D^*$ upstream of the bend for upward and downward flows, while the effect lasts farther than the last measurement station at about $71D^*$ downstream of the bend. Yadav and Kim [51] and Yadav et al. [52] found that the distribution of bubbles in air-water flow through a vertical 90°

bend with upward flow was not affected farther than 16 and 33 times the pipe diameter D^* upstream and downstream of the bend, respectively.

Despite the extensive literature in the field, there is no study investigating the influence of 90° sharp-angled mitre elbows on two-phase flow patterns. In this work, we are therefore motivated to visualize the behaviour of air-water flows upstream, through and downstream of mitre elbows in horizontal and vertical orientations. Important aims are to assess how the flow patterns change character as the fluids pass through the sharp elbows and to represent these changes by use of the Mandhane et al. [1] map.

We propose a novel visual representation that allows identifying the flow patterns both upstream and downstream of the elbows in a single non-dimensional Mandhane et al. map for each elbow orientation.

Two-phase pressure drop

The prediction of pressure drop across pipe fittings, like elbows and pipe bends represents a crucial aim to the designers of two-phase flow piping systems. The pressure drop across elbows and pipe fittings is affected by many factors, which are reported by many studies in the literature. Section 3.3.1 reviews the effect of elbows structure on the two-phase pressure drop, while Section 3.3.2 illustrates the effect of the flow conditions.

Effect of the elbow structure

The pipe diameter D^* and the bend curvature ratio C have been reported by many authors as effective factors on the two-phase pressure drop across elbows and pipe bends.

Experimental and numerical investigations by Graf and Neti [53] studied the pressure drop of air-water bubbly flow across 90° round elbows. The study reported that the pressure drop increases as the elbow curvature ratio C decreases. The experimental and the numerical data have good agreement with Chisholm [54]'s pressure drop prediction model. Chen et al. [55] studied the frictional pressure drop of air-water flow through wavy pipes with different diameters, curvature radii and spacer length for wide range of flow conditions. The experimental re-

sults show that the two-phase pressure drop increases with the decrease of the curvature ratio C. New two-phase multiplier correlation was proposed in terms of the Lockhart and Martinelli [5]'s parameter X and liquid-phase Froude number Fr_{L}. The proposed multiplier fits the experimental data of the study, and Chen et al. [44]'s study with 15.86% average error. Chen et al. [56] studied the pressure drop of refrigerant R-410A two-phase flow across $\cup$ bends with different diameters and curvature ratios for different mass velocities G^{*}. The study reported that the two-phase pressure drop increases as the curvature ratio C decreases. A new two-phase friction factor was proposed in terms of two-phase Reynolds number $\mathcal{R}e_{\text{tp}}$, Weber number We and curvature ratio C. The proposed friction factor fits the experimental data with $\pm$19.1% average error. Benbella et al. [57] investigated the pressure drop of air-water flow through internal wavy vertical to horizontal 90° elbows with different curvature radii for wide range of flow conditions. The study examined the effect of the mass velocity G^{*}, operation pressure p^{*} and the curvature ratio C on the two-phase pressure drop. The pressure drop increases with the increase of the mass velocity, the system pressure and the decrease of the curvature ratio. The study proposed a new correlation for two-phase pressure loss coefficient $\mathcal{K}_{\text{tp}}$ in terms of two-phase Reynolds number $\mathcal{R}e_{\text{tp}}$ and the curvature ratio of the bend C. The proposed correlation fits their data with less than $\pm$10% average error.

Sánchez Silva et al. [58] carried out an experimental study to examine the pressure drop of air-water flow across horizontal 90° round elbows with different diameters and curvature ratios for wide range of flow conditions. The study proved that the pressure drop increases with the decrease of the pipe inside diameter. A new two-phase multiplier was proposed in terms of Dean number De and homogeneous volumetric fraction of the phases λ_{L} and λ_{G}. The predicted pressure drop, which is obtained by using the new multiplier, fits the experimental data with $\pm$7.75% average error. Padilla et al. [59] studied the pressure drop of refrigerant R-410A two-phase flow across horizontal 180° bends with different diameters and curvature ratios for wide range of flow conditions. The study found that the pressure drop through the bend increases with the decrease of the curvature ratio C. Pressure drop of air-water flow across 90° round elbows studied by Hsu et al.

[38] for different pipe diameters, curvature ratios, elbow orientations and wide range of flow conditions. The study reported that the two-phase pressure drop across the elbow increases with the decrease of the curvature ratio C.

Effect of flow conditions

The pressure drop of two-phase flow across pipe fittings is highly affected by the flow conditions as reported by numerous studies.

Tran [60] studied the pressure drop of refrigerants R-410A and R-134a two-phase flow through C-shape 180° bends for wide range of flow conditions and bend orientations. The study found that the pressure drop across the bend increases with the increase of the mass velocity G^*, the gas-phase quality x and the system operating pressure p^*. Wang et al. [46] and Chen et al. [56] carried out an experimental study on two-phase refrigerants R-22 and R-410A flow across 180° return bends to examine the effect of the flow conditions on the pressure drop. The experimental results showed mild effect of the gas-phase quality x on the multiplier of the two-phase pressure drop across the bend for both working refrigerants. Air-water pressure drop through a vertical to horizontal 90° round elbow investigated by Spedding and Bénard [61] to examine the effect of flow conditions on the two-phase frictional pressure drop. The experimental results reported negative values of the frictional pressure drop in the vertical pipe upstream of the elbow for low superficial velocities of upward flow. The pressure drop across the elbow increases with the increase of superficial velocities of the liquid-phase j_L^* and the gas-phase j_G^*. Depending on the experimental data, an empirical correlation was proposed to fit the ratio between the two-phase equivalent length and the diameter $\mathcal{L}_{\text{tp}}$ in terms of two-phase Reynolds number $\mathcal{R}e_{\text{tp}}$.

The influence of the mass velocity G^*, gas-phase quality x and oil concentrations on the pressure drop of refrigerant-oil two-phase flow across wavy pipes investigated by Chen et al. [45] for wide range of flow conditions of R-134a and R-410A refrigerants. The study showed that the two-phase pressure drop increases with the increase of the mass velocity and the oil concentration. Domanski and Hermes [62] employed the experimental data of Geary [63] and Chen et al. [55] to propose a new pressure drop prediction model for two-phase pressure drop across

180° bends by using dimensional analysis Π theorem. The proposed model added a new multiplier to the straight pipe prediction model of Müller-Steinhagen and Heck [64], which represents the effect of the bend in terms of physical properties of the working fluids and the bend curvature ratio C. The new correlation fits 75% of the employed data with about ±25% error. The effect of bends orientation, gas-phase quality x and the total mass velocity G^* on the frictional pressure drop of two-phase refrigerant R-134a flow along straight and wavy pipes with 180° bends studied by Chen et al. [65]. The experimental results showed that pressure drop through the bend of vertical orientation were higher than that in horizontal orientation. Furthermore, the ratio between the bend and straight pipe pressure drop was highly affected by the total mass velocity of the flow G^* and the gas-phase quality x. Sánchez Silva et al. [58] reported that the pressure drop of air-water flow across horizontal 90° round elbow increases with the increase of air and water superficial velocities.

Padilla et al. [59] found that the pressure drop of refrigerant R-410A two-phase flow through 180° horizontal bends increases with the increase of the total mass velocity G^* and the system pressure p^*. Hsu et al. [38] showed that the frictional pressure drop of air-water flow through 90° round elbows increases with the increase of the total mass velocity G^* and the air mass quality x for horizontal and vertical orientations. The experimental data showed that the frictional pressure drop across the elbow in vertical orientation, with the flow goes upward, was larger than that in the horizontal orientation for the same flow conditions. Bowden and Yang [66] investigated the pressure drop of air-water flow through 90° round elbows for wide range of flow conditions. The experimental results showed mild effect of the air mass quality x on the two-phase pressure loss coefficient. The study employed the modified Lockhart and Martinelli [5] two-phase multiplier Φ_L to fit the experimental data.

This work investigates the pressure drop of air-water flow along the test sections and across a horizontal and horizontal to vertical 90° sharp-angled mitre elbows for wide range of flow conditions.

Predictions of two-phase flow patterns and pressure drop

This Section reviews numerous flow patterns prediction maps for two-phase flow through horizontal and vertical pipes and pressure drop prediction models for two-phase flow through straight pipes and across 90° round elbows. Section 3.4.1 reviews the proposed maps to predict the adiabatic two-phase flow patterns in straight pipes for horizontal and vertical orientations. The prediction models of two-phase pressure drop along straight pipes and across elbows are found in Section 3.4.2.

Flow pattern maps

Flow pattern maps are used to predict the flow regimes, which are usually expressed as two dimensional graphs with many inside boundaries. The boundaries represent the transition zones between the flow patterns like the transition region between the laminar and the turbulent flows in single-phase flow.

The importance of flow patterns prediction is related to their influence on the local two-phase flow properties, like the pressure drop and the heat transfer [6, 26, 67, 68, 69, 70].

Numerous studies have been conducted to propose the pattern maps of two-phase flow through different geometries for adiabatic and diabatic flow conditions. Many of these studies expressed the maps in terms of dimensional parameters including physical properties of the working fluids, while limited studies employed non-dimensional parameters [1, 2, 71, 72].

Most of these maps are limited to special experimental conditions and they cannot predict the flow patterns with acceptable percentage of error at different flow conditions [6, 73].

This Section illustrates the most cited flow pattern maps of adiabatic two-phase flow through horizontal and vertical pipes, which are conducted at the same conditions of the present work.

Depending on wide range of experimental data of many studies [74, 75, 76], Baker [71] proposed a pattern map for two-phase flow along horizontal pipes in terms of

superficial mass velocities and fluids properties as shown in Figure 3.2. To cover

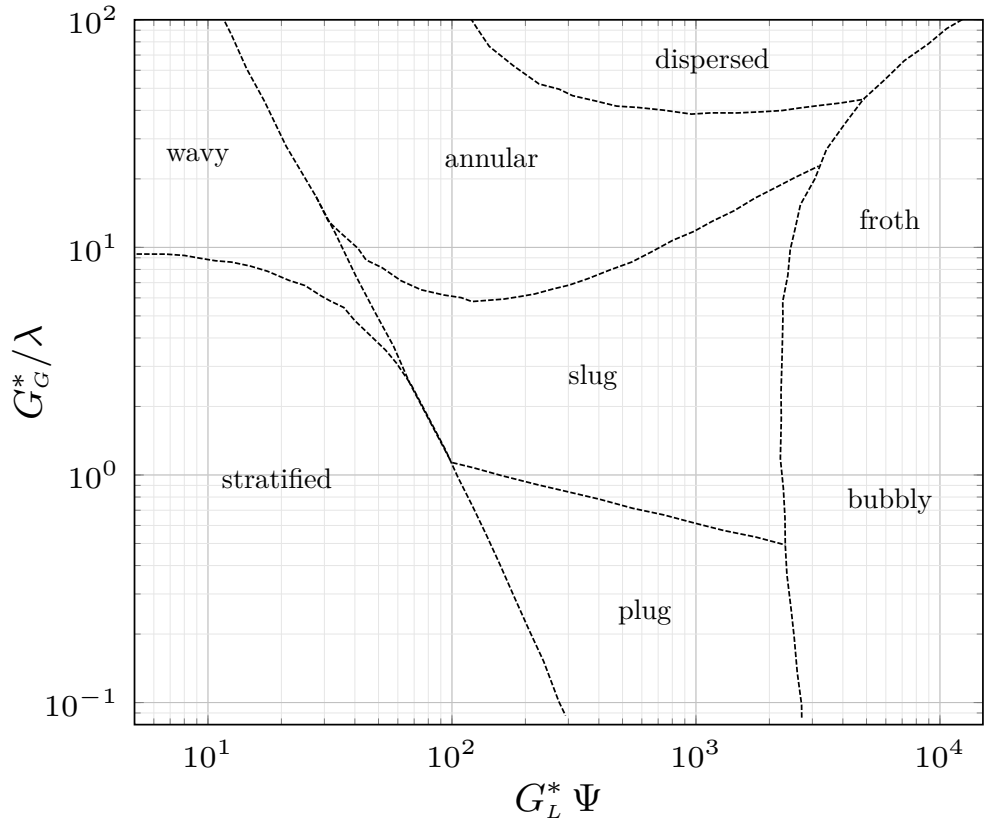

Figure 3.2: Baker's prediction map for two-phase flow patterns along horizontal pipes [71].

wide range of working fluids, the map employed the parameter Ψ with liquid-phase mass velocity in the abscissa and the parameter λ with gas-phase mass velocity in the ordinate. The parameters Ψ and λ are defined in terms of physical properties of the working fluids as:

$$\Psi = \left(\frac{\sigma^*_{water}}{\sigma^*_L}\right)\left[\left(\frac{\mu^*_L}{\mu^*_{water}}\right)\left(\frac{\rho^*_{water}}{\rho^*_L}\right)^2\right]^{1/3}, \tag{3.6}$$

$$\lambda = \left(\frac{\rho^*_G}{\rho^*_{air}}\frac{\rho^*_L}{\rho^*_{water}}\right)^{1/2}. \tag{3.7}$$

A two-phase flow map was proposed for vertical pipe flow by Hewitt and Roberts [2] in terms of superficial momentum fluxes of the phases as shown in Figure 3.3. Although the map was proposed in terms of dimensional parameters, it can predict the flow patterns for wide range of flow conditions with acceptable percentage of error because it has been proposed depending on experimental data of air-water and steam-water flows through wide range of pipes diameters.

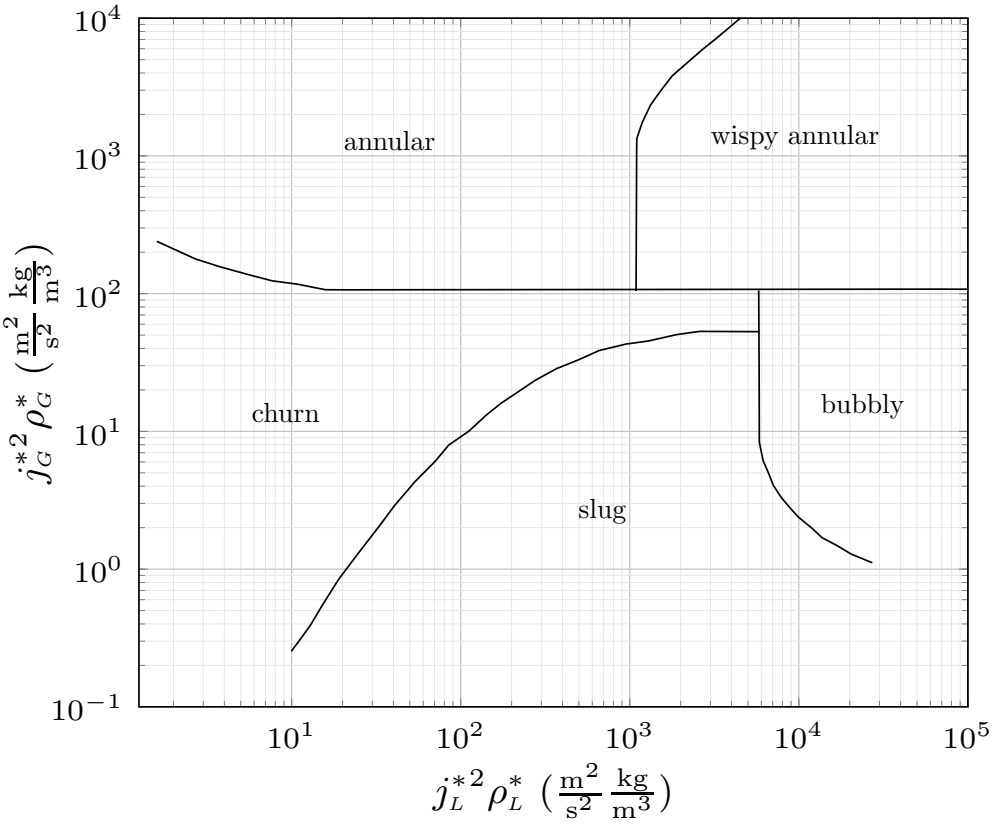

Figure 3.3: Hewitt and Roberts [2]'s map for two-phase flow in vertical pipes

Mandhane et al. [1] used wide range of two-phase flow data to propose a flow patterns prediction map, as shown in Figure 3.4. The map has been proposed in terms of liquid-phase and gas-phase superficial velocities j_L^* and j_G^* to consider the effect of pipe diameter on the flow patterns. To minimize the generated error due to the influence of the fluids physical properties on the flow regimes, the boundaries between the patterns in this map were represented as wide regions instead of lines. The map has the ability to predict the two phase flow patterns in horizontal pipes with acceptable percentage of error although it has been proposed in terms of dimensional parameters.

Depending on theoretical analysis and experimental results Taitel and Dukler [72] proposed a prediction map of two-phase flow through horizontal pipes in terms of non-dimensional parameters, which include the physical properties of the fluids and the pipe diameter, as illustrated in Figure 3.5. The abscissa of the map is the Martinelli parameter X and it can be defined by using:

$$X = \left(\frac{(\Delta p^*/\Delta l^*)_L}{(\Delta p^*/\Delta l^*)_G} \right)^{1/2}. \tag{3.8}$$

The parameter K, in the left y ordinate, is proposed to predict the boundary line

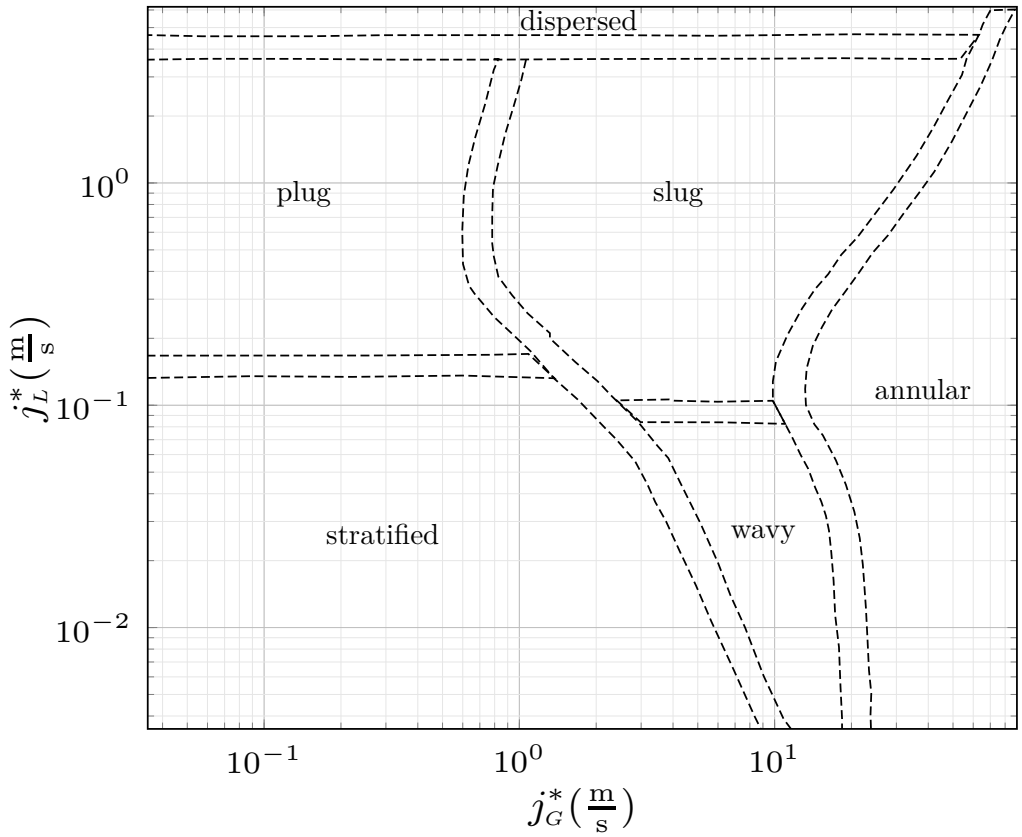

Figure 3.4: Mandhane et al. [1]'s map for horizontal two-phase flow

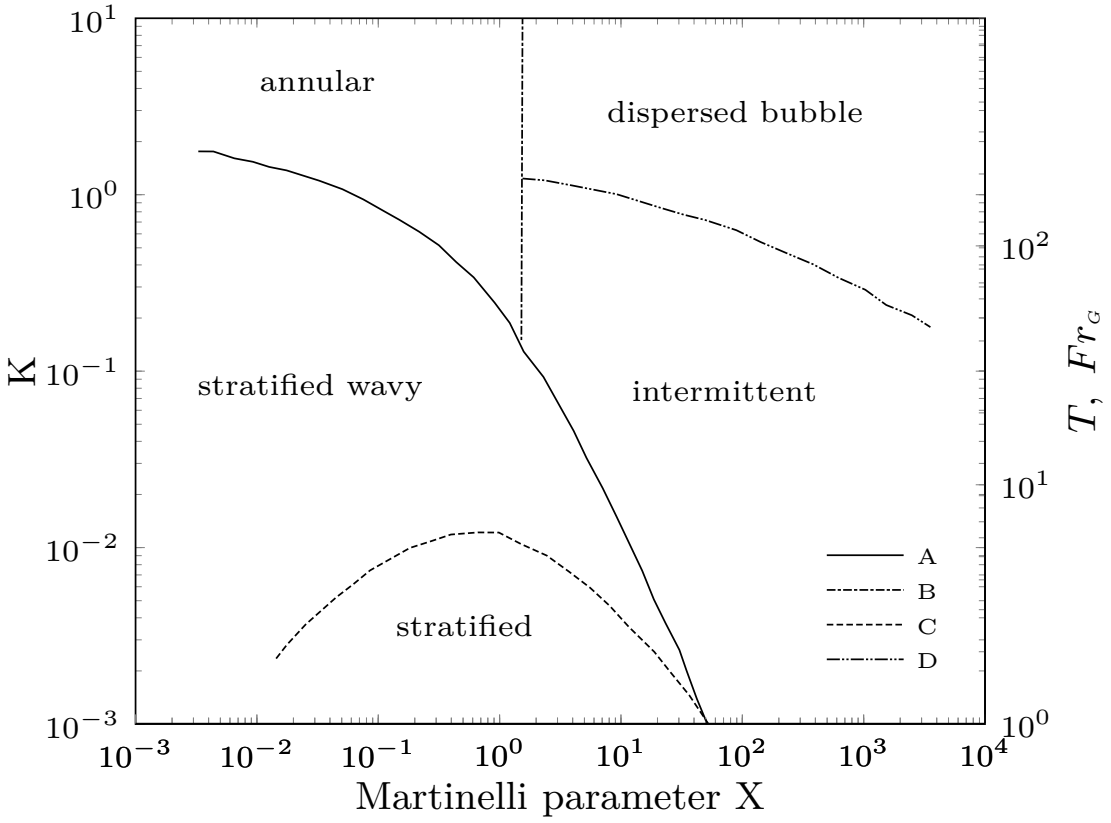

Figure 3.5: Taitel and Dukler [72]'s two-phase flow pattern map for horizontal flow

C between the stratified and the stratified wavy regimes in terms of the physical properties of the fluids as:

$$K = \left[\frac{\rho_G^* j_G^{*2} j_L^*}{(\rho_L^* - \rho_G^*) g^* \nu_L^*}\right]^{1/2}, \tag{3.9}$$

where ν^* is the kinetic viscosity. The parameters of the right y ordinate are used to predict the other patterns. The gas-phase Froude number Fr_G is employed to predict the boundaries A and B and it can be defined as:

$$Fr_G = \sqrt{\frac{\rho_G^*}{\rho_L^* - \rho_G^*}} \frac{j_G^*}{\sqrt{D^* g^*}}. \tag{3.10}$$

The parameter T in the right y ordinate is used to predict the boundary D and it can be defined by using:

$$T = \left[\frac{(\Delta p^*/\Delta l^*)_L}{(\rho_L^* - \rho_G^*) g^*}\right]^{1/2}. \tag{3.11}$$

Two-phase pressure drop prediction models

Three different approaches were followed by many researchers to predict the pressure drop of two-phase flow:

- Empirical approach: The prediction models of this approach are usually simple to use, proposed depending on experimental data and most of them are limited to a special experimental conditions.
- Analytical approach: The proposed models depending on this approach used complex calculations and need more time to get one solution. Most of these models depend on mathematical assumptions and limited to a specific flow conditions.
- Phenomenological approach: The models of this approach employed theoretical analysis and experimental data to include the effect the flow patterns on the two-phase pressure drop. These types of models are not valid for different types of flow patterns and they need an accurate data of flow patterns.

This Section includes many empirical models which are proposed to predict the pressure drop of two-phase flow along straight pipes and across 90° elbows. The

models are classified according to their assumptions to express the two-phase flow as:

- Homogeneous models: These models assume both phases to flow at the same velocity, the phases are thermodynamically equilibrium and an appropriate single-phase friction factor $\mathcal{C}_f$ can be used as a two-phase friction factor. These models are recommended for high velocities flows with low gas-phase or low liquid-phase fractions, like bubbly and mist flows [70].

- Separate flow models: These models assume each phase to flow separately at different velocities in the pipe area, proportional with its mass quality, and the pressure drop in each phase is equal to the total two-phase pressure drop:

$$\left.\frac{\Delta p^*}{\Delta l^*}\right|_{L} = \left.\frac{\Delta p^*}{\Delta l^*}\right|_{G} = \left.\frac{\Delta p^*}{\Delta l^*}\right|_{\text{tp}}. \tag{3.12}$$

  These models express the two-phase pressure drop in terms of two-phase multiplier and single-phase pressure drop per unit length as will be illustrated in this Section [70].

- Chisholm models: These models assume each phase to flow alone in the whole area of the pipe and a two-phase multiplier can be added to represent the effect of the other phase, similar to the separate flow models.

Lockhart and Martinelli's model

This model represents one of the earliest models, which are developed the separate flow theory. The model suggested four different flow cases, tt when the flow is turbulent for both phases, vv when the flow is laminar for both phases, vt when the liquid-phase flow is laminar and the gas-phase is turbulent and tv when the liquid-phase flow is turbulent and the gas-phase is laminar. The two-phase frictional pressure drop according to this model is defined as:

$$\Delta p^*_{\text{tp}} = \Phi^2_{k}\, \Delta p^*_{k}, \tag{3.13}$$

where Δp^*_{tp} is the two-phase pressure drop, Φ_{k} is the two-phase multiplier, Δp^*_{k} is the single-phase pressure drop and the subscript k=L for liquid-phase and k=G

for gas-phase. The single-phase pressure drop Δp_k^* is defined for each phase in terms of the total mass velocity G^* as:

$$\Delta p_L^* = 4\,\mathcal{C}_{f_L}\left(\frac{\Delta l^*}{D^*}\right) G^{*2}(1-x)^2\left(\frac{1}{2\rho_L^*}\right), \tag{3.14}$$

$$\Delta p_G^* = 4\,\mathcal{C}_{f_G}\left(\frac{\Delta l^*}{D^*}\right) G^{*2}x^2\left(\frac{1}{2\rho_G^*}\right), \tag{3.15}$$

where $\mathcal{C}_{f_L}$ and $\mathcal{C}_{f_G}$ are the single-phase Darcy friction factors for liquid and gas phases respectively, and, for turbulent flow, they can be computed by using Blasius [77]'s formula as:

$$\mathcal{C}_{f_L} = \frac{0.079}{\mathcal{R}e_L^{0.25}} \quad \text{and} \quad \mathcal{R}e_L = \frac{G^*(1-x)D^*}{\mu_L^*}, \tag{3.16}$$

$$\mathcal{C}_{f_G} = \frac{0.079}{\mathcal{R}e_G^{0.25}} \quad \text{and} \quad \mathcal{R}e_G = \frac{G^*xD^*}{\mu_G^*}. \tag{3.17}$$

For laminar flow conditions $\mathcal{R}e_k \leq$2000:

$$\mathcal{C}_{f_k} = \frac{16}{\mathcal{R}e_k}. \tag{3.18}$$

The two-phase pressure drop multipliers Φ_L^2 and Φ_G^2 are correlated by Chisholm [78] as:

$$\Phi_L^2 = 1 + \frac{\mathcal{C}}{X} + \frac{1}{X^2}, \tag{3.19}$$

$$\Phi_G^2 = 1 + \mathcal{C}X + X^2, \tag{3.20}$$

where X is known as Martinelli parameter, which represents the ratio between the liquid-phase and the gas-phase pressure gradients, and it can be defined as:

$$X = \frac{(\Delta p^*/\Delta l^*)_L}{(\Delta p^*/\Delta l^*)_G}. \tag{3.21}$$

The values of the empirical parameter $\mathcal{C}$ in Equations (3.19) and (3.20) were proposed by Chisholm [78] for different flow conditions as listed in Table 3.1. Figure 3.6 illustrates the two-phase flow multiplier of Lockhart and Martinelli [5] model Φ_k in terms of Matinelli parameter X for wide range of flow conditions.

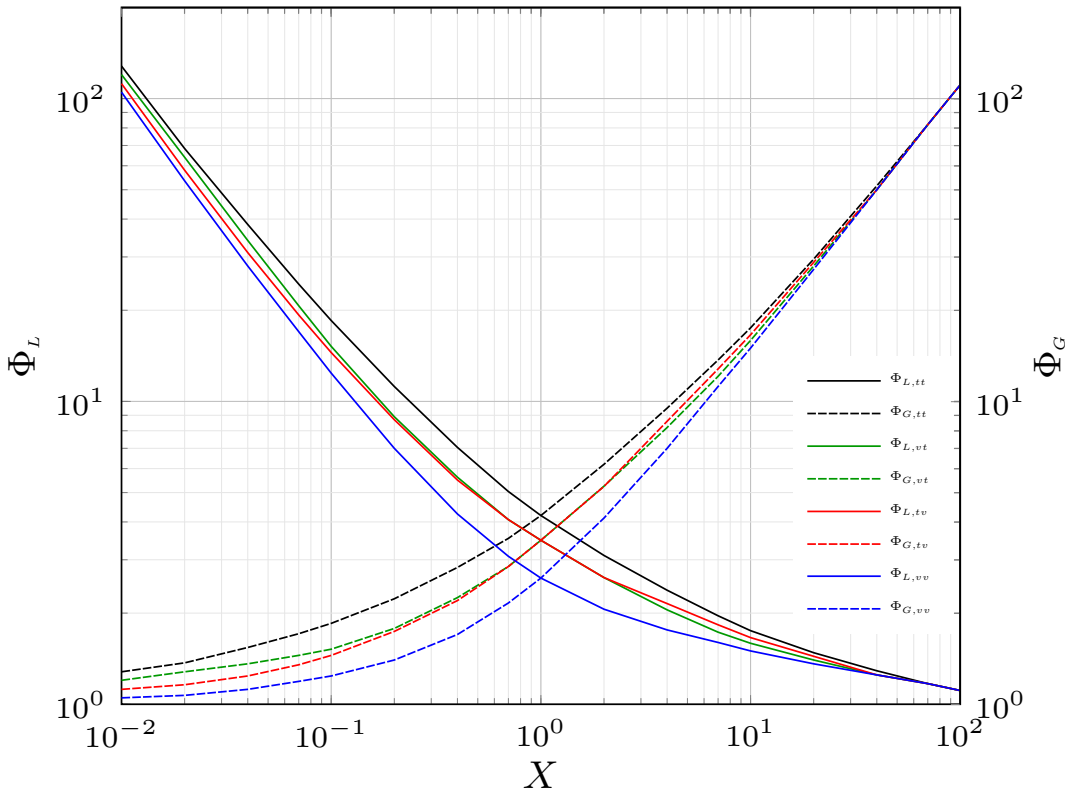

Figure 3.6: Two-phase flow multiplier Φ_k values in terms of Martinelli parameter for wide range of flow conditions [5].

Table 3.1: Experimental values of the parameter $\mathcal{C}$ [78].

Liquid-phase	Gas-phase	Symbol	$\mathcal{C}$
turbulent	turbulent	(tt)	20
laminar	turbulent	(vt)	12
turbulent	laminar	(tv)	10
laminar	laminar	(vv)	5

The parameter $\mathcal{C}$ provides the Lockhart and Martinelli model a unique flexibility to fit the experimental pressure drop data of two-phase flow along straight pipes with the presence of different geometries, such as pipe fittings, elbows and pipes with different cross-sectional areas [40, 66, 79, 80, 81, 82, 83, 84].

Chisholm's pipe flow model

This model has been developed depending on the assumptions of Chisholm's approach by Chisholm [85]. The two-phase multiplier of this model Φ^2_{Ch} is defined

as:

$$\Phi^2_{_{Ch}} = \frac{\Delta p^*_{\text{tp}}}{\Delta p^*_{_{kO}}}, \tag{3.22}$$

where $\Delta p^*_{_{kO}}$ is, liquid-only $k = L$ or gas-only $k = G$, the frictional pressure drop and it is defined in terms of total mass velocity G^* as:

$$\Delta p^*_{_{LO}} = 4\,\mathcal{C}_{f_{_{LO}}} \left(\frac{\Delta l^*}{D^*}\right) G^{*2} \left(\frac{1}{2\rho^*_{_L}}\right), \tag{3.23}$$

$$\Delta p^*_{_{GO}} = 4\,\mathcal{C}_{f_{_{GO}}} \left(\frac{\Delta l^*}{D^*}\right) G^{*2} \left(\frac{1}{2\rho^*_{_G}}\right), \tag{3.24}$$

where $\mathcal{C}_{f_{_{LO}}}$ and $\mathcal{C}_{f_{_{GO}}}$ are single-phase Darcy friction factors for liquid-phase and gas-phase respectively, and they are defined as:

- For turbulent flow conditions $\mathcal{R}e \geq$2000:

$$\mathcal{C}_{f_{_{LO}}} = \frac{0.079}{\mathcal{R}e^{0.25}_{_{LO}}} \quad \text{and} \quad \mathcal{R}e_{_{LO}} = \frac{G^* D^*}{\mu^*_{_L}}, \tag{3.25}$$

$$\mathcal{C}_{f_{_{GO}}} = \frac{0.079}{\mathcal{R}e^{0.25}_{_{GO}}} \quad \text{and} \quad \mathcal{R}e_{_{GO}} = \frac{G^* D^*}{\mu^*_{_G}}. \tag{3.26}$$

- For laminar flow conditions $\mathcal{R}e \leq$2000:

$$\mathcal{C}_{f_{_{kO}}} = \frac{16}{\mathcal{R}e_{_{kO}}}, \tag{3.27}$$

  where the subscript kO=LO for liquid-phase and kO=GO for gas-phase.

The two-phase multiplier $\Phi^2_{_{Ch}}$ is correlated as:

$$\Phi^2_{_{Ch}} = 1 + (Y^2 - 1)\left[Bx^{2-n/2}(1-x)^{2-n/2} + x^{2-n}\right], \tag{3.28}$$

where Y, B and n are experimental parameters and x is the gas-phase mass quality. The parameter Y in (3.28) represents the ratio between the liquid-only and the gas-only single-phase pressure drops, and it can be defined as:

$$Y^2 = \frac{\Delta p^*_{_{GO}}}{\Delta p^*_{_{LO}}}. \tag{3.29}$$

The parameter B in (3.28) is an empirical parameter and it was correlated in terms of Y values as:

- For $0 < Y < 9.5$:

$$\begin{aligned} B &= \frac{55}{G^{*0.5}} \quad \text{for} \quad G^* \geq 1900\,\mathtt{kg/m^2.s}, \\ B &= \frac{2400}{G^*} \quad \text{for} \quad 500 \geq G^* \leq 1900\,\mathtt{kg/m^2.s}, \\ B &= 4.8 \quad \text{for} \quad G^* \leq 500\,\mathtt{kg/m^2.s}. \end{aligned} \tag{3.30}$$

- For $9.5 < Y < 28$:

$$\begin{aligned} B &= \frac{550}{YG^{*0.5}} \quad \text{for} \quad G^* \leq 600\,\mathtt{kg/m^2.s}, \\ B &= \frac{21}{Y} \quad \text{for} \quad 500 \geq G^* > 600\,\mathtt{kg/m^2.s}. \end{aligned} \tag{3.31}$$

- For $Y > 28$:

$$B = \frac{1500}{Y^2 G^{*0.5}}. \tag{3.32}$$

Depending on experimental data, it is found that the parameter n in Equation (3.28) has the value of n=0.25 for gas-phase qualities x<0.5 with ±0.02% accuracy.

Friedel model

This model employed the separated flow model to represent te pressure drop in straight pipes in terms of two-phase multiplier and single-phase liquid pressure drop. The frictional two-phase pressure drop according to this model is defined as:

$$\Delta p^*_{\text{tp}} = \Delta p^*_{LO} \Phi^2_{\text{Fri}}, \tag{3.33}$$

where Δp^*_{LO} is single-phase pressure drop for liquid-phase only as defined in (3.23) while Φ^2_{Fri} is the two-phase multiplier and it can be expressed as:

$$\Phi^2_{\text{Fri}} = A_1 + \frac{3.24 A_2 A_3}{Fr_H^{0.045} We_L^{0.035}}. \tag{3.34}$$

The factors in equation (3.34) are defined as follows:

$$A_1 = (1-x)^2 + x^2 \frac{\rho^*_L \mathcal{C}_{f_{GO}}}{\rho^*_G \mathcal{C}_{f_{LO}}}, \tag{3.35}$$

where $\mathcal{C}_{f_{LO}}$ and $\mathcal{C}_{f_{GO}}$ are the Darcy friction factors for liquid-phase only and gas-phase only as defined in (3.25) and (3.26).

$$A_2 = x^{0.78}(1-x)^{0.224}. \tag{3.36}$$

$$A_3 = \left(\frac{\rho_L^*}{\rho_G^*}\right)^{0.91} \left(\frac{\mu_G^*}{\mu_L^*}\right)^{0.19} \left(1 - \frac{\mu_G^*}{\mu_L^*}\right)^{0.7}. \tag{3.37}$$

$$Fr_{_L} = \frac{G^{*2}}{g^* D^* \rho_{_H}^{*2}}, \tag{3.38}$$

where G^* is the total mass velocity and $\rho_{_H}^*$ is the homogeneous density and it can be defined as:

$$\rho_{_H}^* = \left(\frac{x}{\rho_{_G}^*} + \frac{1-x}{\rho_{_L}^*}\right)^{-1}. \tag{3.39}$$

$$We_{_L} = \frac{G^{*2} D^*}{\sigma^* \rho_{_H}^*}. \tag{3.40}$$

Müller-Steinhagen and Heck's model

A simple model proposed by Müller-Steinhagen and Heck [64] to predict the frictional pressure drop of two-phase flow in straight pipes. The frictional pressure drop according to this model is defined in terms of gas-phase pressure drop and other parameters as:

$$\Delta p_{tp}^* = G^{'}(1-x)^{\frac{1}{3}} + \Delta p_{_{GO}}^* x^3, \tag{3.41}$$

where x is the gas-phase mass quality and $G^{'}$ is known as Muller parameter and it can be expressed as:

$$G^{'} = \Delta p_{_{LO}}^* + 2(\Delta p_{_{LO}}^* - \Delta p_{_{GO}}^*)x, \tag{3.42}$$

where $\Delta p_{_{LO}}^*$ and $\Delta p_{_{GO}}^*$ are liquid-only and gas-only pressure drops respectively and they can be expressed in terms of the total mass velocity of the flow G^* as:

$$\Delta p_{_{LO}}^* = 4\,\mathcal{C}_{f_{_{LO}}} \frac{G^{*2}}{2D^* \rho_{_L}^*} \tag{3.43}$$

$$\Delta p_{_{GO}}^* = 4\,\mathcal{C}_{f_{_{GO}}} \frac{G^{*2}}{2D^* \rho_{_G}^*} \tag{3.44}$$

where $\mathcal{C}_{f_{_{LO}}}$ and $\mathcal{C}_{f_{_{GO}}}$ are liquid-only and gas-only Darcy friction factors and they are defined in Equations (3.25), (3.26) and (3.27).

Chisholm's bends model

This model used Chisholm's approach to express the pressure drop of two-phase flow across 90° bends by modifying the parameter B of Chisholm [85]'s model in

terms of liquid-only pressure loss coefficient $\mathcal{K}_{LO}$ and the curvature ratio of the bend R^*/D^* as:

$$B = 1 + \frac{2.2}{\mathcal{K}_{LO}\left(2 + \frac{R^*}{D^*}\right)}. \tag{3.45}$$

The two-phase pressure drop across 90° round elbows according to this model is defined as:

$$\left.\frac{\Delta p^*_{\text{tp}}}{\Delta p^*_{LO}}\right|_{\text{b}} = 1 + \left(\frac{\rho^*_L}{\rho^*_G} - 1\right)\left[Bx(1-x) + x^2\right], \tag{3.46}$$

where Δp^*_{LO} is the liquid-only pressure drop across the bend and it can be expressed as:

$$\Delta p^*_{LO} = \frac{\mathcal{C}_{f_{LO}} G^{*2}_L \mathcal{L}_L}{2\rho^*_L}, \tag{3.47}$$

where $\mathcal{C}_{f_{LO}}$ is the liquid-only Darcy friction factor, defined in (3.25), G^* is the mass velocity, ρ^* is the density and $\mathcal{L}_L$ is the ratio between the equivalent length of the bend l_{eq} and the pipe diameter D^*.

Sookprasong et al.'s model

This model employed the homogeneous approach to propose a new multiplier for two-phase pressure drop across 90° round elbows in terms of the densities and the superficial velocities of the working fluids as:

$$\Phi^2 = \frac{(\rho^*_L j^*_L + \rho^*_G j^*_G)(j^*_L + j^*_G)}{\rho^*_L j^{*2}_L}. \tag{3.48}$$

The pressure drop of two-phase flow is defined according to this model as:

$$\left.\frac{\Delta p^*_{\text{tp}}}{\Delta p^*_L}\right|_{\text{b}} = \Phi^2, \tag{3.49}$$

where Δp^*_{tp} is the two-phase pressure drop across the elbow, Δp^*_L is the liquid-phase pressure drop across the elbow, which is defined in terms of liquid-phase pressure loss coefficient $\mathcal{K}_L$ as:

$$\Delta p^*_e = \mathcal{K}_L \frac{\rho^*_L j^{*2}_L}{2}. \tag{3.50}$$

Chapter 4

Experimental test facility and procedure

This Chapter illustrates the specifications of the test facility, the methodology of data reduction, the experimental flow conditions, the experimental procedure and the uncertainty calculations procedure.

Test facility design and specifications

A new experimental test rig was designed and built for this work in the Department of Mechanical Engineering at The University of Sheffield. The facility was composed of two main lines, one for air and one for water, a phase mixer, and test sections equipped with 90° sharp-angled mitre elbows as shown schematically in Figure 4.1. The rig was designed to operate with single-phase flow, with air or water, and air-water two-phase flow.

Water line

Water line consists of pumping unit, water filters, water flow meters and water tanks. The pumping unit was designed to feed the test sections with wide range of water flow rates at a constant operating pressure and it was assembled from many components as illustrated in Figures 4.2 and 4.3. A Penstar ULTRA3-7 variable speed pump operating at constant pressure and a maximum flow rate of 80l/min (litres per minute) was employed to pump water from a water storage tank. The pump was controlled automatically by a control unit which was assembled by the

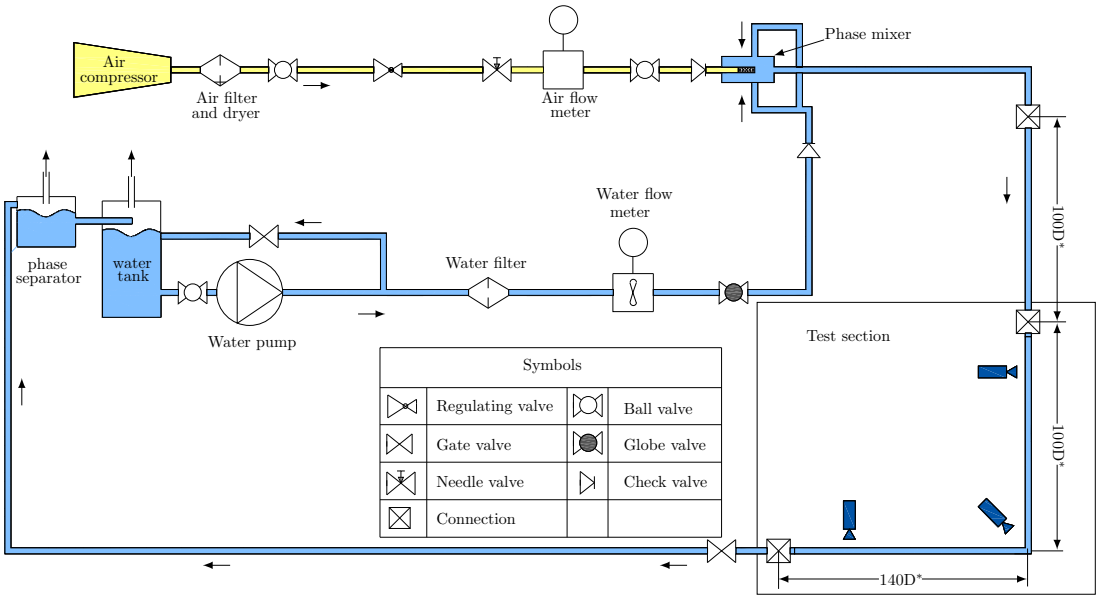

Figure 4.1: Schematic diagram of air-water test facility.

supplier from a pressure vessel, a pressure transducer, a pressure gauge, a variable speed controller and a potentiometer. The unit had the function of controlling the pump velocity automatically to obtain a constant pressure at the exit of the pump for all the flow rates. The potentiometer and the pressure gauge were employed to set the pressure to the operating value up to 6bar. In case of any change in the flow pressure at different flow rates the pressure transducer sent a signal to the variable speed controller to change the pump speed automatically and to keep the pressure constant at the new flow rate.

Two water filters were employed to minimize the intrusion of impurities in the test sections. The first one was a horizontal SpiroTrap MB3 filter, which was located at the exit point of the water storage tank after a ball valve as shown in Figures 4.2 and 4.4. The second filter was a 1mm mesh size in-line strainer, which was located after the pump as shown in Figures 4.2 and 4.4. The water flow rates were measured by two turbine type flow meters, Omega FTB-101 and Omega FTB-104, to cover two wide ranges of volume flow rates: 1.3-13.2 l/min and 6.6-60 l/min, respectively. The flow meters were calibrated by the manufacturer with a $\pm 0.5\%$ reading accuracy. A six digits rate meter, Omega DPF-702, was utilized to display the flow meters readings in l/min. Manual ball valves were employed to separate the air or water lines when operating the rig with single-phase flow. Figure 4.5 shows pictures of the turbine flow meter and the digital ratemeter.

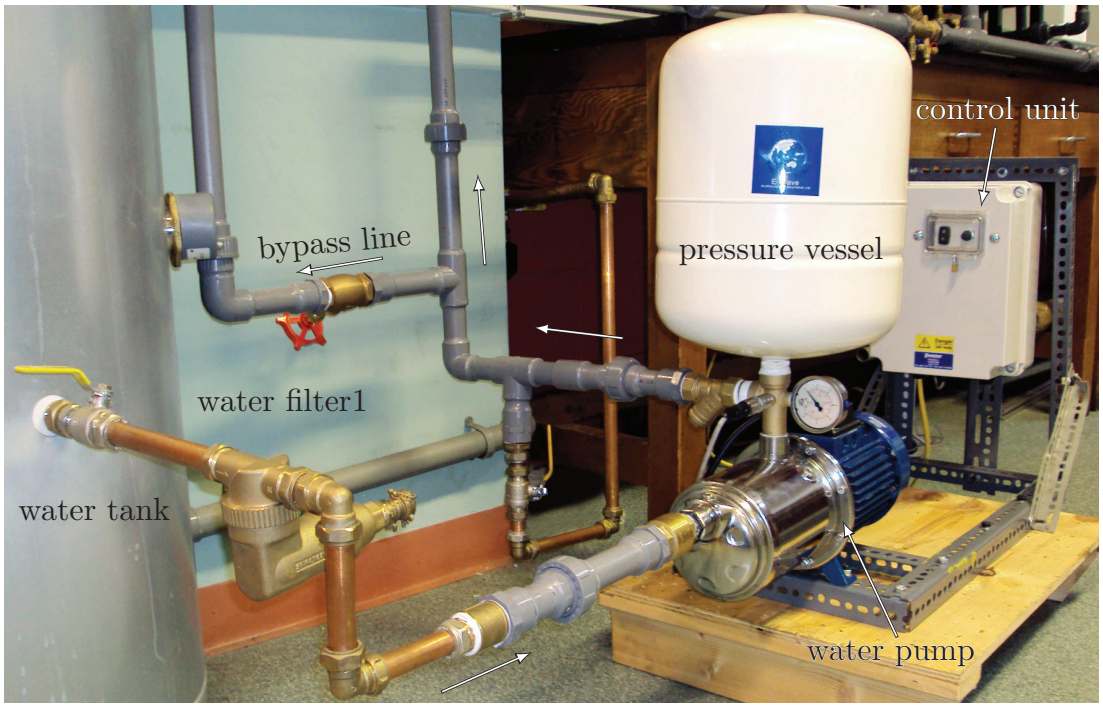

Figure 4.2: Specifications of pumping unit.

(a) Pressure gauge and transducer. **(b)** Pumping unit control box.

Figure 4.3: Pumping unit control.

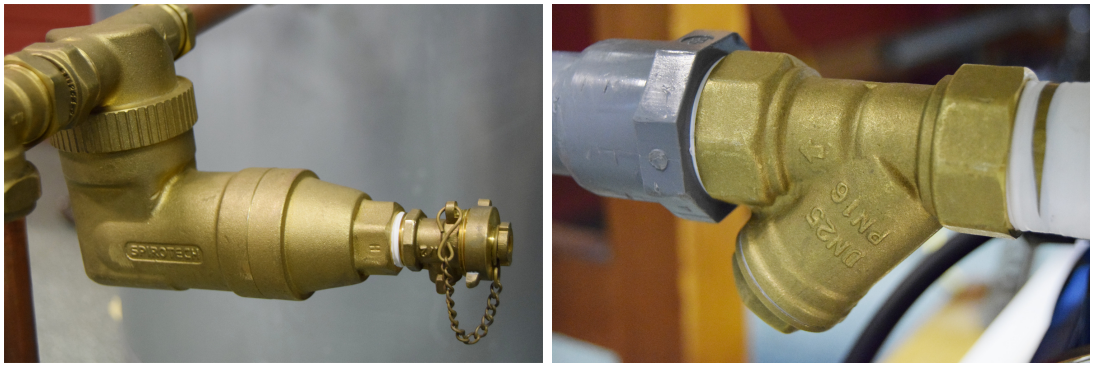

(a) SpiroTrap MB3 water filter. **(b)** In-line water filter.

Figure 4.4: Water filters.

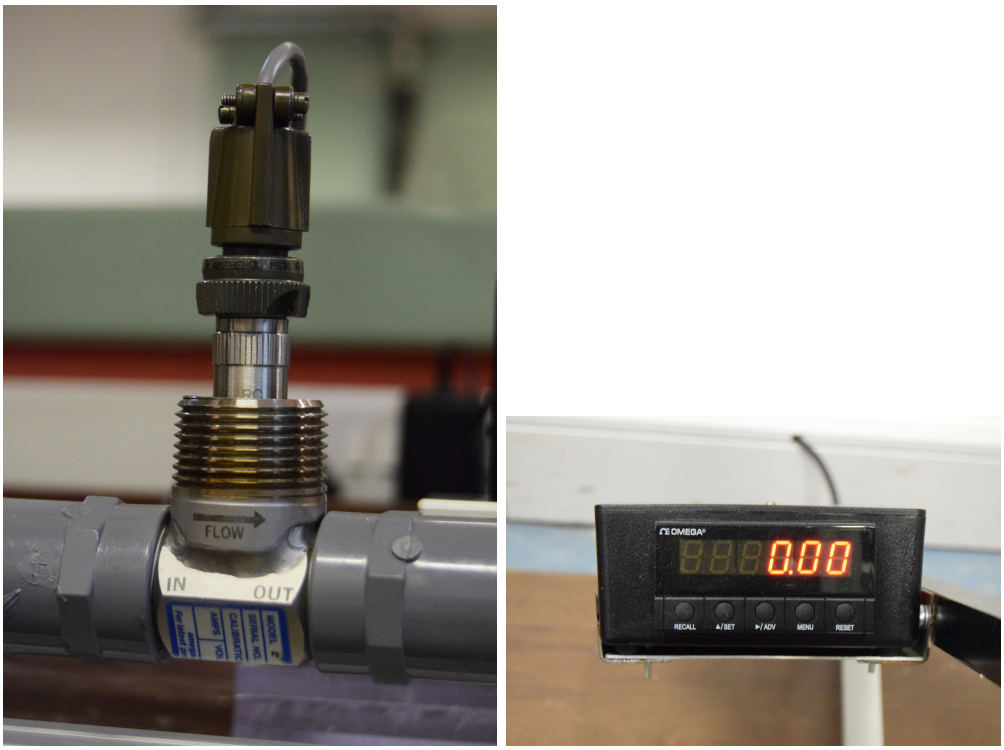

(a) Flow meter. **(b)** Digital ratemeter.

Figure 4.5: Water flow measurement kit.

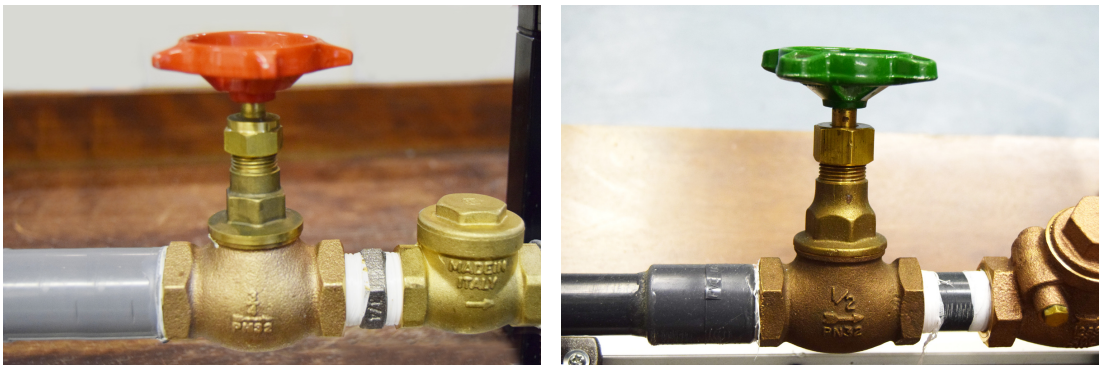

Figure 4.6: Water flow control valves.

Two different screw-down valves were employed to regulate the water flow manually, a 3/4 in globe valve and a 1/2 in needle valve, which were located after the FTB-104 and the FTB-101 flow meters respectively. The valves are shown in Figure 4.6, and their locations are shown in Figure 4.1.

A stainless steel tank with 150 litres capacity was employed as a water storage. Another tank of a 20 litres capacity was connected to the water line as illustrated in Figure 4.1, which had the function of phase-separation, when the rig operates with two-phase flow, the air rises up to the atmosphere, while the water flows down to the main storage tank to pump it again.

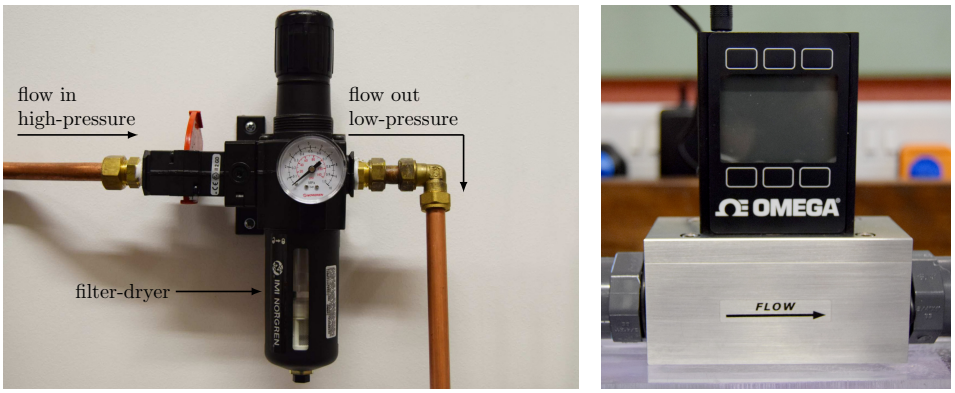

Figure 4.7: Pressure control valve (left) and air flow meter(right).

Air line

The air line was designed to supply the test sections with wide range of air flow rates. Air was supplied by an air compressor at 7bar pressure and regulated to the required flow rate up to 500 standard l/min by a pressure valve. An air filter-dryer was located before the air flow meter to supply the test sections with clean dry air. Air flow rate was regulated by a 1/2 in needle valve manually. An air mass flow meter, Omega FMA-1612A-v2, was used to measure the flow rates between 2.5 and 500 standard l/min. The flow meter was calibrated by the manufacturer with an accuracy of ±0.8% of the reading value and ±0.2% of the full scale value (FS). The pressure valve and the air flow meter are shown in Figure 4.7. A spring type check valve was located after the air flow meter, as illustrated in Figure 4.1, to block any water flow toward the air line when the rig operates with water or two-phase flow.

Phase-mixer:

An air-water phase-mixer was designed and constructed for this work to generate the two-phase flow. The mixer was constructed from a 4 in diameter upvc pipe with 5mm wall thickness and 250mm length. Two jets of water entered the mixer from opposite sides and perpendicularly to the axis of the mixer. Air entered the mixer parallel to its axis through a section of porous media characterized by holes with 0.1mm diameter. The air-water mixture left the mixer from the opposite side of the air entrance, as illustrated in Figure 4.8. A flow stabilizer was designed and constructed to reduce the flow circulation at the exit of the phase-mixer. The stabilizer was assembled from an acrylic pipe with 21mm diameter,

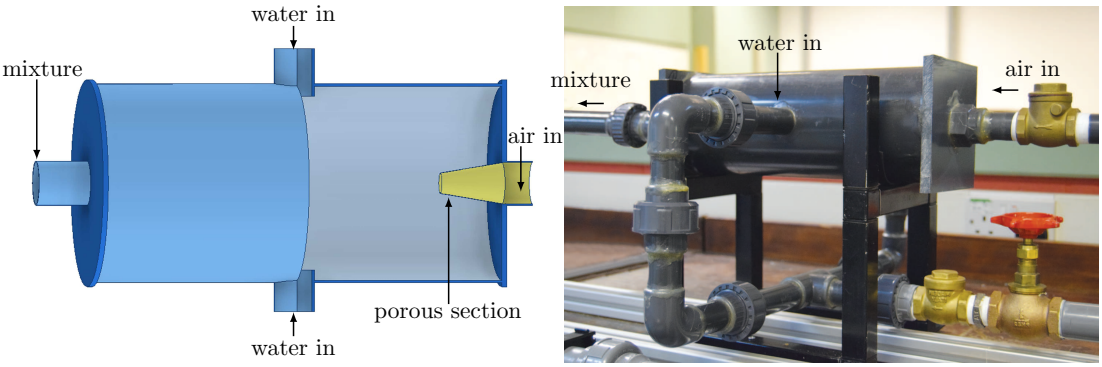

Figure 4.8: Schematic diagram and picture of the phase-mixer.

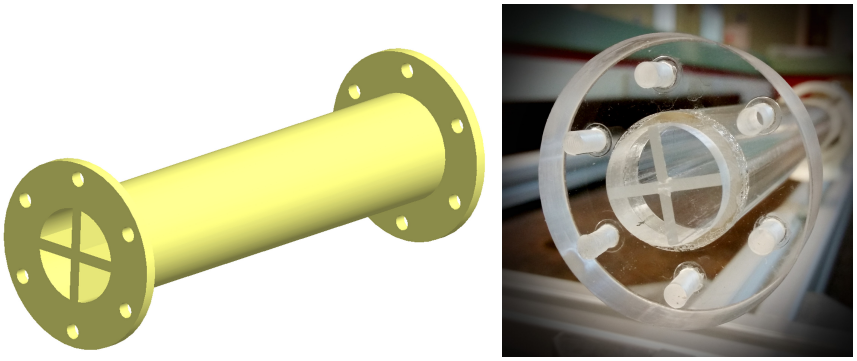

(a) **(b)**

Figure 4.9: Schematic diagram (a) and picture (b) of the flow stabilizer.

2mm wall thickness and 400mm length. Cross fins with 2mm thickness were used to divide the cross section of the pipe to obtain four streams as shown in Figure 4.9.

Test sections

Six test sections, three for flow visualization and three for pressure measurements investigations, were employed in this study. The test sections were constructed from commercial acrylic pipes with a wall thickness of 2mm, internal diameters D^*=11, 16 and 21mm and a total length of $240D^*$ for all pipe diameters ($100D^*$ upstream and $140D^*$ downstream of the elbow to ensure full recovery of the flow). For each test section, an additional straight $100D^*$-long pipe was located upstream of the section to ensure fully developed flow condition, as illustrated in Figure 4.1. Figures 4.10 and 4.11 show the schematic diagrams of the flow visualization and the pressure drop measurement test sections.

The test sections were assembled from segments, which were joined together by

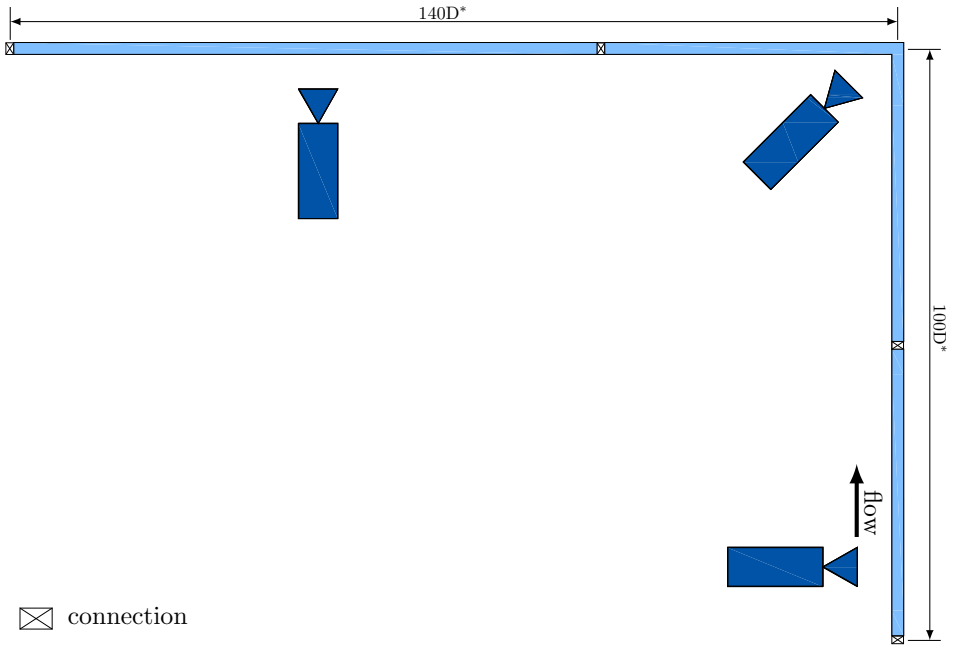

Figure 4.10: Schematic diagram of the flow visualization test sections.

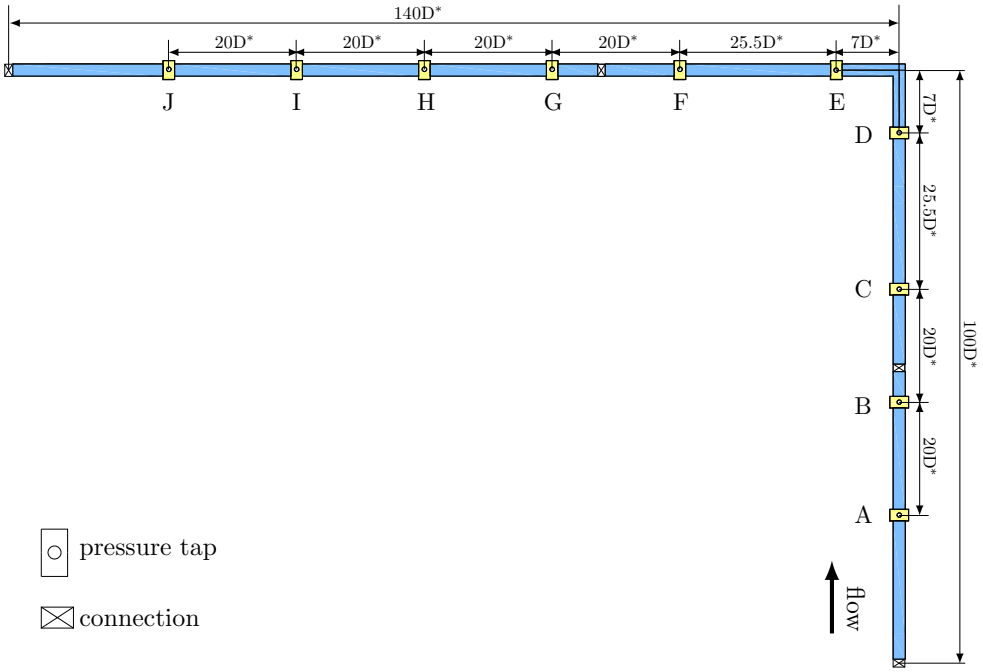

Figure 4.11: Schematic diagram of the pressure drop measurements test sections and measurements taps locations.

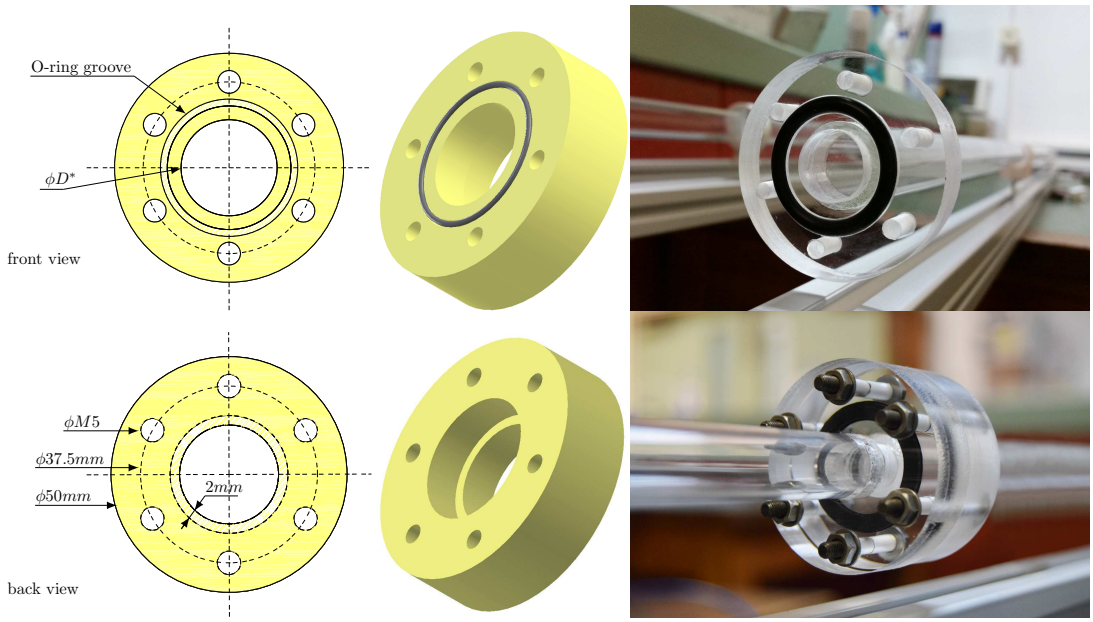

Figure 4.12: Schematic diagram and pictures of the connecting flanges.

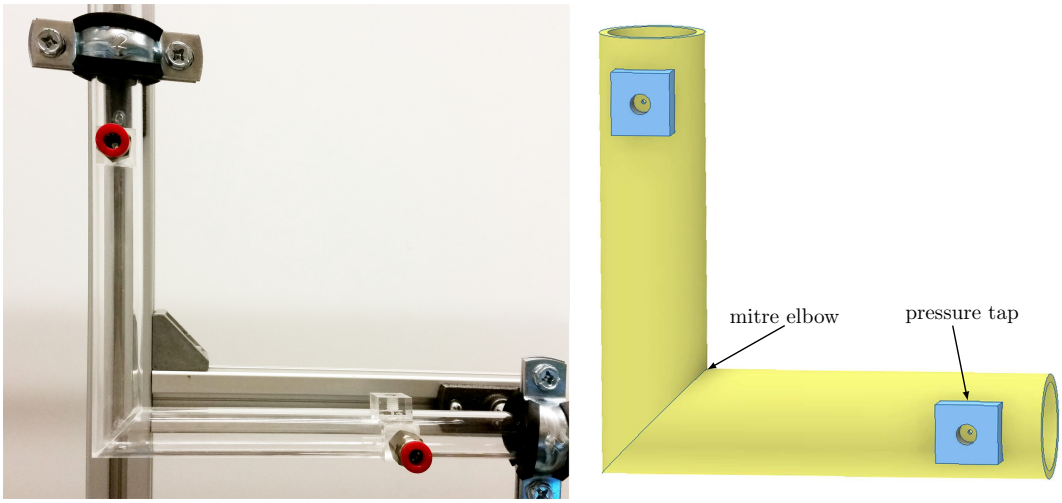

Figure 4.13: Schematic diagram and picture of 90° sharp-angled mitre elbow.

using an acrylic flanges. The flanges were designed carefully to seal the junctions between the pipe segments by using O-rings in order not to perturb the flow as shown in Figure 4.12. The 90° sharp-angled elbows were constructed by cutting two pipe pieces accurately at 45°, with maximum error of ± 0.5°, and by joining them accurately by using a special acrylic welding solution. Figure 4.13 shows the schematic diagram and picture of the mitre elbows. The test section was fixed to an aluminium frame, which was constructed from a square Bosch Rexroth bars with 30×30mm cross section and 8mm slot. The frame was designed to hold the different test sections and the connecting pipes for horizontal and vertical orientations. The portion of the pipe upstream of the elbow was always positioned

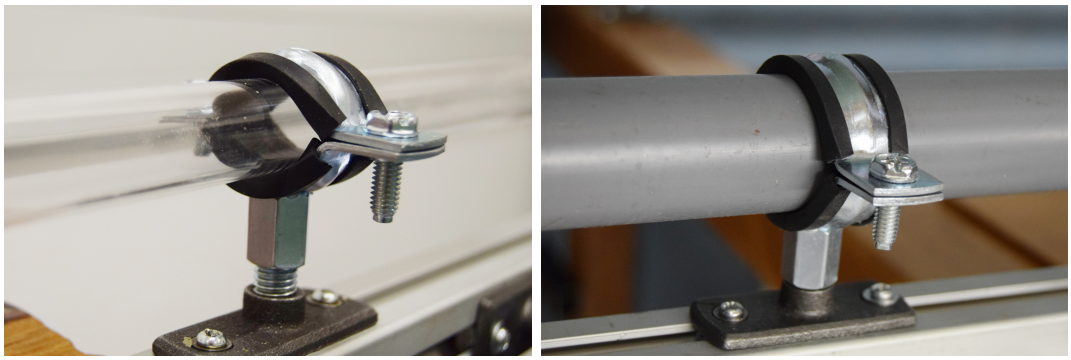

(a) Acrylic pipe clip. **(b)** Abs pipe clip.

Figure 4.14: Test sections pipe clips.

horizontally, while the portion downstream of the elbow was oriented horizontally or vertically with the fluids moving upward. Different sizes of pipe clips were utilized to fix the test sections and the other pipes to the frame as shown in Figure 4.14. The frame dimensions and specifications are illustrated in Figure 4.15.

Ten measurement stations (A-J) were located along the pressure drop measurements test sections, to measure the pressure distribution along the straight parts of the pipe and across the elbow, as shown in Figure 4.11. The pressure taps were designed and machined from the same material of the test sections. Holes with a diameter of 1mm were drilled radially through the pipe walls to allow the fluid to flow through the pressure taps without perturbing the flow inside the pipe. An M5 push-in fittings with 6mm flexible tubes were used to connect the pressure taps with the pressure measurement instruments. Additional pressure taps were located at four measurement stations, stations C-F, upstream and downstream of the elbow of the 16mm diameter test section, as shown in Figure 4.16, to measure the pressure of single-phase and two-phase flows at different angles around the pipe periphery (0° at the top, 90°, and 270°) for horizontal orientation. Plastic ABS pipes with 25mm diameter were employed to connect the test section with the water storage tank and the pumping unit.

Data acquisition

Two differential pressure transducers, Omega PX409-2.5DWU10V and Omega PX409-10WDWUI, were used to measure the pressure drop along the test sec-

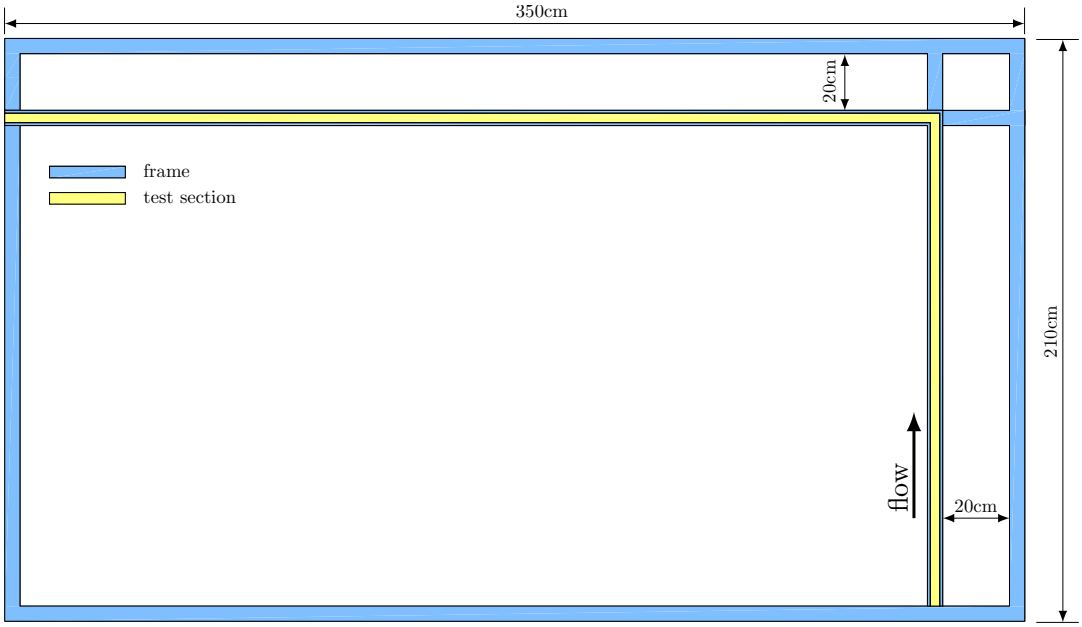

(a) Schematic diagram of the test section holding frame.

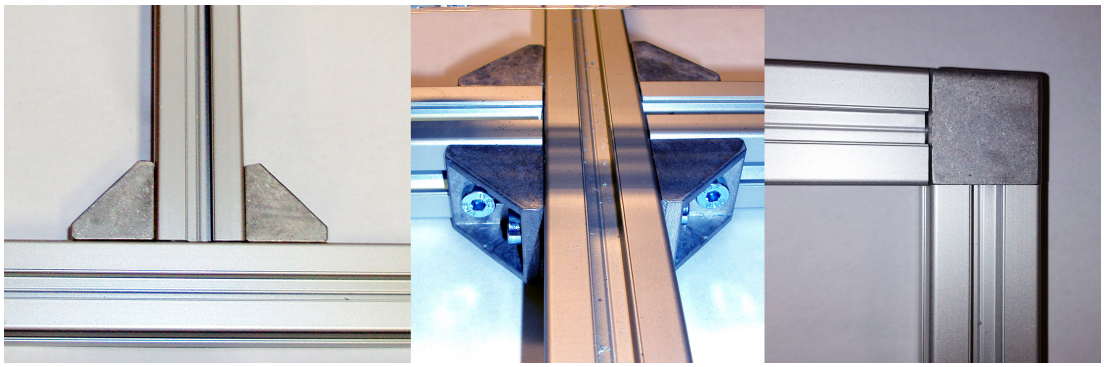

(b) Frame joints.

Figure 4.15: Schematic diagram and pictures of the frame.

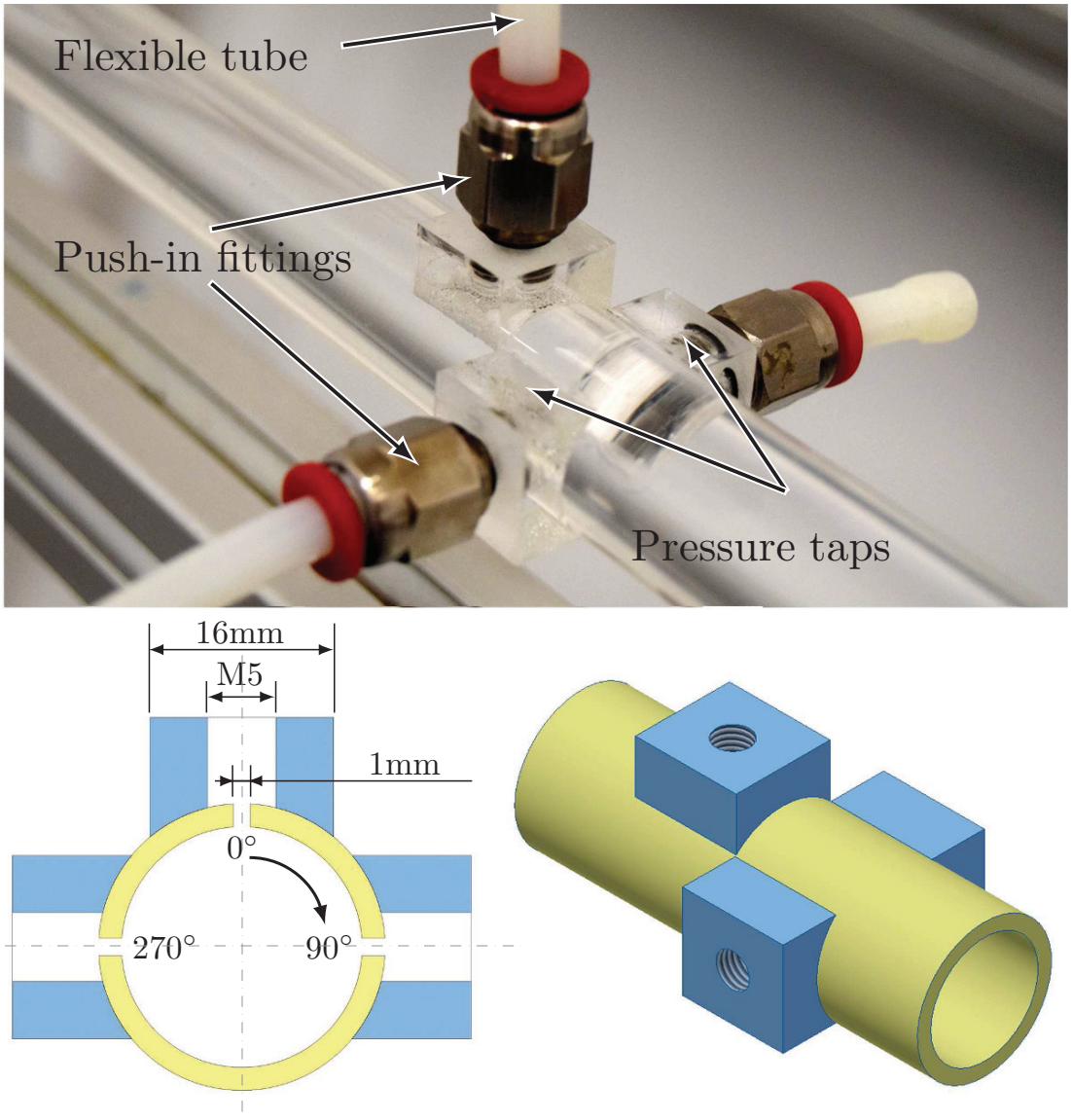

Figure 4.16: Schematic diagram and picture of pressure measurement taps.

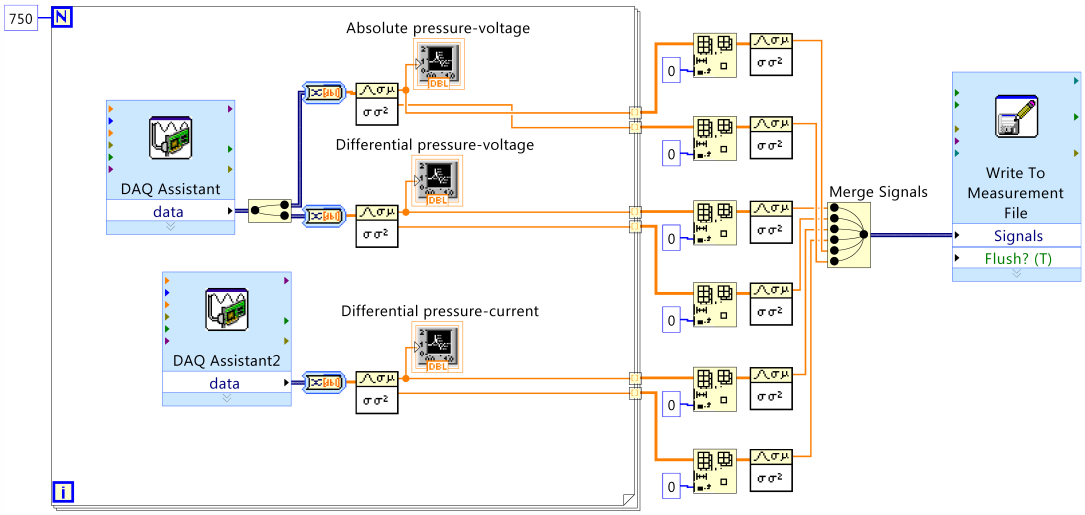

Figure 4.17: The block diagram of the LabView code.

tions when the rig operates with single-phase water or air-water two-phase flows. The transducers were operated in a range of (0−17.2 kPa and 0−2.5 kPa) respectively and they were calibrated by the manufacturer with a full scale (FS) best straight line (BSL) accuracy of ±0.08%. An MK Type4 differential water manometer was employed to measure the pressure drop of the air flow, operated in a range of 0−4.9 kPa with ±0.1% of the reading value and ±1 Pa accuracy at 20°C. An absolute pressure transducer, Omega PX309-100G5V, was used to measure the absolute pressure in a range of $0 - 680$ kPa and it was calibrated by the manufacturer with a ±0.25% FS BSL accuracy. The pressure signals were recorded by a National Instrument data acquisition system with 16-bit resolution, which was consisted of an NI-USB-6002 card for voltage signal and an NI-9203-analogue-channel with an NI-CDAQ-9171-USB-Chasis for current signals. A special Labview code was utilized for the logging and processing of the pressure measurements. The block diagram of the Labview code is illustrated in Figure 4.17. The temperature of the flow was measured at each experimental test by using type K thermocouple with a Picco data logger. The temperature measurement kit was carefully calibrated against an accurate thermometer with less than ± 0.5°C accuracy. The calibration data of the flow, temperature and pressure measurement instruments are illustrated in Appendix B. A Phantom v210 high-speed high-resolution camera was used to video record the two-phase flow patterns in the straight pipes upstream of the elbow (at horizontal orientation), downstream of the elbow (at vertical orientation) and through the elbow

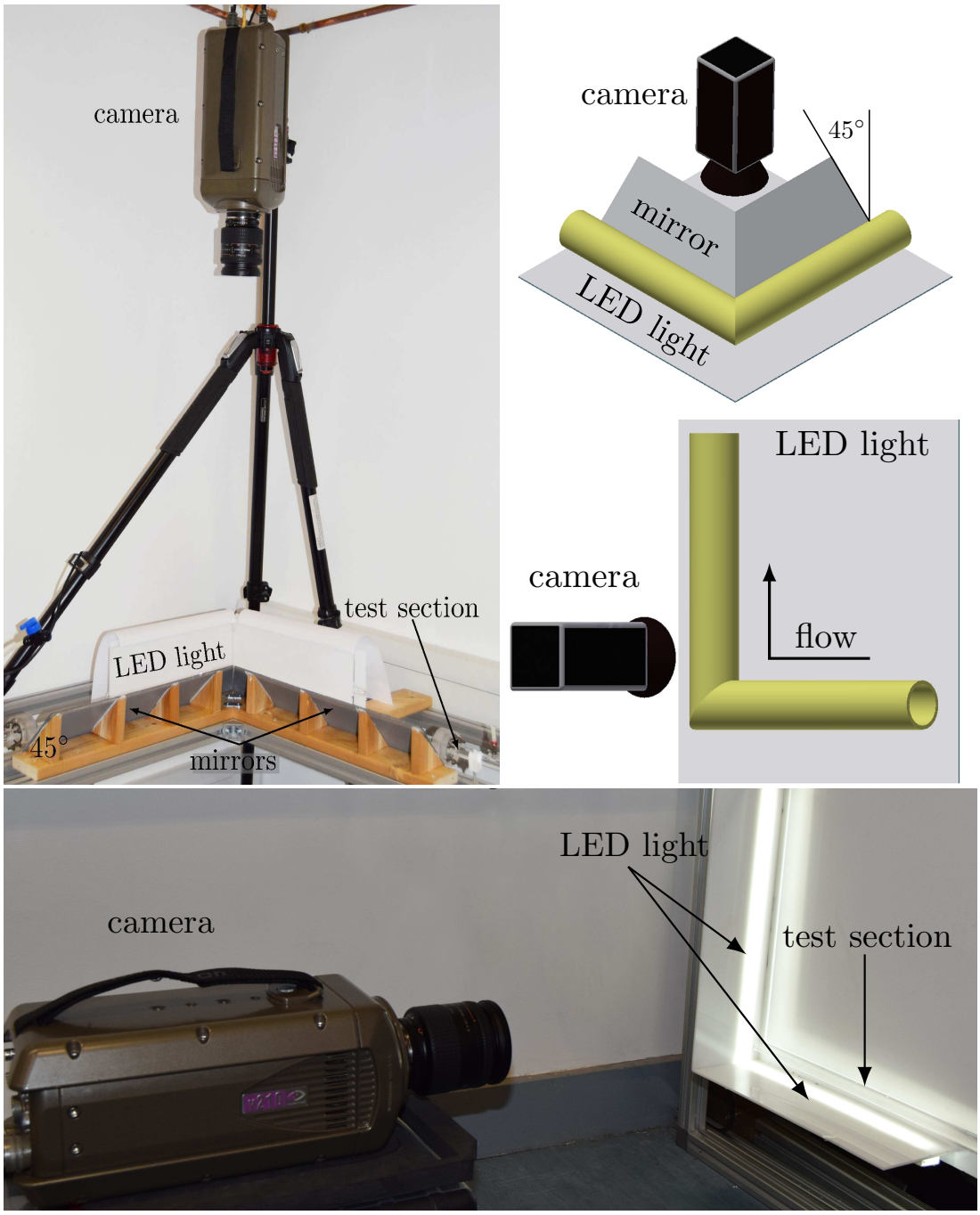

Figure 4.18: Schematic diagrams and pictures of camera position.

at both orientations at 1750 frames per second. White acrylic sheets with white LED light were employed as a monitor background to obtain optimum quality videos. Acrylic mirrors inclined with 45° were located close to the elbow to capture both of the side view and the top view of the flow across the horizontal elbow as illustrated in Figure 4.18. The videos at different flow conditions were analysed to distinguish the observed flow patterns and to investigate the flow regimes behaviour through the elbows for both orientations.

Experimental procedure

This Section includes the experimental procedure of the single-phase and the two-phase flows investigations for horizontal and vertical orientations. Lemmon et al. [88] was used to calculate air and water physical properties at measured temperature and pressure for each experiment. All of the experiments were conducted at about 25°C. The maximum change of the fluid temperature in all the experiments was about 5°C.

In single-phase flow, the pressure was measured along each test section for different flow conditions as listed in Table 4.1.

Table 4.1: Water and air flow rates.

D^* (mm)	$\dot{V}_L^*$ (l/min)	$\dot{V}_G^*$(standard l/min)	$\mathcal{R}e_L$	$\mathcal{R}e_G$
11	4 - 22	5 - 460	8486 - 47522	620 - 63225
16	4 - 32	10 - 500	6016 - 48125	882 - 44114
21	4 - 40	15 - 500	9173 - 45866	1010 - 33669

All of the pressure measurements were started after obtaining a constant mean flow rate. Several experiments were repeated at different dates to check the repeatability of the measurements. The maximum deviation of the measured data across all the repeated experiments was about 0.7%.

In two-phase flow, all experiments were started by regulating the water flow rate to the needed value manually. After obtaining a constant mean water flow, the mixture was created by manually regulating the air flow rate to the needed value by using a needle valve. The data, videos for flow visualization and pressure drop for pressure drop investigations, were then registered after obtaining steady state mixture flow. These steps were repeated for all test sections in horizontal and vertical orientations for different water and air superficial velocities ($j_k^* = \dot{V}_k^*/\mathcal{A}^*$), where $\dot{V}^*$ is the volumetric flow rate, k is the fluid ,L for water and G for air, and $\mathcal{A}^*$ is the pipe cross-sectional area. In the horizontal orientation, five different water superficial velocities were used at D^*=21mm, while three different water velocities were used in the other test sections with D^*=11 and 16mm. About 30, 20 and 15 different air superficial velocities were used at each water velocity at

D^*=21, 16 and 11mm respectively in the ranges that are listed in Table 4.2. In

Table 4.2: Flow parameters in the horizontal configuration.

D^* (mm)	j_L^* (m/s)	j_G^* (m/s)	$\mathcal{R}e_L$	$\mathcal{R}e_G$
11	0.51 - 0.76	0.51 - 33.82	5173 - 10346	293 - 19559
16	0.55 - 0.79	0.26 - 30.59	7945 - 11367	208 - 24956
21	0.297 - 0.68	0.15 - 24.75	5598 - 12782	158 - 26456

the vertical orientation, 5 different water velocities were used for each test section, while 30, 20 and 12 different air velocities were used for each water velocity at D^*=21, 16 and 11mm respectively in the ranges that are listed in Table 4.3. Figure 4.19 shows the flowchart of the experimental procedure for the flow visual-

Table 4.3: Flow parameters in the vertical configuration.

D^* (mm)	j_L^* (m/s)	j_G^* (m/s)	$\mathcal{R}e_L$	$\mathcal{R}e_G$
11	0.68 - 1.02	0.51 - 30.44	6897 - 10346	293 - 17603
16	0.34 - 0.68	0.26 - 33.99	4889 - 9778	208 - 27729
21	0.279 - 0.50	0.15 - 24.75	5598 - 9330	158 - 26456

ization and the pressure drop measurements of two-phase flow. The pressure drop measurements between different measurement stations were repeated at different time intervals to examine the repeatability of the measurements. The maximum deviation between the repeated experiments was less than 5% for all of the test sections in both horizontal and vertical orientations.

Methodology of data reduction procedure

This Section includes the data analysis procedure for single-phase and two-phase pressure drop investigations and the method of the uncertainty analysis.

Single-phase flow

Single-phase pressure drop along the test section were measured to compute the Darcy friction factor $\mathcal{C}_f$, the elbow equivalent length l_{eq}^* and the pressure loss coefficient $\mathcal{K}$ of the sharp elbow. Single-phase Darcy friction factor in straight

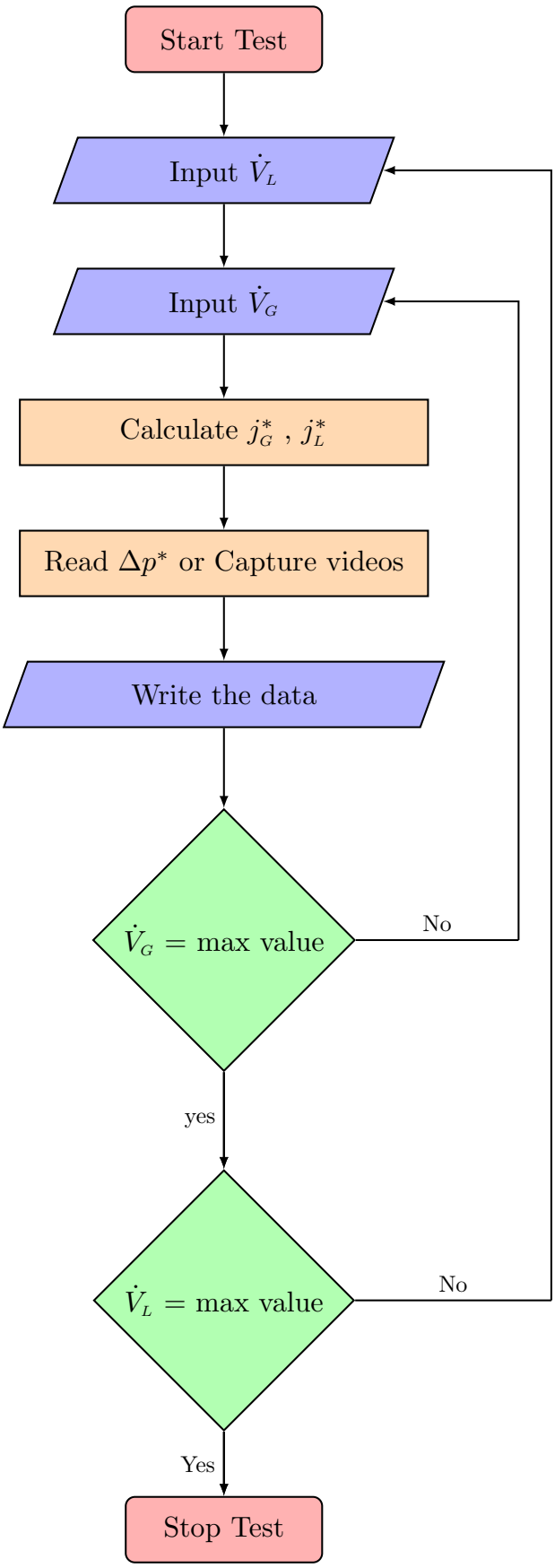

Figure 4.19: Flow chart of experimental procedure for two-phase flow visualization and pressure drop measurements.

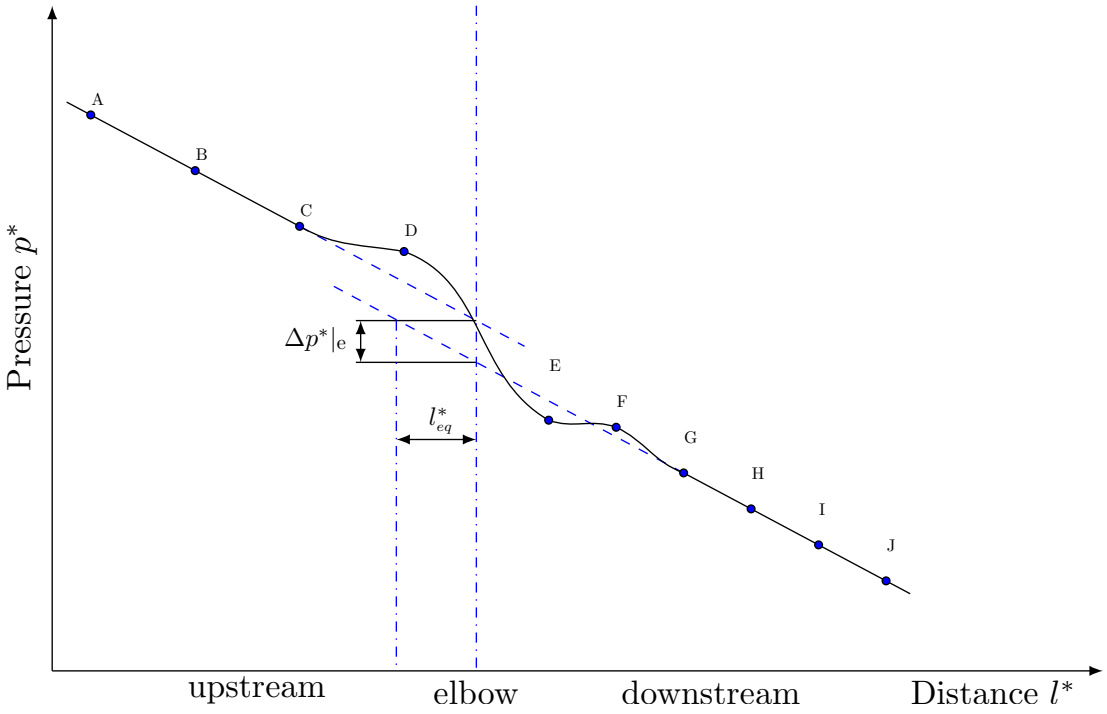

Figure 4.20: Schematic diagram of pressure drop along the test section

pipes $\mathcal{C}_f$ was calculated by using:

$$\mathcal{C}_f = \frac{\Delta p^* D^*}{0.5 \Delta l^* \rho^* \mathcal{U}_b^{*2}}, \tag{4.1}$$

where Δp^* is the measured pressure drop, D^* is the pipe diameter, Δl^* is the distance between the measurement stations, ρ^* is the density of the utilized fluid and $\mathcal{U}_b^*$ is the bulk velocity.

Pressure drop across the elbow was computed by using the pressure drop along the straight pipes upstream and the downstream of the elbow as reported by Ito [13], Crawford et al. [10] and Spedding et al. [17]. Figure 4.20 shows a schematic diagram of the pressure drop along the test section with the presence of the elbow. As displayed in Figure 4.20, the pressure-drop through the elbow was computed as the difference between the intercepts on the vertical axis of the two best-fit straight lines defining the straight-pipe pressure gradients upstream and downstream of locations C and G (dashed blue lines). The scaled equivalent length l^*_{eq} was obtained by subtracting the intercepts of the two best-fit straight lines on the horizontal axis. After obtaining the pressure drop across the elbow, the pressure loss coefficient $\mathcal{K}$ is evaluated by using:

$$\mathcal{K} = \frac{\Delta p^*|_e}{0.5 \rho^* \mathcal{U}_b^{*2}}, \tag{4.2}$$

where $\Delta p^*|_{\mathrm{e}}$ is the pressure drop across the sharp elbow. The equivalent length of the elbow l^*_{eq} was computed by using:

$$l^*_{eq} = \frac{\Delta p^*|_{\mathrm{e}}}{\left(\Delta p^*/\Delta l^*\right)_{up}}, \tag{4.3}$$

where $\left(\Delta p^*/\Delta l^*\right)_{up}$ is the pressure gradient along the straight pipe upstream of the elbow.

Two-phase flow

In two-phase flow investigations, pressure drop measurements along the test sections for both orientations were employed to evaluate the pressure drop across the elbow by applying the same procedure that was used in single-phase flow.

The frictional pressure drop per unit length along the straight portions of the pipe is computed as follows [89, 90]:

$$\left.\frac{\Delta p^*}{\Delta l^*}\right|_{\mathrm{f}} = \left.\frac{\Delta p^*}{\Delta l^*}\right|_{\mathrm{meas}} - \left.\frac{\Delta p^*}{\Delta l^*}\right|_{\mathrm{st}} \sin\theta^*, \tag{4.4}$$

where the angle θ^* is measured with respect to the vertical line, the subscript "meas" denotes the total measured pressure drop per unit length and the subscript "st" indicates the static pressure drop per unit length due to the effect of gravity and defined as:

$$\left.\frac{\Delta p^*}{\Delta l^*}\right|_{\mathrm{st}} = g^* \left[(1-\epsilon)\,\rho^*_{L} + \epsilon\rho^*_{G}\right], \tag{4.5}$$

where ϵ is the gas-phase void fraction, ρ^*_{L} is the density of water and ρ^*_{G} is the density of air. Many empirical correlations were proposed to predict the gas-phase void fraction, like Lockhart and Martinelli [5], Spedding and Chen [91] and Baroczy [92]. The average deviation between the void fraction results by using these correlations, for our flow conditions, was less than ±5%. Therefore, the method of Baroczy [92] was used in our calculations as:

$$\epsilon = \left[1 + \left(\frac{1-x}{x}\right)^{0.74}\left(\frac{\rho^*_{G}}{\rho^*_{L}}\right)^{0.65}\left(\frac{\mu^*_{L}}{\mu^*_{G}}\right)^{0.13}\right]^{-1}, \tag{4.6}$$

where $x{=}\dot{m}^*_{G}/(\dot{m}^*_{G} + \dot{m}^*_{L})$ is the gas-phase mass quality.

Table 4.4: The uncertainty in the measurements instruments.

Device	Model	uncertainty
Water flow meter	FTB-104	±(0.5% of reading)
Water flow meter	FTB-100	±(0.5% of reading)
Absolute pressure transducer	PX309-100G5V	±(0.25% FS BSL)
Diff. pressure transducer	PX409-2.5DWU10V	±(0.08% FS BSL)
Diff. pressure transmitter	PX409-10WDWUI	±(0.08% FS BSL)
Diff. alcohol manometer	Air flow Type 4	±(1% Reading)
Air flow meter	FMA-1612A-V2	±(0.8% Reading + 0.2% FS)
Thermocouple	Type K	±(0.5%)

Uncertainty calculations

There were two main sources of uncertainty: the uncertainty associated with the measurement instruments and the uncertainty in the measured values. The uncertainties of the measurement instruments were provided by the manufacturers, as discussed in Section 4.1.5 and listed in Table 4.4.

The uncertainties in the measured values included the uncertainty of the pipe diameter D^*, the distance between the measurement stations Δl^*, the surface roughness of the pipes, the elbow angles and the fluids physical properties. Each pipe diameter was measured carefully by a micrometer at five different locations with a ±0.1mm maximum error, while the surface roughness of the pipe was measured by a Dektal 150 surface profiler with a ±2% uncertainty. The distances between measurement stations Δl^* were measured with a ±1mm maximum error and the angle of the elbows was measured by an accurate protractor with a ±0.5° uncertainty. The uncertainty in the fluid properties was computed for each experiment by using the NIST Refprop database [88]. The square root of the sum of the sequence method was used to obtain the total uncertainty of a measured quantity $f = f(x_0, .., x_N)$, as follows [93]:

$$\delta f = \sqrt{\sum_{n=0}^{N} \left(\frac{\partial f}{\partial x_n} \, \delta x_n \right)^2}, \tag{4.7}$$

where δx_n is the experimental error associated with the variable x_n.

The uncertainties are indicated by error bars in the graphs of Chapters 5, 6 and

7. For clarity, error bars are only shown for data corresponding to three or four representative points in some figures rather than displaying the error bars for all data points. The average of the absolute error percentage between the predicted and the experimental values was computed by using:

$$\text{average abs. error} = \frac{1}{N}\sum_{1}^{N}\left|\frac{\text{predicted value - experimental value}}{\text{experimental value}}\right| \times 100(\%). \tag{4.8}$$

Chapter 5

Single-phase flow results

This Chapter includes the experimental results of the single-phase pressure drop measurements along straight pipes and across 90° sharp-angled mitre elbows. Section 5.1 reviews the results and discussions of the friction factor in straight pipes. The results and discussions of the pressure drop across 90° elbows are found in Section 5.2, while the measurements of peripheral pressure are included in Section 5.3.

Friction factor in straight pipes

Before studying the local pressure drop due to the elbow, it is essential to verify that the Darcy friction factor of the turbulent flow in the straight pipe upstream of the elbow,

$$\mathcal{C}_f = \frac{2D^*\Delta p^*}{\Delta l^* \rho^* \mathcal{U}_b^{*2}}, \tag{5.1}$$

agrees with well-established empirical correlations for the range of Reynolds numbers of interest in our study. In Equation (5.1) Δp^* is the pressure drop along the straight section of the pipe upstream of the elbow, Δl^* is the distance along which Δp^* is measured, ρ^* is the density of the fluid, $\mathcal{U}_b^* = \dot{m}^*/(\rho^* \mathcal{A}^*)$ is the mean-flow velocity, $\dot{m}^*$ is the mass flow rate, and $\mathcal{A}^*$ is the cross-sectional area of the pipe. Figure 5.1 shows $\mathcal{C}_f$ as a function of the Reynolds number $\mathcal{R}e = \mathcal{U}_b^* D^*/\nu^*$, where ν^* is the kinematic viscosity of the fluid, for the three different pipe diameters and the two fluids. The data are compared with Churchill's [94], Haaland's [95] and McKeon *et al.*'s [96] correlations and with data from experiments and di-

rect numerical simulations [96, 97, 98, 99]. A very good agreement with less than ±5% average error is found. The scatter is almost constant in the whole Reynolds number range, although the estimated uncertainty increases as $\mathcal{R}e$ decreases due to the high uncertainty in the measurement instruments at these ranges of flow conditions. Air and water data have the same average errors.

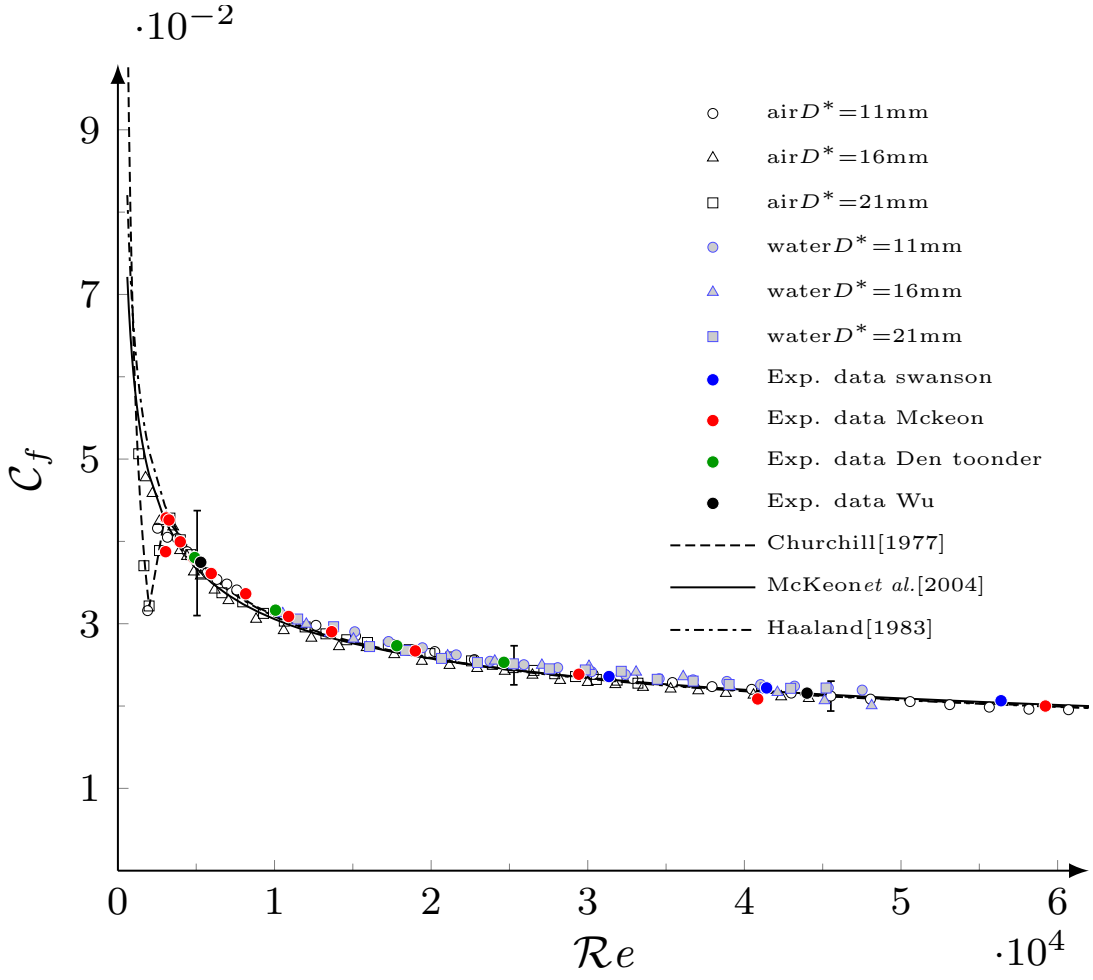

Figure 5.1: Friction factor $\mathcal{C}_f$ as a function of the Reynolds number $\mathcal{R}e$ for flow through straight pipes.

Pressure drop across 90° sharp-angled mitre elbow

Pressure drop across the elbow is computed depending on the pressure distribution along the test section as illustrated in Section 4.3.

Figure 5.2 shows the scaled pressure drop along the test sections and across the mitre elbows for water and air flows. The trends show the independence of the

results on the working fluid and clearly show the local drop due to the elbow. This effect is negligible upstream and downstream of streamwise distances equal to $32.5D^*$ from the elbow (measurement locations C and F, respectively), i.e. where the pressure gradient is solely due to the distributed straight-pipe frictional effects.

As displayed in Figure 5.2, the pressure-drop coefficient $\mathcal{K}$ was computed as the difference between the intercepts on the vertical axis of the two best-fit straight lines defining the straight-pipe pressure gradients upstream and downstream of locations C and F (dashed black lines). The scaled equivalent length $\mathcal{L}$ was obtained by subtracting the intercepts of the two best-fit straight lines on the horizontal axis. The pressure drop across 90° sharp-angled elbows is expressed

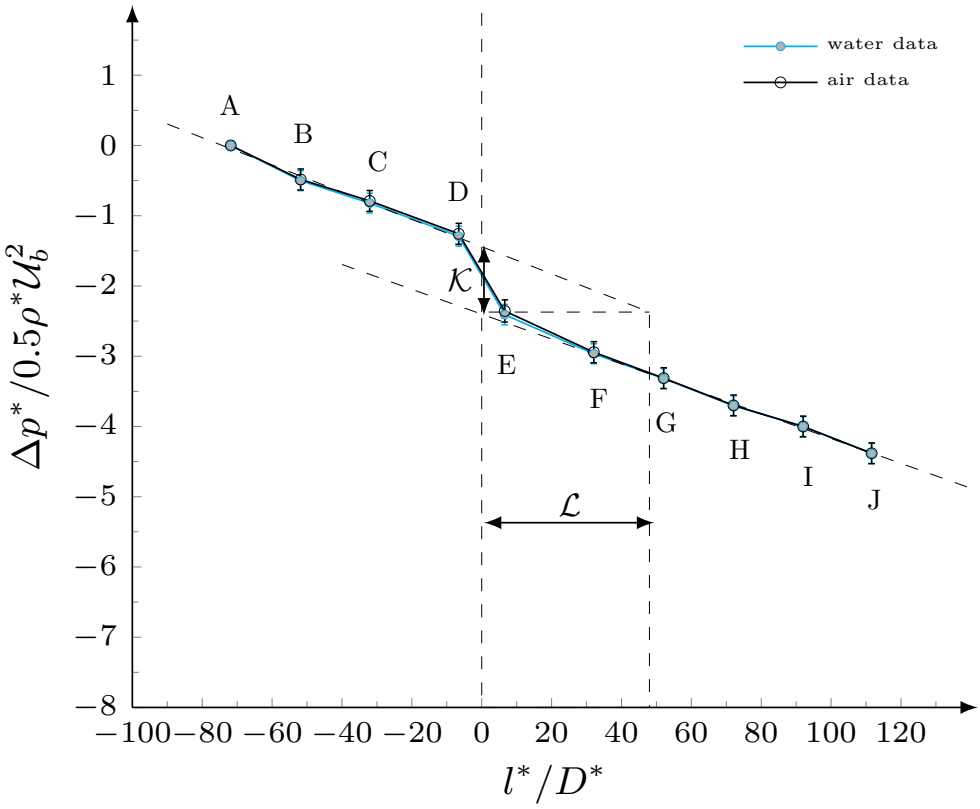

Figure 5.2: Pressure drop relative to the measurement location A along the 21-mm-diameter test section at $\mathcal{R}e$ =22900 for air and water flows. The pressure-loss coefficient $\mathcal{K}$ and the scaled equivalent length $\mathcal{L}$ are indicated.

in terms of pressure loss coefficient $\mathcal{K}$ by using Equation (4.2) as illustrated in Section 4.3.

Figure 5.3 shows $\mathcal{K}$ as a function of $\mathcal{R}e$. To the best of our knowledge, this is

the first time that the dependence of $\mathcal{K}$ on $\mathcal{R}e$ has been presented for 90° sharp-angled mitre elbows. The experimental results show that $\mathcal{K}$ decreases rapidly as $\mathcal{R}e$ increases up to $\mathcal{R}e{\approx}10^4$. For $\mathcal{R}e{>}10^4$ the effect of $\mathcal{R}e$ is moderate as $\mathcal{K}$ keeps decreasing. As remarked by Munson *et al.* [22] it is expected that the coefficient $\mathcal{K}$ displays a weak dependence on $\mathcal{R}e$ at high $\mathcal{R}e$ because the dominance of inertia effects, which is responsible for secondary flows and separation, renders the local pressure drop directly proportional to the dynamic pressure $0.5\rho^*\mathcal{U}_b^{*2}$. A new

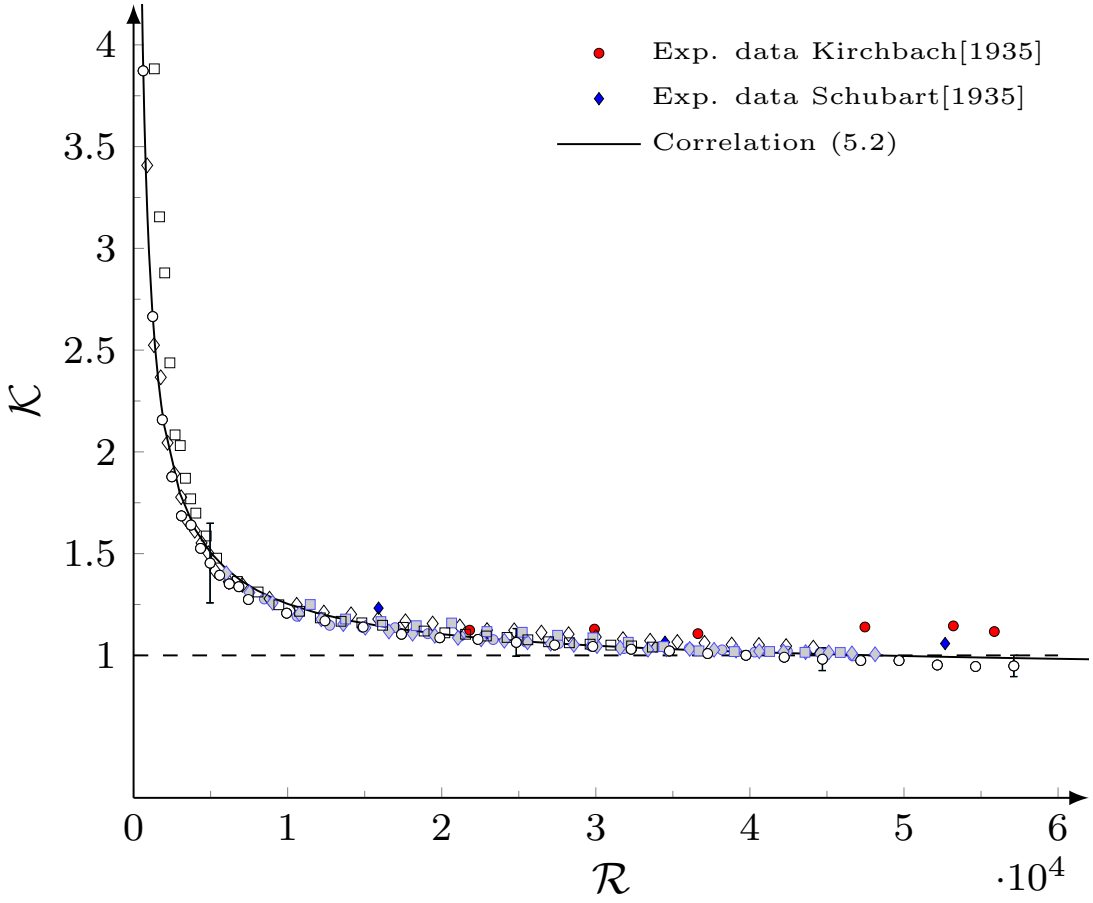

Figure 5.3: Pressure-loss coefficient $\mathcal{K}$ for 90° sharp-angled elbows as a function of the Reynolds number $\mathcal{R}e$. Legends are given in Figure 5.1.

correlation based on our experimental data is proposed:

$$\mathcal{K} = 427.5\mathcal{R}e^{-0.77} + 0.9, \quad 500 \leq \mathcal{R}e \leq 60000. \tag{5.2}$$

Correlation (5.2) fits our experimental data within an average error of ±3%. The experimental data for smooth elbows by Kirchbach [18] and for rough elbows by Schubart [19] are shown for comparison in Figure 5.3. Probably due to the high uncertainty in their experiments, Kirchbach's [18] and Schubart's [19] data do not

show the subtle dependence of $\mathcal{K}$ on $\mathcal{R}e$ in the range $15000<\mathcal{R}e<60000$. They predict a constant $\mathcal{K}=1.1$, whereas our $\mathcal{K}$ values decrease slowly with $\mathcal{R}e$ and are consistently lower than theirs in this $\mathcal{R}e$ range. According to Kirchbach's [18] and Schubart's [19] data, roughness has no effect on $\mathcal{K}$ in this $\mathcal{R}e$ range, arguably because the Reynolds number is large enough for the elbow pressure drop to be caused mainly by the local separation rather than by frictional effects. As for the $\mathcal{C}_f$ data, our $\mathcal{K}$ data show an experimental scatter that is independent of the Reynolds number and of the fluid employed. It would be interesting to extend the range of $\mathcal{R}e$ to verify whether $\mathcal{K}$ reaches a constant value at larger $\mathcal{R}e$ and to quantify this value precisely. According to our measurements, $\lim_{\mathcal{R}e\to\infty}\mathcal{K}=0.9$ appears to be more realistic than the currently adopted $\mathcal{K}=1.1$. It is also important to investigate how $\mathcal{K}$ varies in the laminar-flow limit $\mathcal{R}e\to 0$.

Figure 5.4 shows a comparison between our $\mathcal{K}$ values as a function of $\mathcal{C}_f$ and the predicted $\mathcal{K}$ trend proposed by Crane [25] for turbulent flow conditions. Both Crane's formula [25] and our data predict that $\mathcal{K}$ increases monotonically with $\mathcal{C}_f$, but our data are lower than Crane's [25] in the whole $\mathcal{C}_f$ range. Furthermore, our study reveals that the increase of $\mathcal{K}$ with $\mathcal{C}_f$ is linear only for $0.02<\mathcal{C}_f<0.03$, while the dependence of $\mathcal{K}$ on $\mathcal{R}e$ is more significant for $\mathcal{C}_f>0.03$. In the linear regime, the following relation between $\mathcal{K}$ and $\mathcal{C}_f$ is proposed,

$$\mathcal{K} = 26.92\mathcal{C}_f + 0.42, \quad 0.02 < \mathcal{C}_f < 0.03, \tag{5.3}$$

which fits the experimental data in this range of $\mathcal{C}_f$ within a $\pm 2.5\%$ average error. Crane [25] instead predicts a linear dependence for any value of $\mathcal{C}_f$, i.e. $\mathcal{K}=60\,\mathcal{C}_f$. It is worth noting that our linear Correlation (5.3) does not cross the origin in the $(\mathcal{K},\mathcal{C}_f)$ plane, while Crane's [25] does. If the straight line passed through the origin, the bulk velocity $\mathcal{U}_b^*$ could be simplified from the linear relationship upon re-writing the quantities in dimensional form. The elbow pressure drop could be computed by simply measuring the straight-pipe pressure drop and this would be very useful for engineering applications.

Figure 5.4 also shows that Kirchbach's [18] and Schubart's [19] data are also much lower than Crane's [25] predicted values, which is somewhat surprising because Crane's correlation [25] is based on Kirchbach's [18] and Schubart's [19] results.

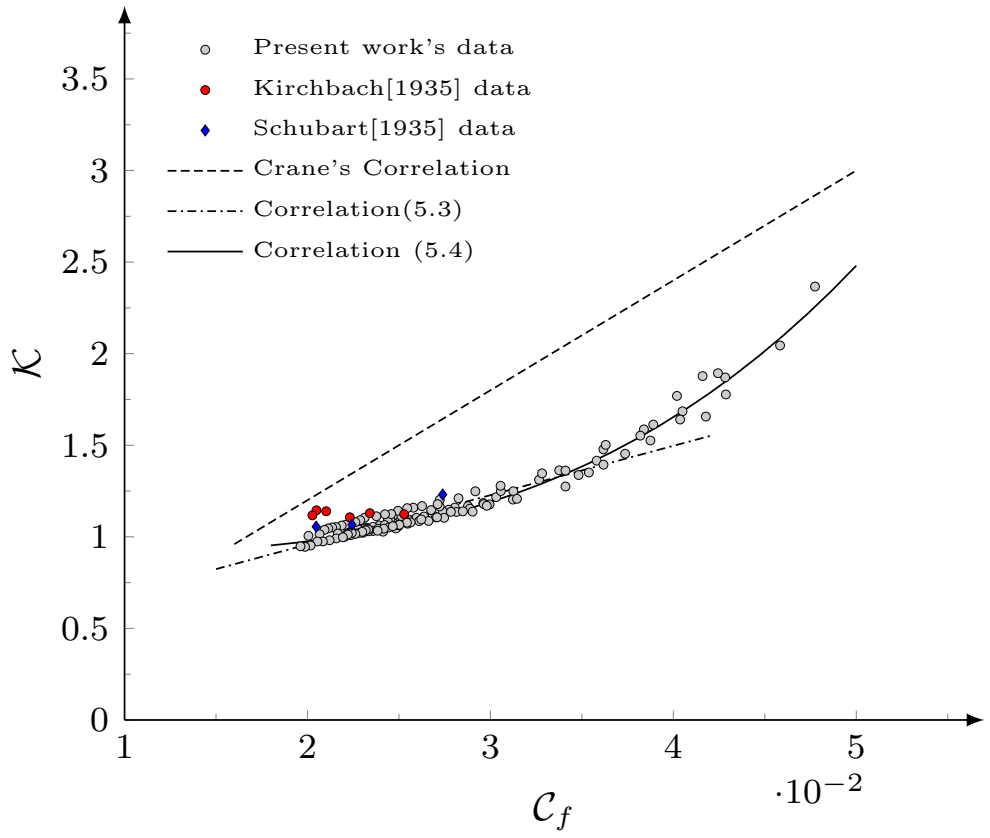

Figure 5.4: Pressure-loss coefficient $\mathcal{K}$ for sharp-angled elbows as a function of $\mathcal{C}_f$.

For the whole range of $\mathcal{C}_f$ values, a new correlation relating $\mathcal{K}$ and $\mathcal{C}_f$ is proposed for flows across 90° sharp-angled elbows:

$$\mathcal{K} = 32980\,{\mathcal{C}_f}^{3.32} + 0.9, \quad 0.02 < \mathcal{C}_f < 0.05. \tag{5.4}$$

Correlation (5.4) fits the experimental data within a ±1.9% average error. If the well-known correlation for the turbulent friction coefficient given by Blasius, $\mathcal{C}_f$=0.3164 $\mathcal{R}e^{-0.25}$ [23], is substituted into our Correlation (5.4), one obtains $\mathcal{K}$=722.8$\mathcal{R}e^{-0.83}$ + 0.9, which only differs from our Correlation (5.2) by less than ±2%, which is smaller than the experimental error of our $\mathcal{K}$ and $\mathcal{C}_f$ data.

The equivalent length to diameter ratio,

$$\mathcal{L} = \frac{l^*_{eq}}{D^*} = \frac{\Delta l^* \Delta p^*_e}{D^* \Delta p^*}, \tag{5.5}$$

where the equivalent length l^*_{eq} is the length of the straight pipe that would generate the same pressure drop as the elbow at the same bulk Reynolds number, represents another way to express the pressure loss in elbows and pipe bends. In Equation (5.5), Δl^* and Δp^* are defined as in Equation (5.1). As shown in Figure 5.5, $\mathcal{L}$ varies between 35 and 65. It decreases sharply up to $\mathcal{R}e$=7000,

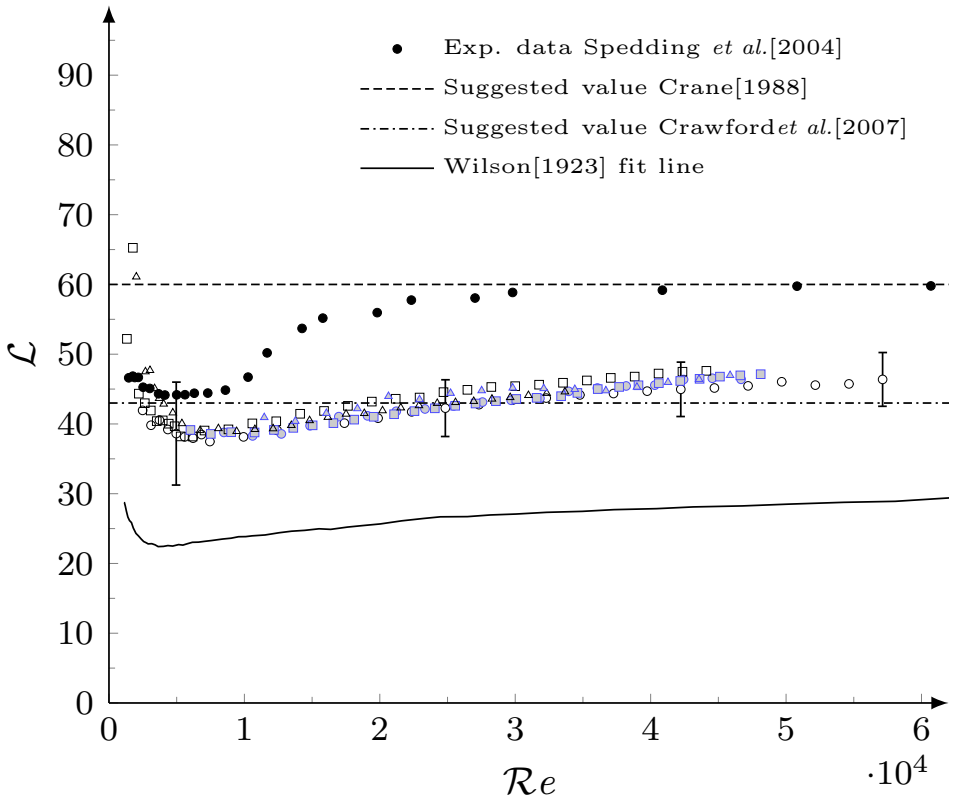

Figure 5.5: Equivalent length to diameter ratio $\mathcal{L}$ for sharp-angled elbow as a function of $\mathcal{R}e$. The symbols are given in Figure 5.1.

then increases slowly with $\mathcal{R}e$ and appears to approach the asymptotic value $\mathcal{L}$=45. Our data are in the middle of the experimental data for 90° round elbows by Wilson *et al.* [14] (C=1) and Spedding *et al.* [17] (C=0.65). The dashed line indicates the constant $\mathcal{L}$=60 suggested by Crane [25], which matches Spedding *et al.*'s data [17] at large Reynolds number. The dash-dotted line denotes the constant $\mathcal{L}$=43 proposed by Crawford *et al.* [10], which shows the best agreement with our results. It is thus confirmed that $\mathcal{L}$ depends strongly on the elbow curvature ratio C and only mildly on $\mathcal{R}e$ for $\mathcal{R}e$>40000 [13, 9, 10, 15].

Measurement of peripheral pressure

Figure 5.6 shows scaled air pressure measurements at different angles (0°, 90° and 270°) around the periphery of the 16-mm-diameter pipe at four different stations upstream and downstream of the elbow and at four Reynolds numbers. The experimental data show that the peripheral pressure upstream and downstream of the elbow is axially symmetric at all the tested locations. As shown in Figure 4.11, the closest locations D and E are at a distance of $7D^*$ upstream and downstream

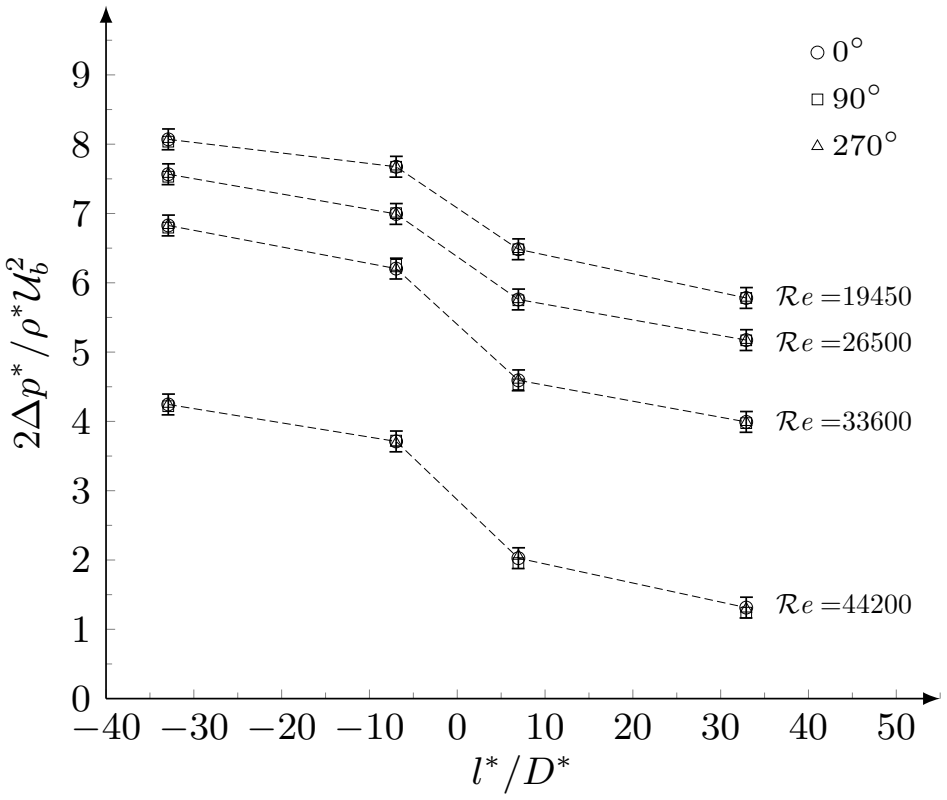

Figure 5.6: Air-flow pressure drop at different angles around the pipe periphery at stations C, D, E and F of the 16-mm-diameter test section at different $\mathcal{R}e$.

of the elbow, respectively, which agrees with the result by Ito for 90° round elbows [13].

Chapter 6

Two-phase flow visualization results

This Chapter reviews the results and discussions of two-phase flow visualization along straight pipes and through 90° sharp-angled mitre elbows for horizontal and vertical orientations.

Two-phase flow in straight pipes

Four flow patterns were observed in the horizontal configuration for 275 flow conditions of Table 4.2: plug, slug, slug-annular and annular flows. Figure 6.1 presents instantaneous snapshots of these flow patterns in the horizontal pipe section upstream of the elbow for D^*=21mm, j_L^*=0.495 m/s and different j_G^*.

Three flow patterns, slug, churn and annular flows, were recorded in the vertical riser at a distance of $100D^*$ downstream of the elbow for 338 flow conditions for air and water superficial velocities in the ranges listed in Table 4.3. Figure 6.2a shows instantaneous snapshot of the two-phase flow patterns in the vertical pipe with D^*=21mm for j_L^*=0.279m/s and different j_G^*. The membrane flow structure, discovered by Milan et al. [47] in vertical downward flows, has been observed for the first time in the present study in the vertical upward flow downstream of the elbow as a result of the coalescence of the bubbles after their division through the elbow. Figure 6.2b shows pictures of single and multiple membrane flow in the pipe with D^*=21mm for j_G^*=0.15 m/s and different j_L^*. Up to four

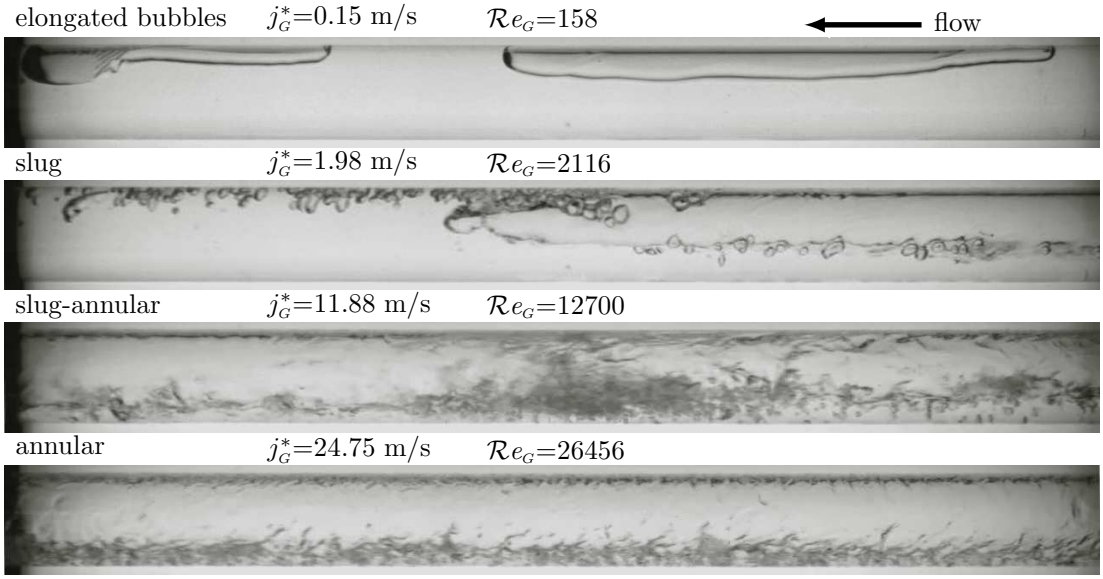

Figure 6.1: Flow patterns in horizontal pipe sections upstream of the elbow for D^*=21mm, j_L^*=0.495 m/s, $\mathcal{R}e_L = \rho_L^* j_L^* D^* \pi/(4\mu_L^*)$=5598 and different j_G^*. The Reynolds number for air is defined as $\mathcal{R}e_G = \rho_G^* j_G^* D^* \pi/(4\mu_G^*)$. The densities of the fluids are ρ_k^* and the dynamic viscosities are μ_k^*.

membranes were observed in a single air slug, often almost equally spaced along the vertical direction. Milan et al. [47] observed the membrane flow at a maximum water velocity of 0.41 m/s, while we recorded the presence of these structures at higher water velocities, i.e. up to j_L^*=1.02 m/s, which correspond to higher Reynolds numbers based on j_L^* because our three diameters are larger than Milan et al.'s, i.e. D^*=8.8mm. Figure 6.3 represents the observed flow patterns in the horizontal straight pipes on the Mandhane et al. map [1], while Figure 6.4 shows the patterns in the vertical straight pipes on the Hewitt and Roberts map [2]. We have chosen these maps to display our experimental data graphically because they were proposed to cover a wide range of pipe diameters, including ours. The comparison is better for the data for the vertical orientation in Figure 6.4 than for the data for the horizontal orientation in Figure 6.3.

The dimensional analysis in Appendix C shows that the patterns of an incompressible isothermal air-water flow can be expressed in scaled form in terms of only three non-dimensional parameters, i.e. the Reynolds number for water $\mathcal{R}e_L = \dot{m}_L^*/(\mu_L^* D^*) = \rho_L^* j_L^* D^* \pi/(4\mu_L^*)$, the Reynolds number for air $\mathcal{R}e_G = \dot{m}_G^*/(\mu_G^* D^*) = \rho_G^* j_G^* D^* \pi/(4\mu_G^*)$, and the Froude number for water $Fr_L = \dot{m}_L^*/(\sqrt{g^*} D^{*5/2} \rho_L^*)$, where $\dot{m}_L^*$, $\dot{m}_G^*$ and μ_L^*, μ_G^* are the mass flow rates and viscosities of the two fluids, and

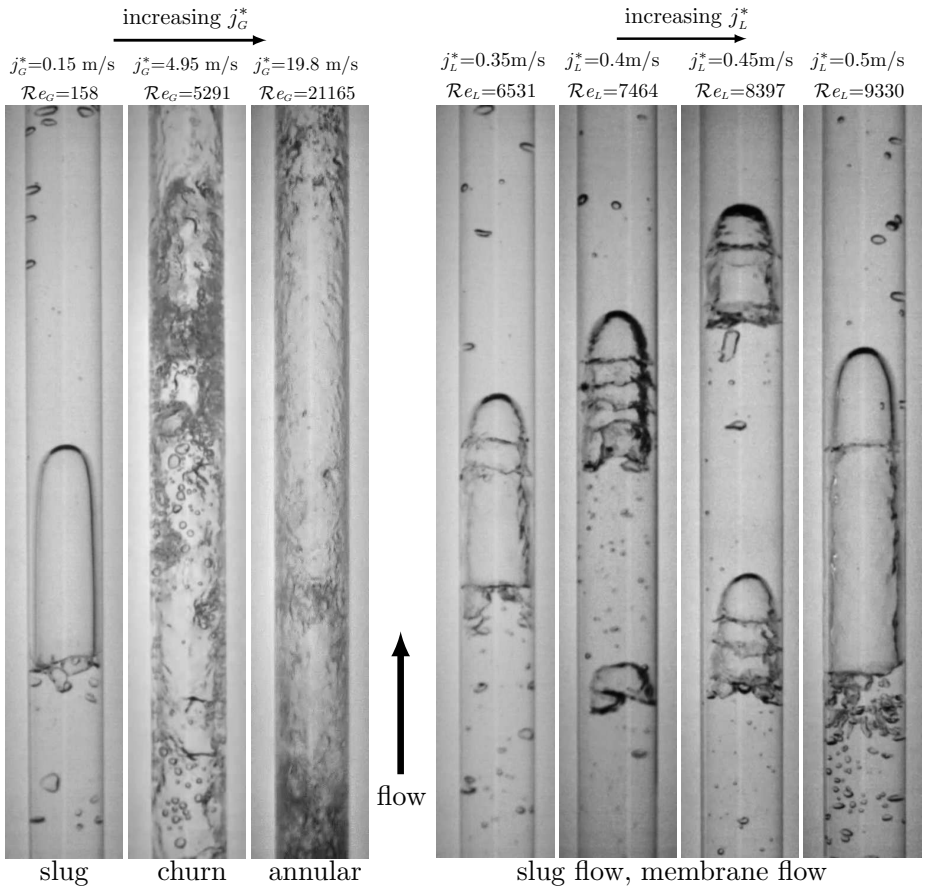

(a) Patterns for j_L^*=0.279 m/s. **(b)** Membrane flow for j_G^*=0.15m/s.

Figure 6.2: Flow patterns in vertical pipe section downstream of the elbow for D^*=21mm, (a) $\mathcal{R}e_L$=5598 and (b) $\mathcal{R}e_G$=159.

g^* is the gravitational acceleration. The analysis demonstrates that only three parameters are necessary because for incompressible isothermal air-water flows the other scaled parameters, the ratio of densities and the ratio of viscosities, are constant. For a constant Froude number, a rigorous non-dimensional representation of incompressible constant-property air-water flow patterns is therefore a map in the $(\mathcal{R}e_G, \mathcal{R}e_L)$ plane.

We can then express the dimensional maps in Figures 6.3 and 6.4 in terms of $\mathcal{R}e_L$ and $\mathcal{R}e_G$ by assuming that the effect of Froude number is negligible. This hypothesis has been largely verified by experimental works in the horizontal case at sufficiently high mass flow rates of both fluids, which avoid the stratified flow regime where gravity plays a decisive role [6]. This is the case of our experiments because all our data points are on the upper half of the horizontal-flow Mandhane map, as clearly shown in Figure 6.3. In the vertical-flow case, Spedding and

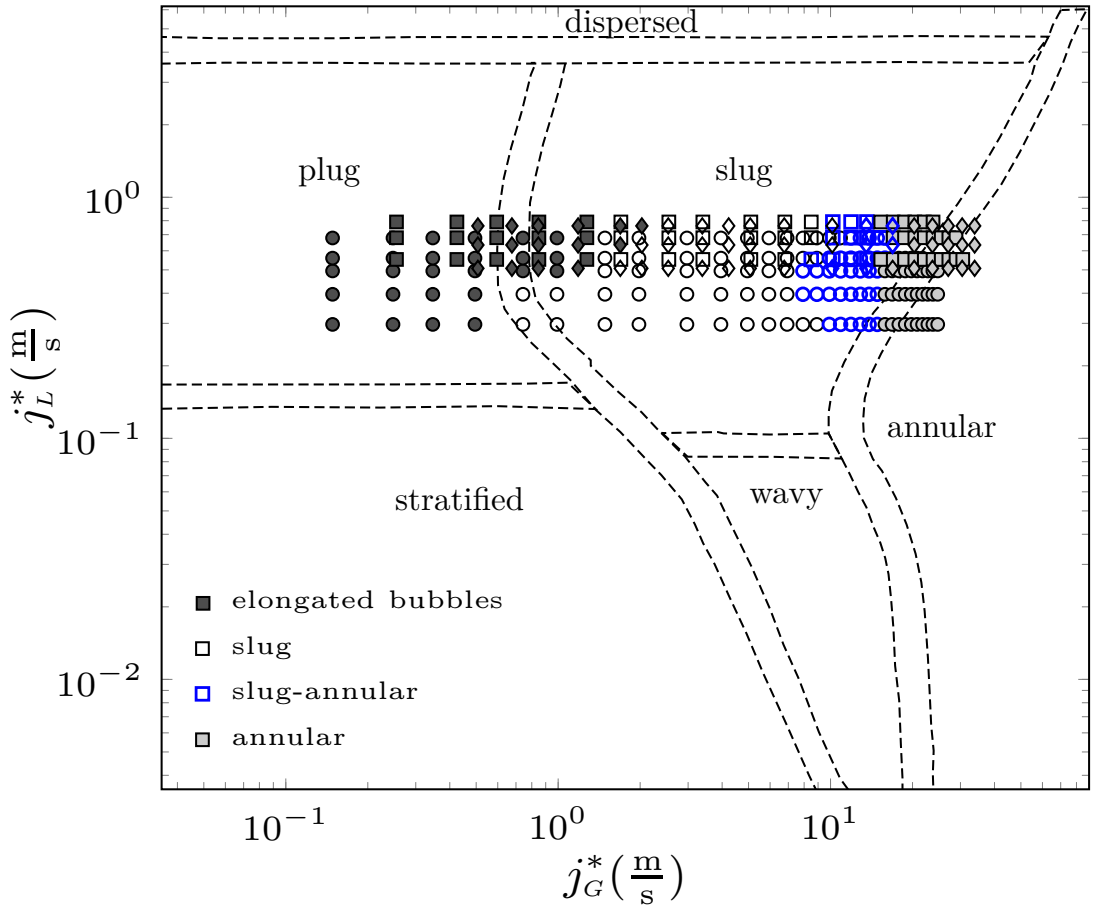

Figure 6.3: Comparison between the detected flow patterns in horizontal pipe sections (represented by the symbols) with the prediction given by the Mandhane et al. map [1] for D^*=21mm (○), D^*=16 mm (□), and D^*=11mm (◇).

Nguyen [100] (refer to discussion of their figure 3 on page 785) showed that, in the Froude number range of interest for our work, i.e. $0.5 \leq Fr_{L} \leq 2.5$, gravity has a mild effect on the flow patterns, especially on the slug-flow regime.

To rescale the maps in terms of $\mathcal{R}e_{L}$, $\mathcal{R}e_{G}$, the velocities j_{L}^*, j_{G}^* at the boundaries between the regions distinguishing the flow patterns and the average value of our pipe diameters are used to compute $\mathcal{R}e_{L}$ and $\mathcal{R}e_{G}$. The rescaled Mandhane et al. and Hewitt and Roberts maps are displayed in Figures 6.5 and 6.6. The rescaled Mandhane et al. map in Figure 6.5 shows a slight improvement for the prediction across the boundary between the plug and slug regions as fewer symbols representing the plug flow fall in the slug-flow region and no symbols representing the slug flow are confined in the strip dividing the two regions. This is instead the case in the dimensional Mandhane et al. map of Figure 6.3. In the rescaled Hewitt and Roberts map in Figure 6.6, all the symbols fall more clearly within

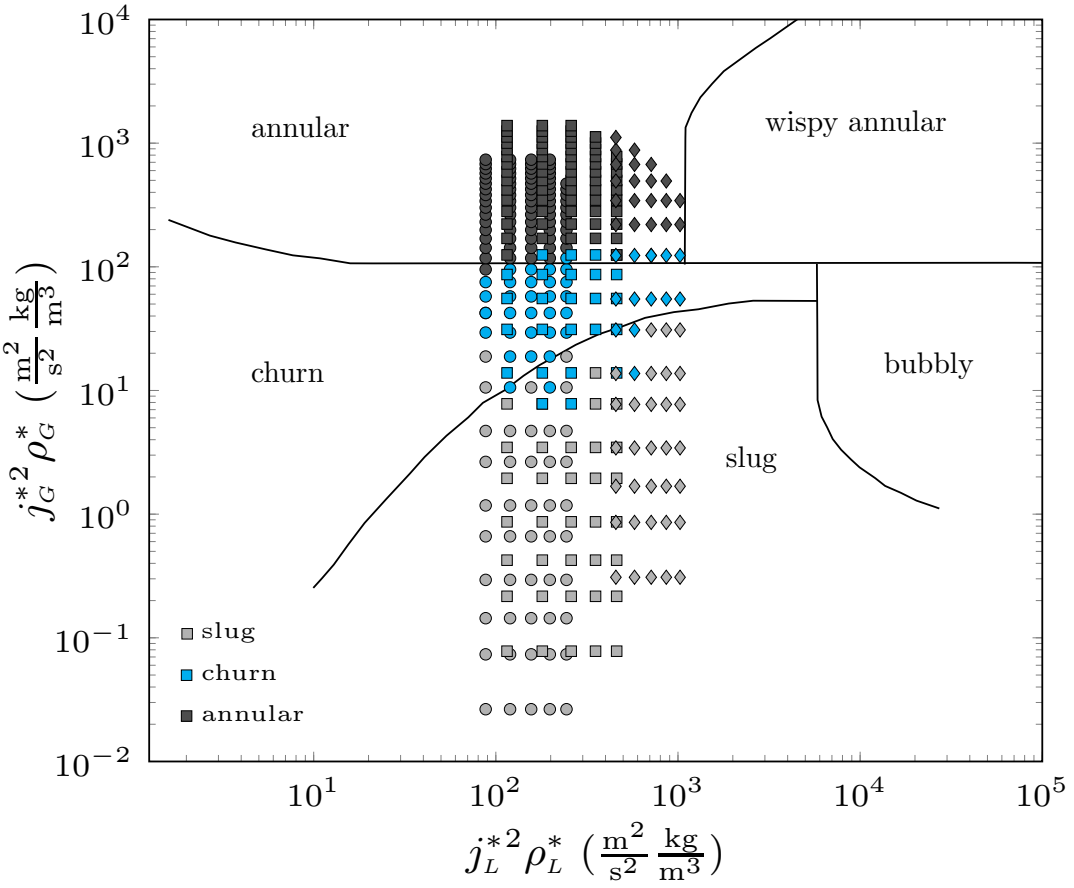

Figure 6.4: Comparison between the observed flow patterns in the vertical straight pipe sections with the prediction given by the Hewitt and Roberts map [2]. The symbols indicate the same diameters as in Figure 6.3.

the predicted regions as they are more clustered together than in the dimensional map.

Figure 6.7 shows the map obtained by Milan et al. [47] to identify the regions in the parameter space where the membrane flow was observed for vertical downward flow. Because our pipe diameters are different from Milan et al.'s, we show the map in non-dimensional form. As for the discussion of Figure 6.2, almost all the flow conditions for which we detected the membrane flow lie in a higher range of $\mathcal{R}e_L$, where Milan *et al.* did not observe this flow.

Two-phase flow across the mitre elbow

Two-phase flow patterns through 90° sharp-angled mitre elbows have been investigated visually to document the behaviour of the flow regimes through the sharp bend caused by the interaction of different forces, like the centrifugal force, the

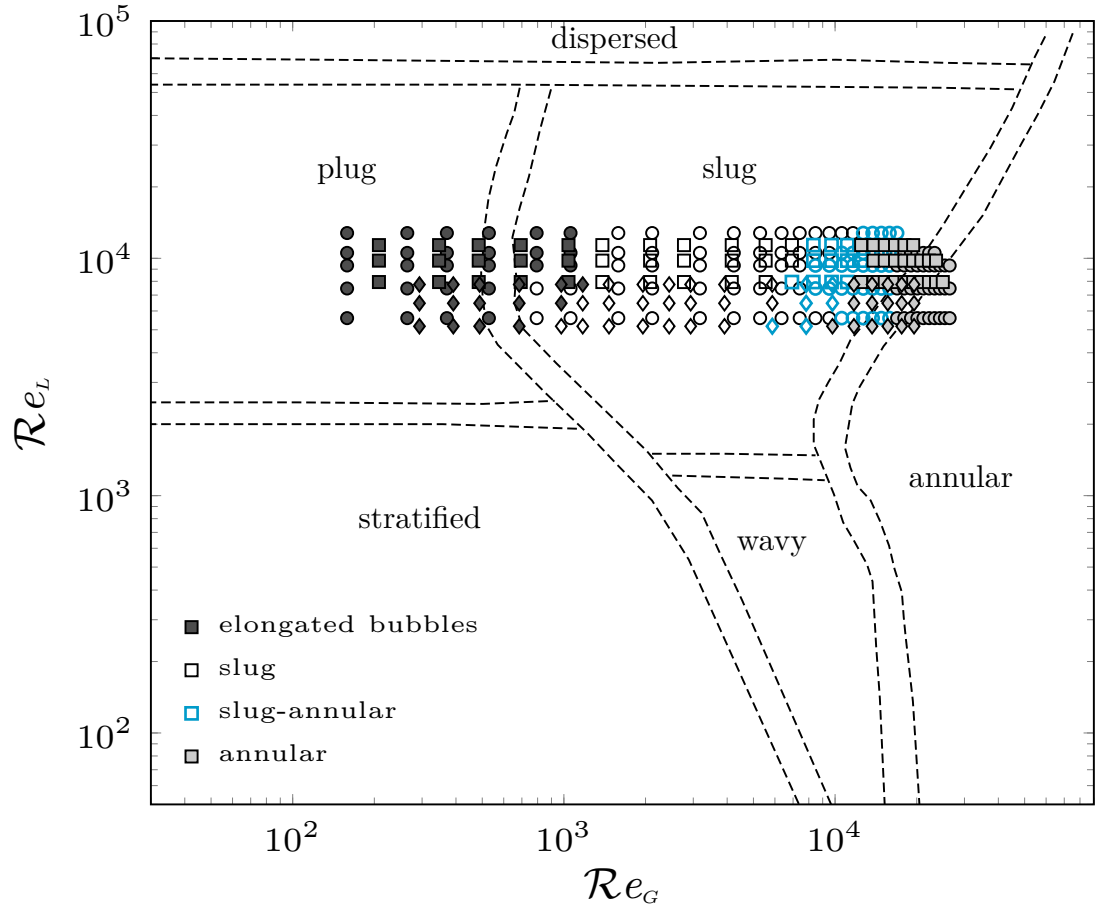

Figure 6.5: Comparison between the observed flow patterns in horizontal straight pipes with the prediction given by the rescaled Mandhane et al. map [1]. The symbols indicate the same diameters as in Figure 6.3.

gravity force, and the buoyancy force, which acts primarily in the vertical orientation. When the elbow was positioned vertically, we investigated the horizontal to vertical upward flow, which is one of four possible flow orientations for this geometry, the others being the horizontal to vertical downward flow, the vertical upward to horizontal flow, and the vertical downward to horizontal flow.

Horizontal orientation

For $\mathcal{R}e_G$<200 in the horizontal orientation, the plug flow is not affected by the elbow due to the balance between the secondary flow and the gravity. The elongated air bubbles, observed for 200<$\mathcal{R}e_G$<3000 in plug and slug flows, divide into two or more bubbles as the flow passes through the elbow, as shown in Figure 6.8 in the pipe with D^*=21mm. The disruption of the bubbles is caused by the flow separation and the strong secondary flow across the elbow. The divided bub-

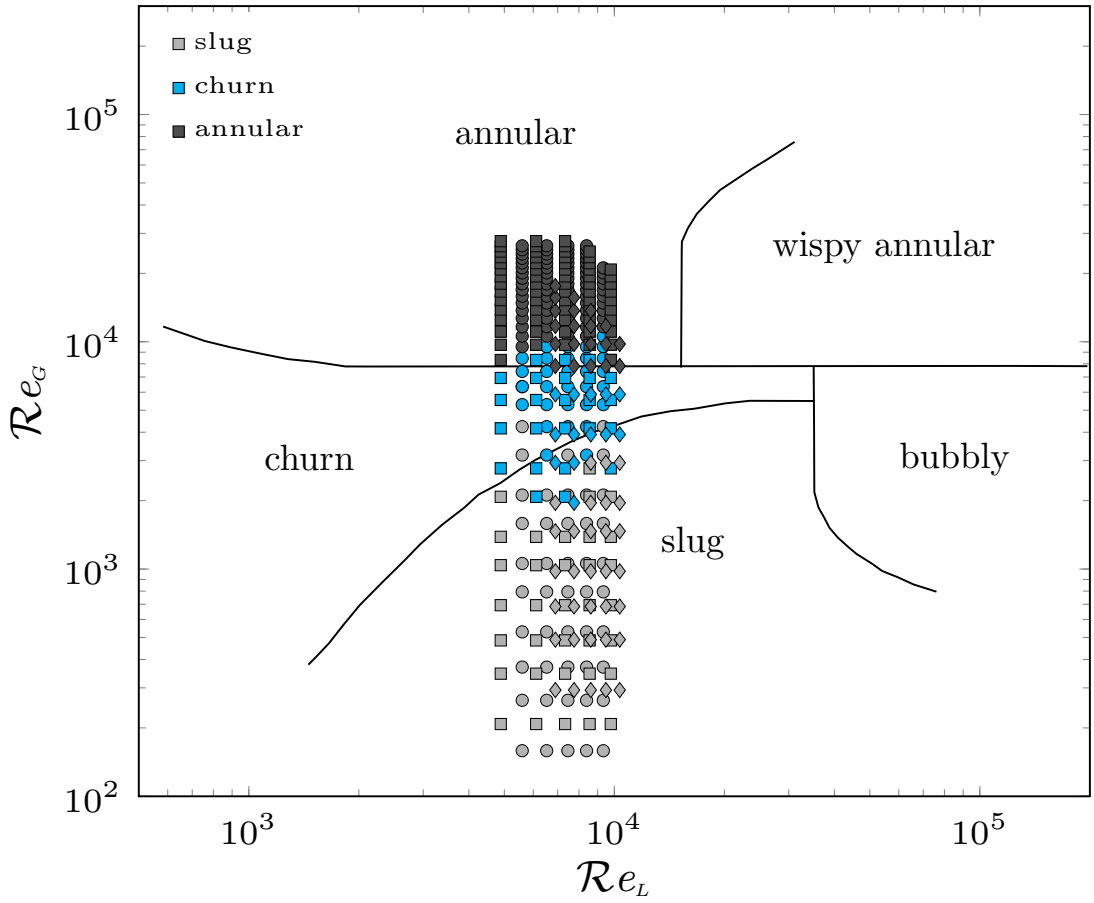

Figure 6.6: Comparison between the observed flow patterns with the non-dimensional Hewitt and Roberts map [2]. The symbols indicate the same diameters as in Figure 6.3.

bles often merge downstream of the elbow to recover the unperturbed regimes upstream of the elbow as the centrifugal force vanishes downstream of the bend, similar to the results of Chen et al. [44] in horizontal return bends. At higher air velocities, $3000<\mathcal{R}e_G<20000$, slug and slug-annular flows suddenly become annular downstream of the elbow due to the centrifugal effects dominating over the gravity effects. This annular flow downstream of the elbow is different from the annular flow in straight pipes because it is swirling as the water layers move in rotational motion around the air flow core and along the pipe periphery, while the layers in straight pipe annular flow move parallel to the pipe axis. The flow then recovers its original pattern approximately $60D^*$ downstream of the elbow. Figure 6.9 shows the flow change from slug to swirling annular through a D^*=21mm horizontal elbow. This phenomena was reported by Chen et al. [44] and Wang et al. [32, 46] in horizontal 180° bends at superficial velocities larger than ours because the secondary flow in 90° sharp-angled mitre elbows is stronger than that

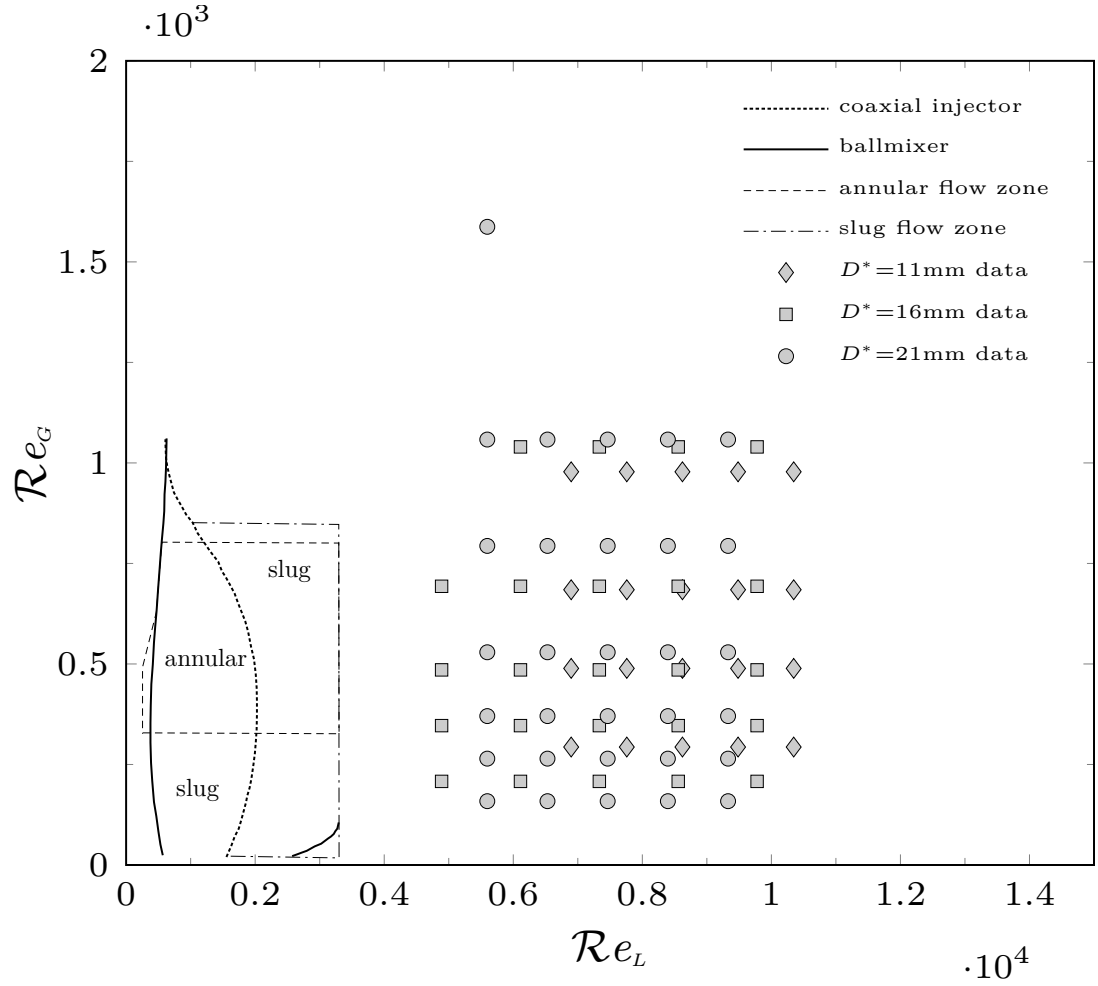

Figure 6.7: Comparison between the experimental data and non-dimensional Milan et al. [47]'s membrane flow map.

in round bends for similar conditions.

For $\mathcal{R}e_G$>20000 the flow upstream of the elbow is annular and has a thick bottom water layer. Downstream of the elbow it is still annular but it is characterized by a constant-thickness axially symmetrical water layer because the inertia of the secondary flow and the centrifugal force dominate over the gravity effects. Like in the case in Figure 6.8, the water layers of the annular flow downstream of the elbow swirl around the pipe periphery before recovering to the standard, non-rotating annular flow farther downstream of the elbow (after approximately $60D^*$). Figure 6.10 illustrates this phenomenon through the D^*=21mm horizontal elbow for different flow conditions. Two-phase flow patterns through horizontal mitre elbows are represented for the first time in terms of the non-dimensional Mandhane et al. map [1], shown in Figure 6.11. This novel representation is useful because it visually combines information on the flow regime upstream of

Figure 6.8: Bubble division and coalescence in the horizontal elbow with D^*=21mm, $\mathcal{R}e_L$=5598 and $\mathcal{R}e_G$=1058.

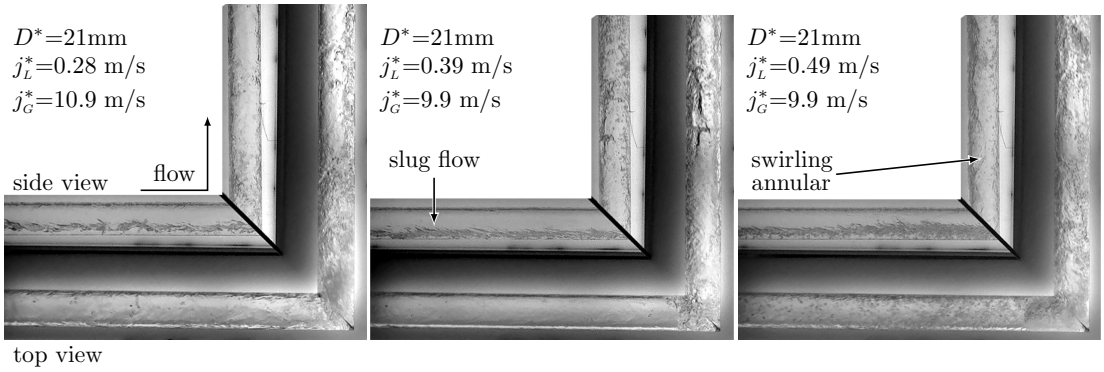

Figure 6.9: Change from slug flow to swirling annular flow across the horizontal elbow with D^*=21mm. Left photo: $\mathcal{R}e_L$=5598 and $\mathcal{R}e_G$=11641. Middle photo: $\mathcal{R}e_L$=7464 and $\mathcal{R}e_G$=11641. Right photo: $\mathcal{R}e_L$=9330 and $\mathcal{R}e_G$=10582.

the elbow, given by the location of the symbols in the Mandhane et al. regions, with the information on the change of the flow regimes as the fluids move across the elbow, denoted by the colour of the symbol.

Horizontal to vertical upward orientation

For $\mathcal{R}e_G$<1000, the intermittent flow patterns (plug and low-j_G^* slug) entering the horizontal part of the elbow change to slug flow in the riser downstream of the elbow due to the effect of gravity. In the upward flow, a liquid-phase reverse downward flow may occur for these flow conditions. This reverse water

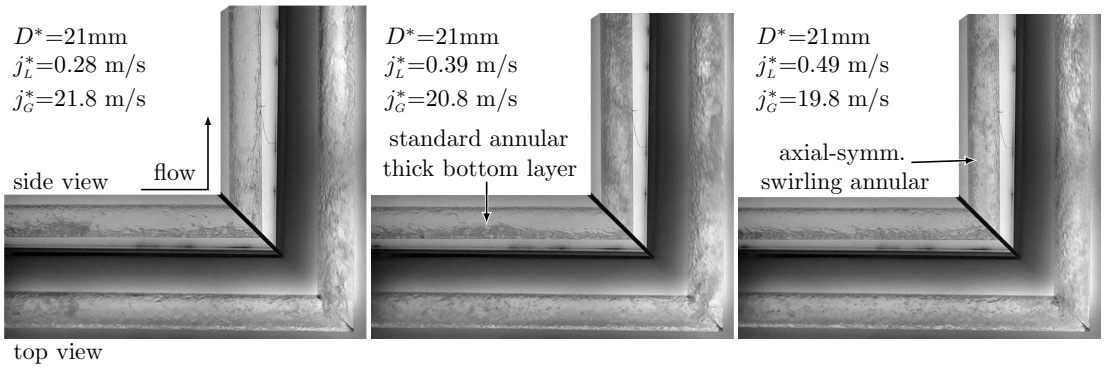

Figure 6.10: Change from annular flow to swirling annular flow across the horizontal elbow with D^*=21mm. Left photo: $\mathcal{R}e_L$=5598 and $\mathcal{R}e_G$=23281. Middle photo: $\mathcal{R}e_L$=7464 and $\mathcal{R}e_G$=22223. Right photo: $\mathcal{R}e_L$=9330 and $\mathcal{R}e_G$=21165.

flow splits the air slugs into two or more bubbles downstream of the elbow. The divided bubbles coalesce downstream of the elbow, often resulting in a membrane flow structure. This behaviour was reported by Wang et al. [43] downstream of vertical 180° bend with upward flow and by Milan et al. [47] in vertical straight pipe with downward flow. Figure 6.12 shows this phenomenon in the vertical elbow with D^*=21mm at different times. The phenomenon of flow reversal and bubble division were reported by Hsu et al. [38] in 90° round elbows and Wang et al. [43] in 180° bend at velocities higher than ours because the secondary flow, which is the main cause for this phenomenon, increases with the decrease of curvature radius of the elbow at the same flow conditions, as also mentioned by Wang et al. [32] and Wang and Mayinger [101].

For $1000<\mathcal{R}e_G<3000$, the slug flow upstream of the elbow remains such in the vertical pipe downstream of the elbow, but it changes character. In the horizontal pipe upstream of the elbow, the air slugs occur in the top part of the pipe while thin water layers appear at the bottom of the pipe. Downstream of the elbow in the vertical pipe, the air slugs move in the centre of the pipe while thin liquid films occur between the slugs and the pipe wall. At higher j_G^*, i.e. for $3000<\mathcal{R}e_G<10000$, the slug flow converts to churn flow through the elbow, as shown in Figure 6.13 for the elbow of D^*=21mm at j_L^*=0.297 m/s. At higher j_G^*, $\mathcal{R}e_G>10000$, the slug-annular and annular flows in the horizontal pipe upstream of the elbow change to swirling annular as the fluids pass through the elbow due to the centrifugal force and the secondary-flow effects dominating over the gravity effects, similar to the results of Wang et al. [43] in vertical 180° round elbows. As for the

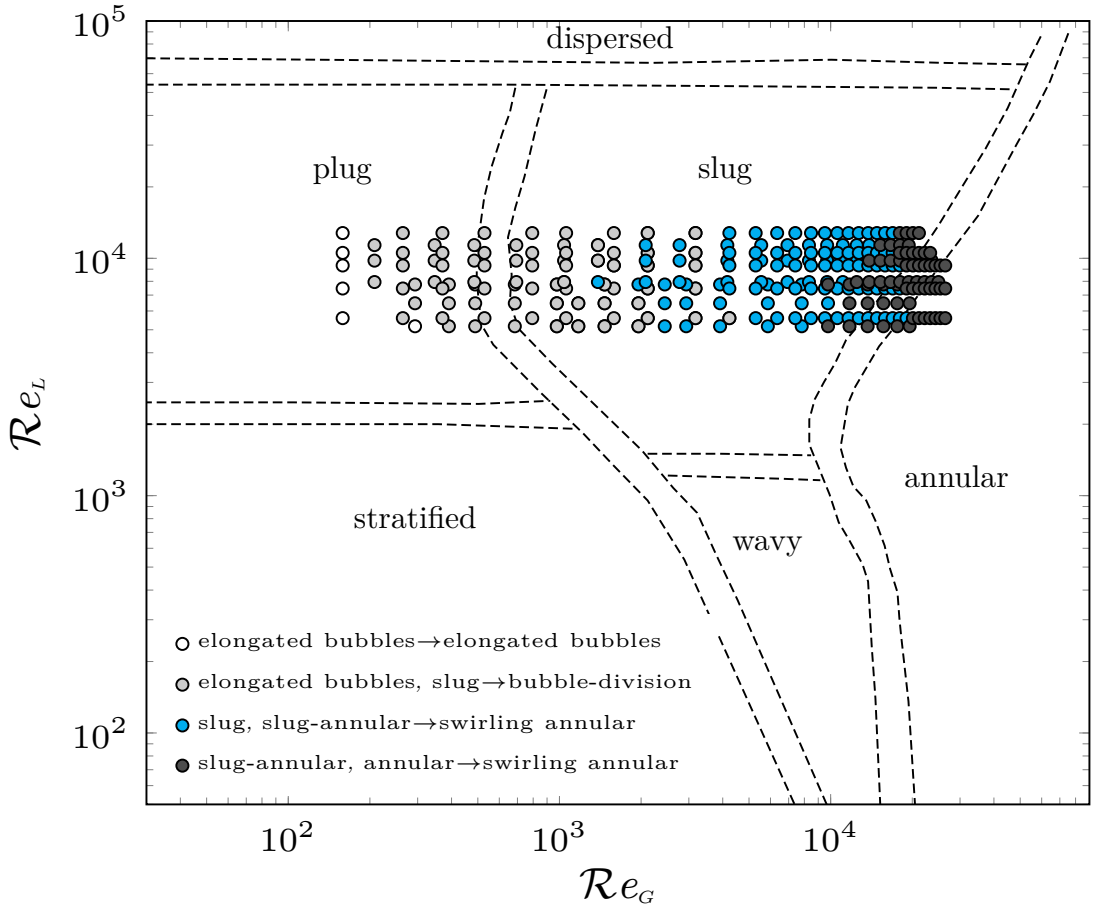

Figure 6.11: Representation of the two-phase flow patterns through the mitre elbows in the horizontal orientation on the non-dimensional Mandhane et al. map [1]. The flow regime upstream of the elbow are denoted by the location of the symbols in the Mandhane regions, while the flow regimes downstream of the elbow are indicated by the colour of the symbol.

behaviour of the flow across the elbow in the horizontal configuration, the water layers of the swirling annular flow downstream of the elbow rotate around the pipe periphery before recovering to the standard annular flow at a distance of about $60D^*$ downstream of the elbow. The annular flow enters the horizontal leg of the vertical elbow with a thicker water layer at the bottom of the pipe and changes to a swirling annular flow with an axially symmetrical water-layer thickness downstream of the elbow, as shown in Figure 6.15 for the D^*=21mm elbow. Similar to the map of Figure 6.11, the air-water flow patterns through elbows in the horizontal to vertical upward position are represented for the first time on the rescaled Mandhane et al. map [1], as shown in Figure 6.16.

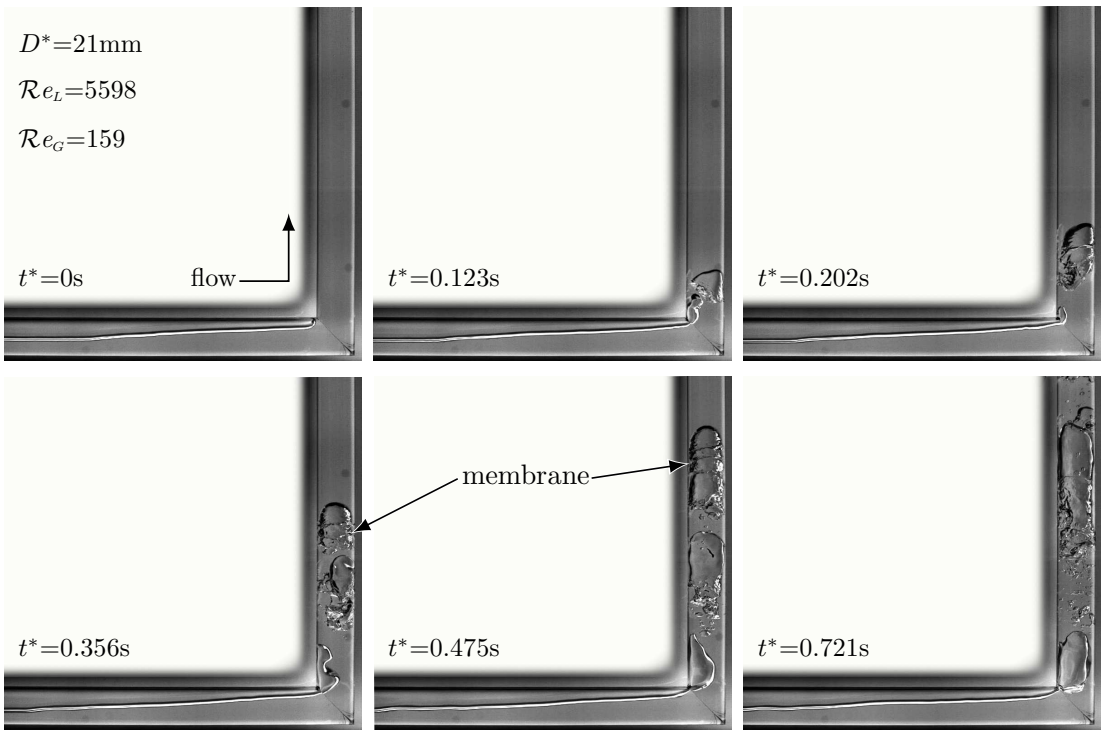

Figure 6.12: Change from plug flow to slug flow due to separation of bubbles across the elbow for D^*=21mm, j_L^*=0.297 m/s, j_G^*=0.15 m/s, $\mathcal{R}e_L$=5598 and $\mathcal{R}e_G$=159.

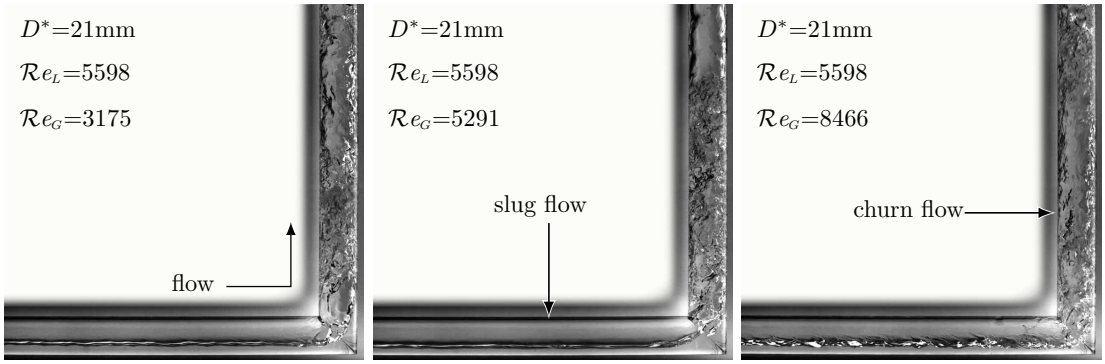

Figure 6.13: Change from slug flow to churn flow through the vertical elbow for D^*=21mm, j_L^*=0.297 m/s, and different j_G^*. Left photo: $\mathcal{R}e_L$=5598 and $\mathcal{R}e_G$=3175. Middle photo: $\mathcal{R}e_L$=5598 and $\mathcal{R}e_G$=5291. Right photo: $\mathcal{R}e_L$=5598 and $\mathcal{R}e_G$=8466.

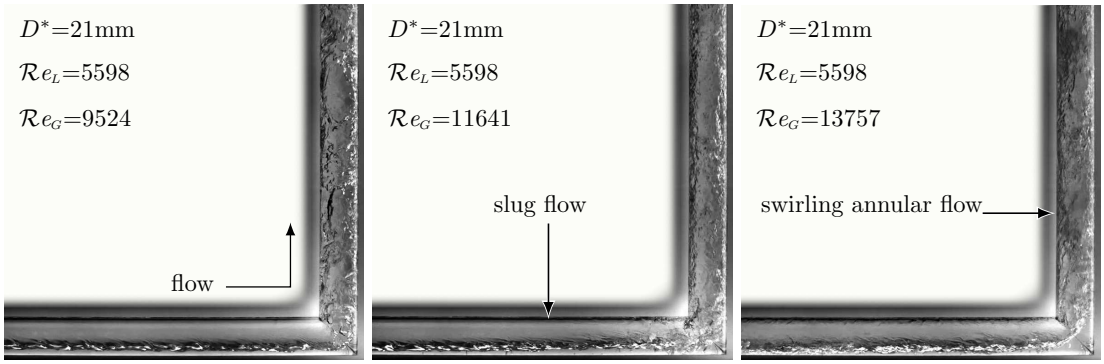

Figure 6.14: Change from slug flow to swirling annular flow through the horizontal to vertical elbow for D^*=21mm, j_L^*=0.297 m/s, and different j_G^*. Left photo: $\mathcal{R}e_L$=5598 and $\mathcal{R}e_G$=9524. Middle photo: $\mathcal{R}e_L$=5598 and $\mathcal{R}e_G$=11641. Right photo: $\mathcal{R}e_L$=5598 and $\mathcal{R}e_G$=13757.

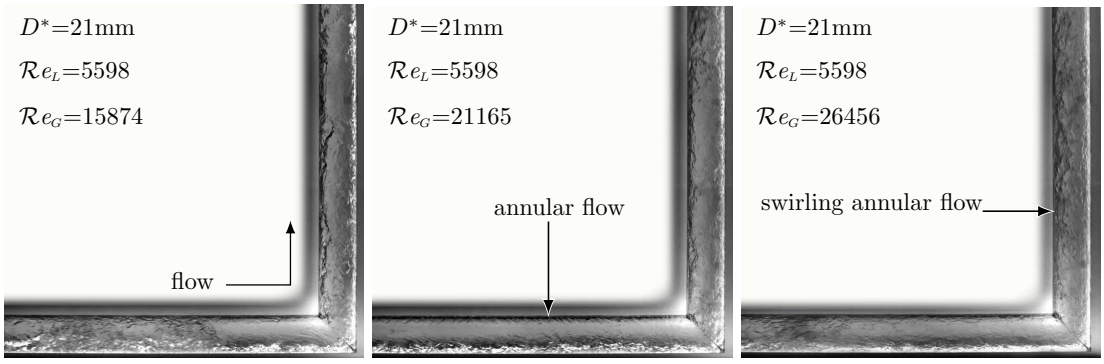

Figure 6.15: Standard annular flow change to swirling annular flow through the horizontal to vertical elbow with upward flow for D^*=21mm, j_L^*=0.297 m/s and different j_G^*. Left photo: $\mathcal{R}e_L$=5598 and $\mathcal{R}e_G$=15874. Middle photo: $\mathcal{R}e_L$=5598 and $\mathcal{R}e_G$=21165. Right photo: $\mathcal{R}e_L$=5598 and $\mathcal{R}e_G$=26456.

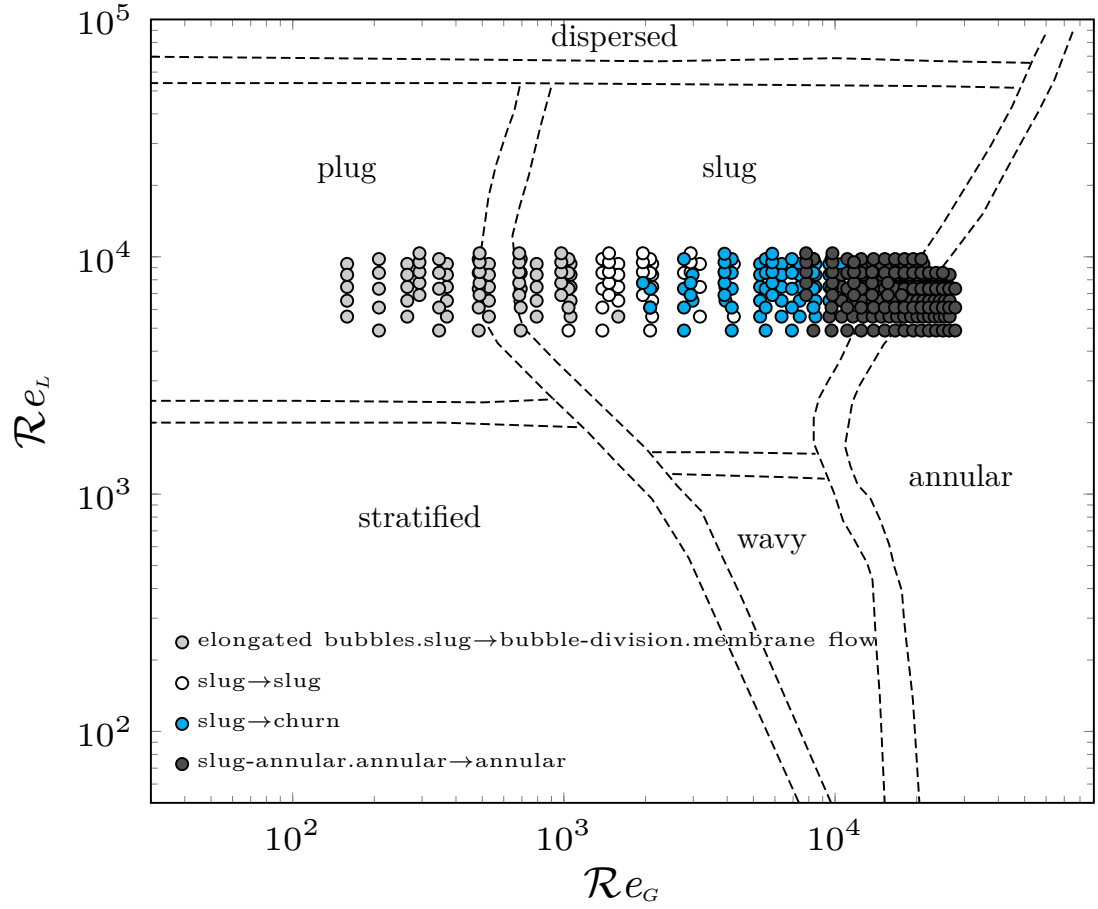

Figure 6.16: Representation of the two-phase flow patterns through the mitre elbows in the horizontal to vertical upward orientation on the non-dimensional Mandhane et al. map [1]. Like in Figure 6.11, the flow regime upstream of the elbow are denoted by the location of the symbols in the Mandhane regions, while the flow regimes downstream of the elbow are indicated by the colour of the symbol.

Chapter 7

Two-phase pressure drop measurements results

This Chapter includes the experimental results and discussions of the pressure drop measurements of air-water flow along straight pipes and across 90° sharp-angled mitre elbows for horizontal and vertical orientations. Section 7.1 reviews the pressure drop in horizontal and vertical straight pipes, while Section 7.2 depicts the pressure drop across 90° sharp-angled mitre elbows. Measurements of peripheral pressure are found in Section 7.3.

Two-phase pressure drop measurements in straight pipes

The pressure drop was first measured along the straight portions of the pipes upstream and downstream of the mitre elbows. The distance upstream of the elbow where the flow starts to be affected by the elbow and the distance downstream of the elbow after which the presence of the elbow is not influential were also measured. The flow recovery length was $60D^*$ downstream of the elbow and the upstream perturbation distance was $32.5D^*$ upstream of the elbow.

Figure 7.1 shows a comparison between our pressure drop data in straight pipes in the horizontal and vertical configurations and the predictions by the models proposed by Lockhart and Martinelli [5], Friedel [86], Chisholm [85] and Müller-Steinhagen and Heck [64]. The data are not predicted well by the models. The

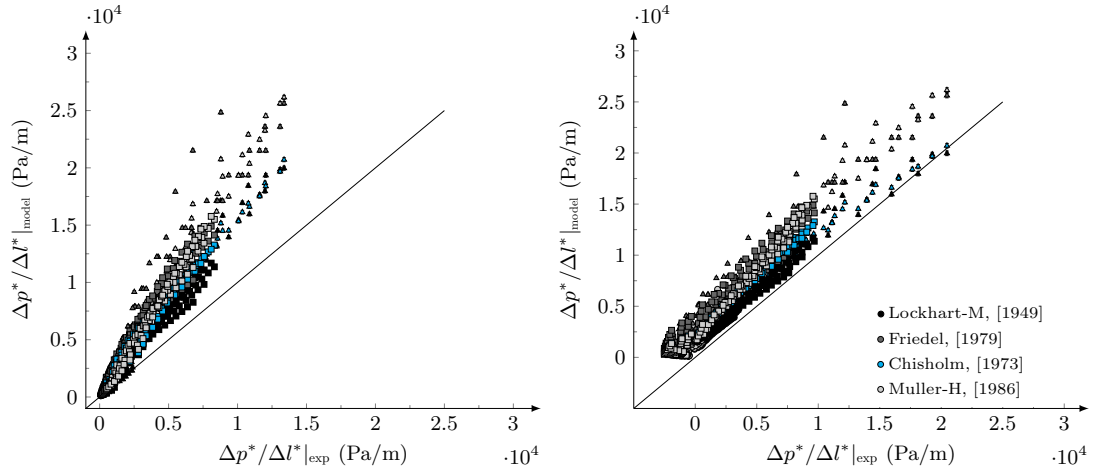

Figure 7.1: Comparison between the experimental pressure drop in horizontal straight pipes (left) and vertical straight pipes (right), with Lockhart and Martinelli [5], Friedel [86], Chisholm [85] and Müller-Steinhagen and Heck [64] models, D^*=11mm △, D^*=16mm □ and D^*=21mm ∘.

deviation between the experimental data and the predicted values increases as the pressure drop increases. The Lockhart and Martinelli [5] model leads to a better agreement with the experimental data than the other two models. At very small pressure drops ($\Delta p^*/\Delta l^*$<2500 Pa/m), the Lockhart and Martinelli [5] and the Müller-Steinhagen and Heck [64] models predict the experimental data with good agreement. At higher pressure drops, the Müller-Steinhagen and Heck [64] model gives a deviation from the experimental data that is much larger than the other two models. The deviation between the models and the experimental data was lower in the vertical case than in the horizontal case. The prediction models do not include the effects of the flow patterns.

Figure 7.2 shows the scaled experimental pressure drop data fitted with the Lockhart and Martinelli Correlation (3.19) [5]. The pressure drop across the whole test section between stations A and J is well expressed by the model with $\mathcal{C}$=10 and $\mathcal{C}$=20. We observe that our data are comprised between the correlation curves for $\mathcal{C}$=10 and $\mathcal{C}$=20.

The scatter is due to the additional factors generated by the elbow, such as severe flow separation and significant perturbation of the flow patterns.

Figure 7.3 shows a comparison between the scaled experimental pressure drop along the test section close to the elbow (between measurement stations C and G) fitted with the Lockhart and Martinelli Correlation (3.19) [5]. The pressure

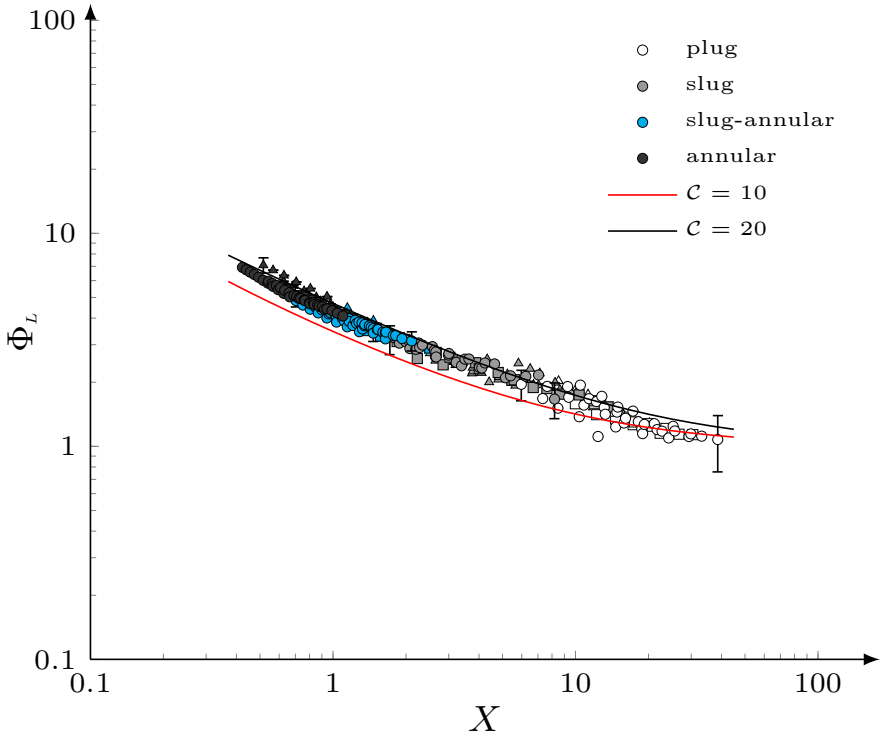

Figure 7.2: Comparison between the experimental two-phase pressure drop along the test section scaled by two-phase multiplier and (3.19) [5], legends are specified in Figure 7.1.

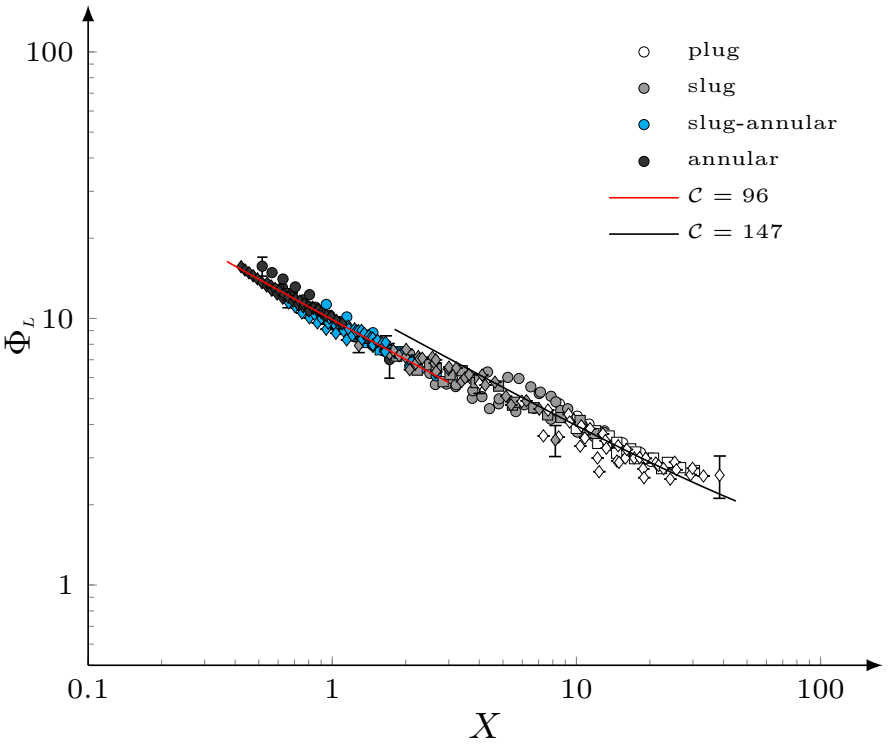

Figure 7.3: Comparison between the experimental pressure drop along the test section close to the elbow scaled by two-phase multiplier and (3.19) [5], legends are specified in Figure 7.1.

drop close to the elbow is higher than across the whole section and it is strongly affected by the flow patterns as depicted in Figure 7.3.

Therefore, we choose to use two $\mathcal{C}$ parameters, one corresponding to the intermittent patterns (slug and plug) and one corresponding to the continuous patterns (slug-annular and annular). The new values are $\mathcal{C}$=147 $\pm$ 9.67% for intermittent patterns and $\mathcal{C}$=96 $\pm$ 3% for continuous patterns. These results show the flexibility of the Lockhart and Martinelli [5] model to fit the two-phase pressure drop with the presence of different types of pipe fittings by employing different values of the parameter $\mathcal{C}$ in Correlation (3.19) as reported by many researchers like Dang et al. [40], Mishima and Hibiki [79], Zhao and Bi [80], Lee and Lee [81], Kim et al. [82], Kong and Kim [83], Qiao et al. [84], Kim et al. [102].

In Appendix C a dimensional analysis based on the Π theorem proves that the scaled frictional pressure drop of an incompressible isothermal air-water flow,

$$\mathcal{C}_{L} = \frac{\Delta p^*}{\Delta l^*} \Bigg|_{\mathrm{f}} \frac{{D^*}^5 \rho_{L}^*}{\dot{m}_{L}^{*2}}, \tag{7.1}$$

can be expressed as a function of only three non-dimensional parameters, i.e. $\mathcal{C}_{L} = \mathcal{C}_{L}(\mathcal{R}e_{L}, \mathcal{R}e_{G}, Fr_{L})$, where $\mathcal{R}e_{L} = \dot{m}_{L}^*/(\mu_{L}^* D^*) = \rho_{L}^* j_{L}^* D^* \pi/(4\mu_{L}^*)$ is the Reynolds number for water, $\mathcal{R}e_{G} = \dot{m}_{G}^*/(\mu_{G}^* D^*) = \rho_{G}^* j_{G}^* D^* \pi/(4\mu_{G}^*)$ is the Reynolds number for air, and $Fr_{L} = \dot{m}_{L}^* / \left(\sqrt{g^*} {D^*}^{5/2} \rho_{L}^*\right)$ is the Froude number for water, where g^* is the gravitational acceleration, and $\dot{m}_{k}^*$, ρ_{k}^*, and μ_{k}^* are the mass flow rates, the densities, and the viscosities of the two fluids, respectively. Only three parameters are required because for incompressible isothermal air-water flows the ratio of densities and the ratio of viscosities are constant.

In Figure 7.4 the two-phase $\mathcal{C}_{L}$ data for the horizontal straight pipe upstream of the elbow in the present work and the data of Spedding and Bénard [61] and Kim et al. [102] show excellent collapse when $\mathcal{C}_{L}\mathcal{R}e_{G}^{\alpha}$ is plotted as a function of $(\mathcal{R}e_{L}/\mathcal{R}e_{G})^{\beta}$. A least-square fit analysis gives α=0.3 and β=0.5. The effect of Froude number is negligible in this range of parameters, as it is expected in the horizontal case. The excellent scaling of the data is independent of the flow patterns, which are represented by different colours in the graph.

Figure 7.5 represents the two-phase $\mathcal{C}_{L}$ data for the vertical straight pipe downstream of the elbow and experimental data from Tang et al. [103]. The collapse

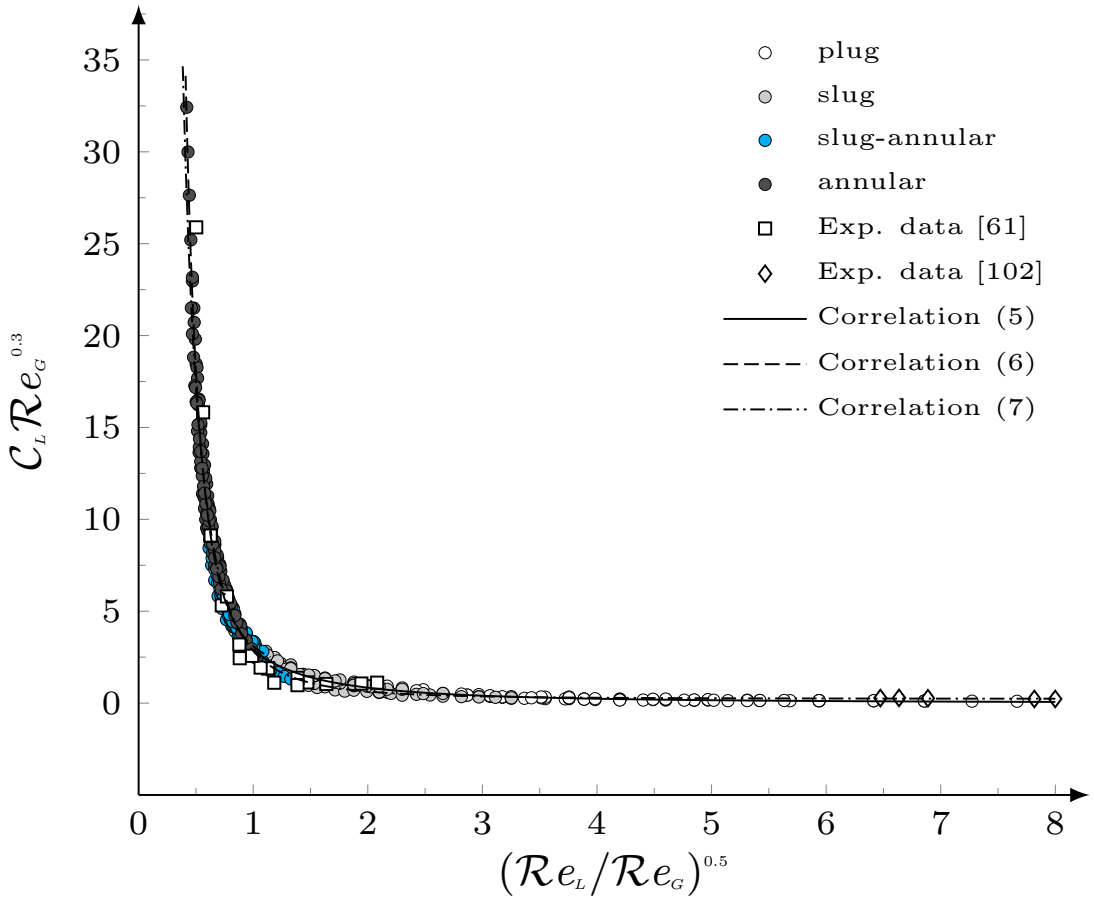

Figure 7.4: Scaled two-phase pressure drop in horizontal pipes.

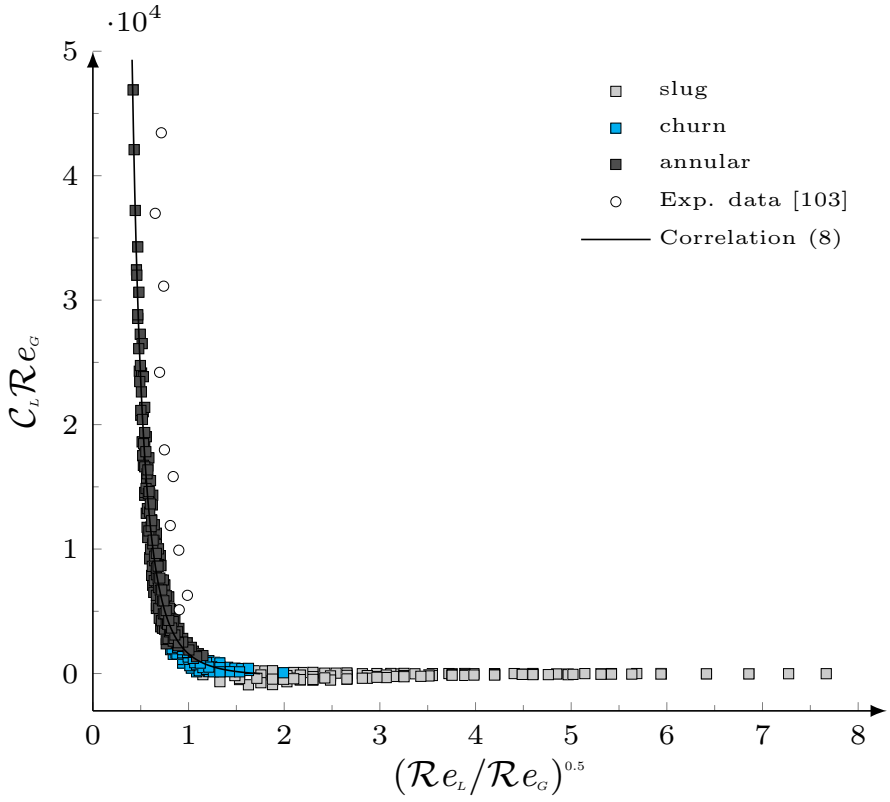

Figure 7.5: Scaled two-phase pressure drop in vertical pipes.

of data scaled in the form $\mathcal{C}_L \mathcal{R}e_G^{\alpha}$ as a function of $(\mathcal{R}e_L/\mathcal{R}e_G)^{\beta}$ (α=1 and β=0.5) is also very good, although the scatter of some data representing the slug and churn flows is larger than in the horizontal configuration because the effect of Fr_L. This is also expected because gravity plays a non-negligible role in the vertical configuration. To clarify the effect of Fr_L the scaled pressure drop data for the vertical pipe case of Figure 7.5 is coloured by Fr_L in Figure 7.6. The effect of Fr_L augments in the range $1<(\mathcal{R}e_L/\mathcal{R}e_G)^{0.5}<4$, causing a scatter in the experimental data in the region between the slug and churn flows. The maximum data scatter occurs for $Fr_L \leq 1$.

Figures 7.5 and 7.6 show that the frictional pressure drop has negative values in the range between slug and churn regimes because the static pressure drop due to gravity overcomes the frictional effect, a phenomenon due to reversed liquid flow at the pipe surface and reported, amongst others, by Spedding's group [61, 104, 105] and by Liu's group [89, 106, 103] in vertical pipe flow. The negative-friction data are highlighted by the hatched area in Figure 7.6. Note that the range of parameters for which the negative friction occurs falls within the range where the effect of Froude number is significant.

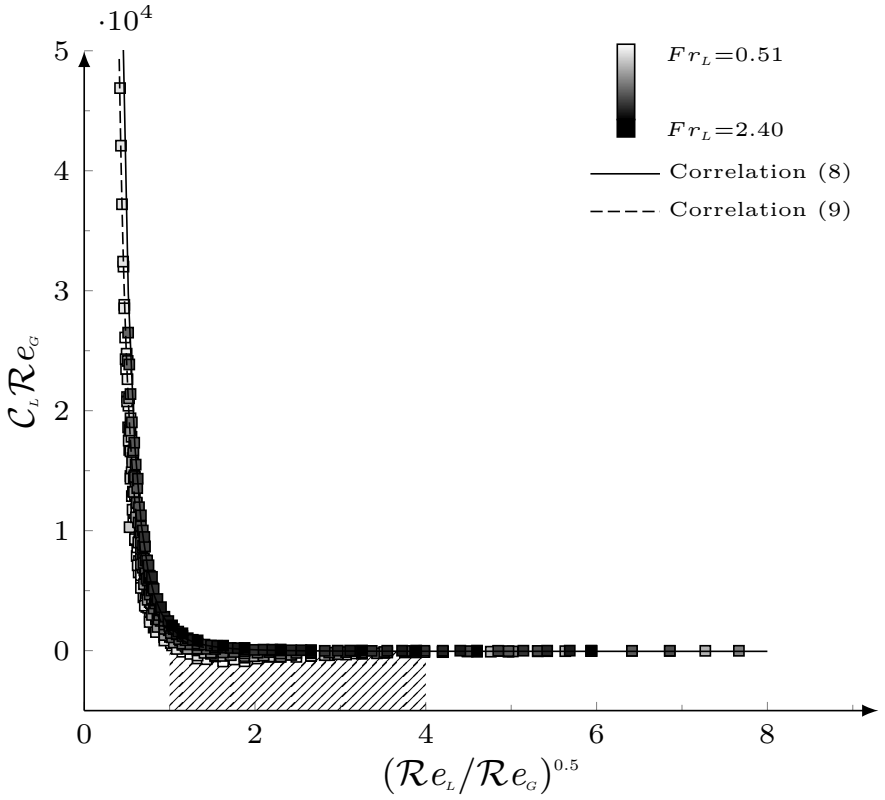

Figure 7.6: Scaled two-phase pressure drop in vertical pipes coloured by Fr_L.

New pattern-based correlations are proposed to fit the experimental data of the frictional pressure drop in horizontal and vertical pipes. The correlations in this section and in Section 7.2 are valid for the same viscosity and density ratios as the ratios between the air and water densities and viscosities and in the ranges of Reynolds numbers stated next to each equation and listed in Tables 4.2 and 4.3.

For the horizontal case the following correlation is proposed for intermittent (plug and slug) flows:

$$\mathcal{C}_L \mathcal{R}e_G^{0.3} = 2.914 \left(\frac{\mathcal{R}e_L}{\mathcal{R}e_G} \right)^{-1.287} - 0.0075, \qquad \left(\frac{\mathcal{R}e_L}{\mathcal{R}e_G} \right)^{0.5} > 1. \tag{7.2}$$

For slug-annular and annular flows in the horizontal case, we propose the following correlation:

$$\mathcal{C}_L \mathcal{R}e_G^{0.3} = 1.54 \left(\frac{\mathcal{R}e_L}{\mathcal{R}e_G} \right)^{-2.923} + 1.554, \qquad \left(\frac{\mathcal{R}e_L}{\mathcal{R}e_G} \right)^{0.5} < 1. \tag{7.3}$$

Correlations (7.2) and (7.3) fit the scaled experimental data with $\pm 12.4\%$ and $\pm 7.8\%$ average error, respectively. The following correlation is proposed to fit the pressure drop data for all flow patterns:

$$\mathcal{C}_L \mathcal{R}e_G^{0.3} = 2.607 \left(\frac{\mathcal{R}e_L}{\mathcal{R}e_G} \right)^{-2.203} + 0.23, \qquad 0.4 < \left(\frac{\mathcal{R}e_L}{\mathcal{R}e_G} \right)^{0.5} < 8. \tag{7.4}$$

Correlation (7.4) fits the experimental data of the present work with ±15% average error and the data of Spedding and Bénard [61] and Kim et al. [102] with ±32% average error.

The frictional pressure drop data for vertical upward churn and annular flows is correlated as follows:

$$\mathcal{C}_{L}\mathcal{R}e_{G} = 1835\left(\frac{\mathcal{R}e_{L}}{\mathcal{R}e_{G}}\right)^{-3.197} - 249.6, \qquad \left(\frac{\mathcal{R}e_{L}}{\mathcal{R}e_{G}}\right)^{0.5} < 1, \tag{7.5}$$

Correlation (7.5) fits 89% of the scaled experimental data of the present work with ±19.3% average error and the data of Tang et al. [103] with ± 42% average error. The high deviation between the experimental data of Tang et al. [103] and Correlation (7.5) is related to the effect of the void fraction, as our calculations were based on Correlation (4.6) to compute the void fraction while the Tang et al.'s are employed direct measurements of the void fraction. Due to the scatter in the pressure drop data for slug flow in vertical pipes, we could not correlate these data with acceptable error for the whole range of Froude numbers. However, we propose a new correlation to fit the experimental data for Fr_{L}>1 as:

$$\mathcal{C}_{L}\mathcal{R}e_{G} = 2111\left(\frac{\mathcal{R}e_{L}}{\mathcal{R}e_{G}}\right)^{-3.506} - 60.77. \qquad \left(\frac{\mathcal{R}e_{L}}{\mathcal{R}e_{G}}\right)^{0.5} > 1. \tag{7.6}$$

The correlation fits 70% of the experimental data for Fr_{L}>1 with ±16.9% average error.

Two-phase pressure drop measurements across the mitre elbows

Pressure gradient distribution along the test sections was measured to study the effect of the elbow and to compute the pressure drop across the 90° sharp-angled mitre elbows.

Figure 7.7 shows the two-phase pressure drop along the test section of D^{*}=21mm and across the mitre elbow in the horizontal configuration. The influence of the elbow is negligible upstream and downstream of the elbow at streamwise distances equal to $32.5D^{*}$ and $60D^{*}$ from the elbow, i.e. at measurement locations C and G, respectively, where the pressure gradient is solely due to the distributed

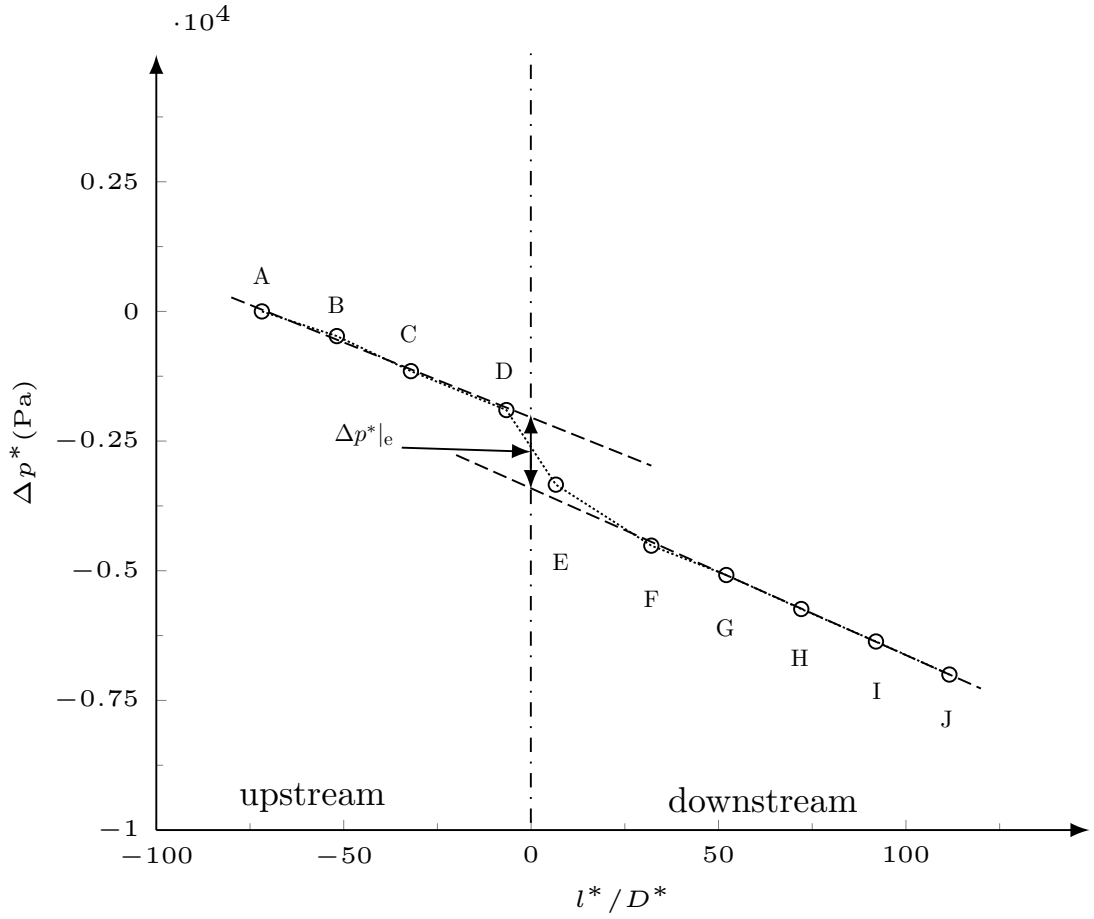

Figure 7.7: Air-water pressure drop relative to the measurement location A along the 21-mm-diameter test section for $\mathcal{R}e_L$ =9330 and $\mathcal{R}e_G$ =8466 in the horizontal configuration.

straight-pipe frictional effects. As graphically represented in Figure 7.7, the pressure drop across the elbow $\Delta p^*|_e$ is computed as the difference between the two best-fit straight lines defining the straight-pipe pressure gradients upstream and downstream of locations C and G, denoted by the dashed lines, and the vertical dash-dotted line at l^*/D^*=0.

Figure 7.8 shows the comparison between our experimental data for the pressure drop through horizontal and horizontal to vertical mitre elbows for a wide range of flow conditions, listed in Tables 4.2 and 4.3, and the prediction given by the models proposed by Chisholm [54] and Sookprasong et al. [87]. These models severely overpredict the pressure drop especially at high flow rates. The deviation increases with the increase of pressure drop for both orientations. This amount of error is expected because these correlations model the frictional pressure drop across round elbows. These models do not include the influence of the flow

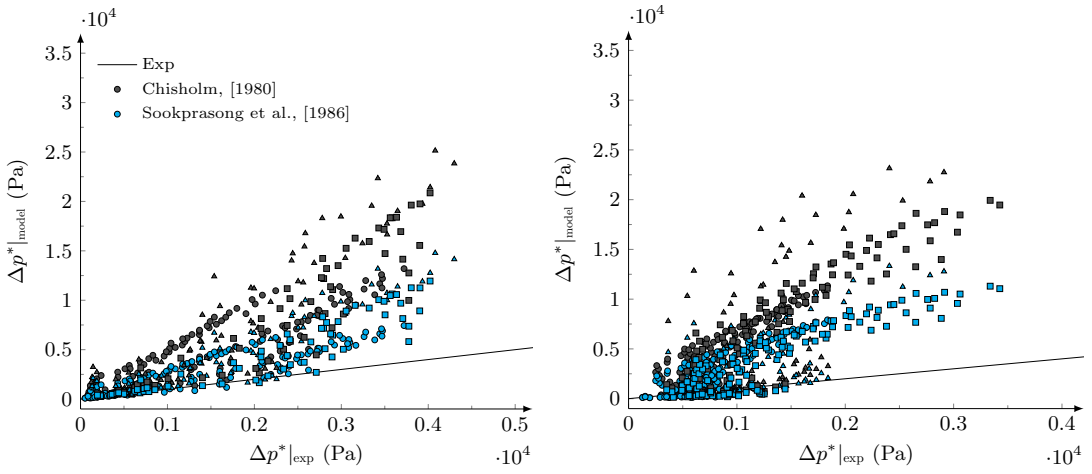

Figure 7.8: Comparison between the experimental pressure drop through horizontal (left) and vertical (right) 90° sharp-angled mitre elbow with Chisholm [54] and Sookprasong et al. [87] models. Legends for the symbols are specified in Figure 7.1.

patterns on the pressure drop [6, 26, 58, 107].

Similar to the $\mathcal{C}_{L}$ coefficient for straight pipes, the dimensional analysis based on the Π theorem outlined in Appendix C proves that the scaled pressure drop of an incompressible isothermal air-water flow across a mitre elbow,

$$\mathcal{K}_{L} = \frac{\Delta p^{*}|_{e} D^{*4} \rho_{L}^{*}}{\dot{m}_{L}^{2}}, \tag{7.7}$$

can be expressed as $\mathcal{K}_{L} = \mathcal{K}_{L}(\mathcal{R}e_{L}, \mathcal{R}e_{G}, Fr_{L})$. Figures 7.9 and 7.10 show the scaled pressure drop $\mathcal{K}_{L}$ for the horizontal and the horizontal to vertical upward configurations, respectively.

Differently from the frictional pressure drop in the straight portions of the pipe, the elbow pressure drop is strongly affected by the flow patterns. The highest data scatter in Figures 7.9 and 7.10 is observed for slug and slug-annular flows, whereas the data for annular and for plug flows instead collapse well, i.e. in the cases of large inertia due to large air flow rates, i.e. large $\mathcal{R}e_{G}$, and to large water flow rates, i.e. large $\mathcal{R}e_{L}$. The effect of Fr_{L} ($0.5 \leq Fr_{L} \leq 2.5$) is mild for the pressure drop due to the mitre elbows. The high scatters for intermittent flows is not due to the effect of the Froude number as in the vertical case but to the separation and secondary flows in elbows, which are more influential than gravity.

New pattern-based correlations are proposed to fit the scaled pressure drop through 90° sharp-angled mitre elbows. For the horizontal case the following correlation

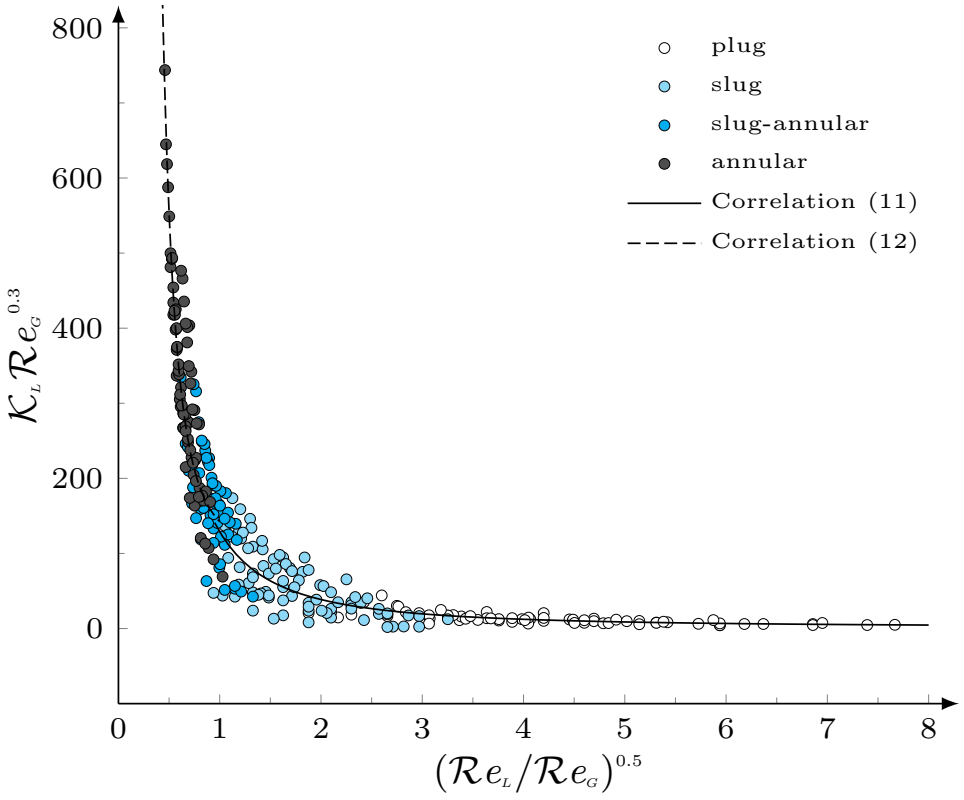

Figure 7.9: Scaled two-phase pressure drop through horizontal 90° sharp-angled mitre elbows.

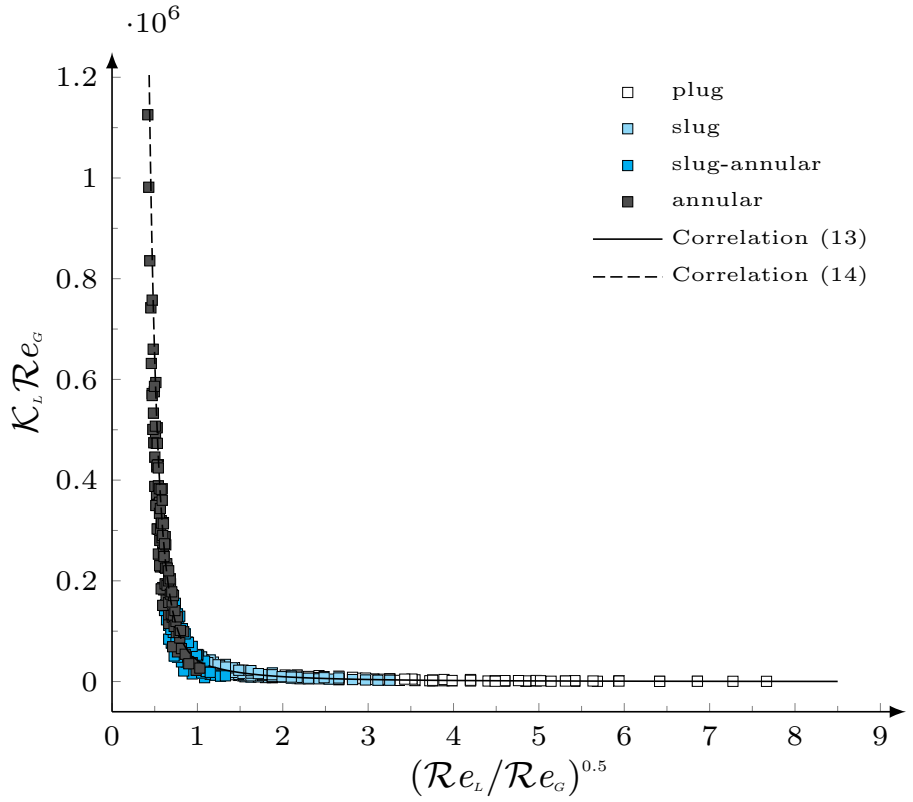

Figure 7.10: Scaled two-phase pressure drop through horizontal to vertical 90° sharp-angled mitre elbows.

is proposed for intermittent (plug and slug) flows:

$$\mathcal{K}_{L}\mathcal{R}e_{G}^{0.3} = 127.3\left(\frac{\mathcal{R}e_{L}}{\mathcal{R}e_{G}}\right)^{-1.276} + 1.472, \qquad \left(\frac{\mathcal{R}e_{L}}{\mathcal{R}e_{G}}\right)^{0.5} > 1. \tag{7.8}$$

For slug-annular and annular flows in the horizontal case, we propose the following correlation:

$$\mathcal{K}_{L}\mathcal{R}e_{G}^{0.3} = 40.25\left(\frac{\mathcal{R}e_{L}}{\mathcal{R}e_{G}}\right)^{-2.991} + 102.1, \qquad \left(\frac{\mathcal{R}e_{L}}{\mathcal{R}e_{G}}\right)^{0.5} < 1. \tag{7.9}$$

Correlation (7.8) fits 83% of the data with ±23.6% average error, while (7.9) fits 90% of the data with ±14.2% average error. Correlation (7.9) also fits the annular flow data only with the same accuracy.

For the horizontal to vertical upward configuration, the following correlation is proposed for intermittent (plug and slug) flows:

$$\mathcal{K}_{L}\mathcal{R}e_{G} = 41370\left(\frac{\mathcal{R}e_{L}}{\mathcal{R}e_{G}}\right)^{-1.549} - 321.2, \qquad \left(\frac{\mathcal{R}e_{L}}{\mathcal{R}e_{G}}\right)^{0.5} > 1. \tag{7.10}$$

For slug-annular and annular flows in the horizontal to vertical upward configuration, the following correlation is proposed:

$$\mathcal{K}_{L}\mathcal{R}e_{G} = 25570\left(\frac{\mathcal{R}e_{L}}{\mathcal{R}e_{G}}\right)^{-4.111} + 16790, \qquad \left(\frac{\mathcal{R}e_{L}}{\mathcal{R}e_{G}}\right)^{0.5} < 1. \tag{7.11}$$

Correlations (7.10) and (7.11) predict the scaled experimental data with 28.6% and 23.9% average error, respectively.

Measurement of two-phase flow peripheral pressure

Figure 7.11 shows two-phase pressure measurements at three angles (0°, 90° and 270°) around the periphery of the 16-mm-diameter pipe at four stations upstream and downstream of the elbow for $\mathcal{R}e_{L}$=8610 and four $\mathcal{R}e_{G}$ in the horizontal configuration. The experimental data show that the peripheral pressure upstream and downstream of the elbow is axially symmetric at all the tested locations. As shown in Figure 4.11, the closest locations D and E are at a distance of $7D^{*}$ upstream and downstream of the elbow, respectively, which agrees with the result by Lima and Thome for the two-phase refrigerant flow through horizontal 180° round elbows [108].

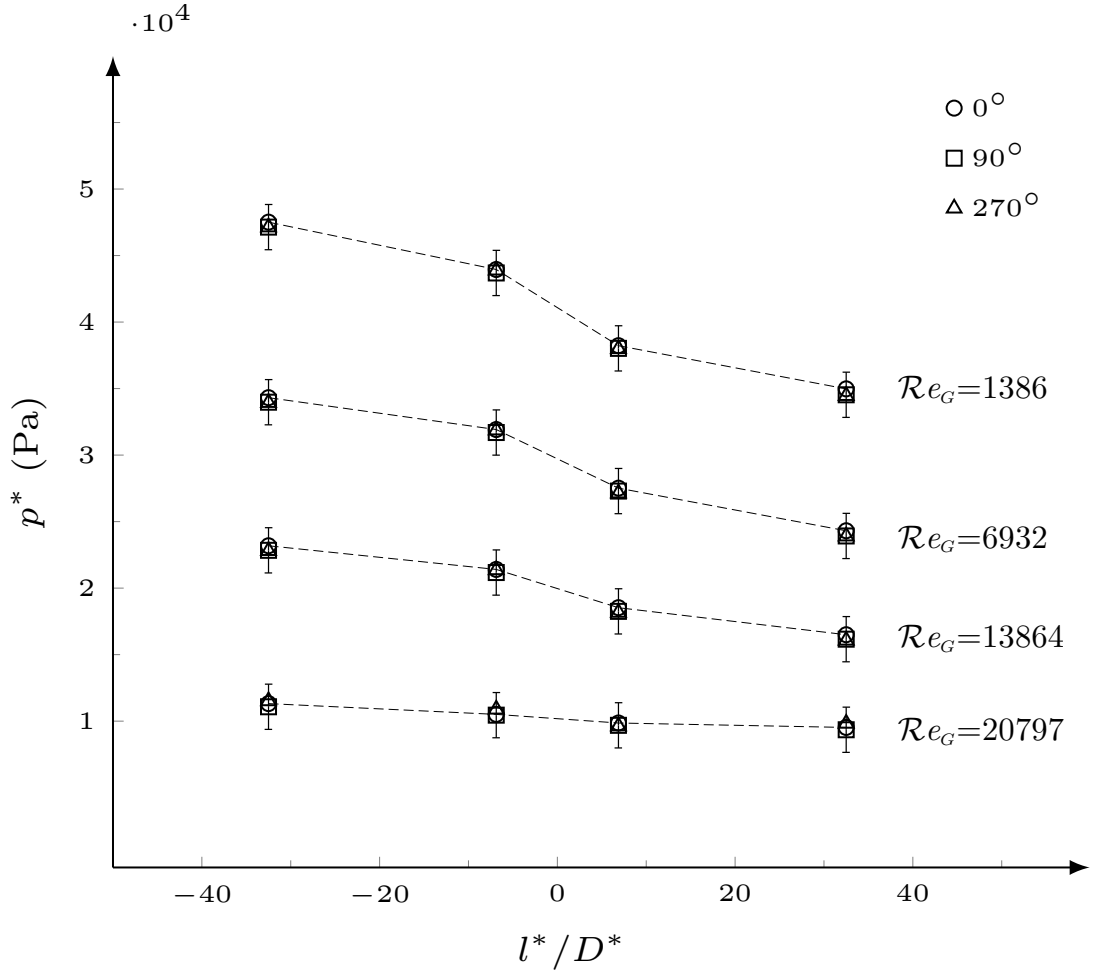

Figure 7.11: Air-water flow pressure drop at different angles around the pipe periphery at stations C, D, E, and F of the 16-mm-diameter test section at $\mathcal{R}e_L$=8556 and different $\mathcal{R}e_G$.

Chapter 8

Conclusions and recommendations

Conclusions

This Section reviews the conclusions of single-phase flow measurements, the two-phase flow visualization and the pressure drop investigations of two-phase flow.

Single-phase flow

The pressure drop in straight pipes and across 90° sharp-angled circular mitre elbows was investigated experimentally for wide ranges of flow conditions to express the pressure loss coefficient $\mathcal{K}$ in terms of Reynolds number $\mathcal{R}e$. The straight-pipe friction factor shows excellent agreement with well-established correlations and reliable published data and it is proved that the pressure was axially symmetric at all the measurement locations. We have shown that the dependence of the pressure-loss coefficient of the 90° mitre elbow on the bulk Reynolds number is rather pronounced, particularly for $\mathcal{R}e$<20000. We have also studied the relationship between this coefficient and the straight-pipe friction factor and obtained two new correlations for the pressure-loss coefficient which will be useful for the design of piping systems fitted with these sharp elbows. The pressure drop was also expressed in terms of the equivalent length to diameter ratio. We have shown that this ratio varies between 35 and 60 and we have presented its dependence on the Reynolds number.

Two-phase flow

This section reviews the conclusions of the prediction results, two-phase flow visualization and pressure drop measurements results.

Prediction results

The prediction results examined the effective factors on two-phase pressure drop in straight pipes and across elbows. The pressure drop increases with the increase of phase velocities, while the pressure drop decreases with the increase of pipe diameter and the bend curvature ratio C for the same flow conditions.

The pressure drop trend was similar in all prediction models which are used in this study even though there is a remarkable deviation between the results of different models.

Two-phase flow visualization

Flow visualization was conducted in this work to identify the flow patterns in straight pipes and to study the behaviour of the two-phase flow patterns through the horizontal and horizontal to vertical 90° sharp-angled mitre elbows. Four flow patterns are observed in horizontal pipes upstream of the elbow: elongated bubbles, slug, slug-annular and annular at 275 different flow conditions, while three flow patterns were observed in the vertical pipe downstream of the elbow: slug, churn and annular at 338 different flow conditions. The observed flow patterns in horizontal and vertical pipes are satisfactory predicted by the Mandhane et al. map [1] and by the Hewitt and Roberts map [2], respectively. The Mandhane et al. [1] map and the Hewitt and Roberts [2] map are successfully rescaled in terms of $\mathcal{R}e_L$ and $\mathcal{R}e_G$ depending on dimensional analysis. The rescaled maps show an improve in the prediction of the flow patterns with mild effect of Fr_L. The membrane flow structure is observed in this study in vertical upward flow as a result of bubbles merge downstream of the elbow at new ranges of j_L^* higher than those were reported by Milan *et al.* [47] in downward flow.

The effects of 90° sharp-angled mitre elbows on the observed flow patterns are expressed in terms of the rescaled Mandhane et al. map [1] for both orientations. The perturbation of the flow regimes due to the elbow lasts about $60D^*$

downstream of the elbow in horizontal and vertical orientations.

Two-phase pressure drop measurements

Pressure drop investigations were conducted to express the air-water pressure drop, in straight pipes and across 90° sharp-angled mitre elbows, in terms of flow patterns and non-dimensional parameters by using Π theory. Pressure drop measured along three different diameters test sections for horizontal and vertical configurations at more than 600 flow conditions.

The comparison between the experimental results and pressure drop prediction models show that the models could not predict the experimental data for all flow conditions. The model of Lockhart and Martinelli [5] fits the scaled pressure drop along the whole test section between $\mathcal{C}$=10 and $\mathcal{C}$=20. The pressure drop along the test section close to the mitre elbow (between measurement stations C and G) is strongly affected by the flow patterns. New pattern-based values of the parameter $\mathcal{C}$ are proposed to fit the scaled pressure drop close to the elbow. The experimental data of straight pipes and 90° sharp-angled mitre elbows in horizontal and vertical orientations are well expressed in terms of non-dimensional parameters and two-phase flow patterns. New empirical correlations are proposed to fit the scaled experimental data of straight pipes and 90° sharp-angled elbows for horizontal and vertical orientations.

The flow perturbation length was located at about $32.5D^*$ upstream of the elbow and $60D^*$ downstream of the elbow. The pressure measurements proved that there is no effect of the elbow on the peripheral pressure farther than $7D^*$ upstream and downstream of the elbow.

Recommendations

This Section includes the recommendations for the future work.

- Investigate the pressure loss coefficient of 90° sharp-angled mitre elbows in single-phase laminar flow for $\mathcal{R}e$<500 and turbulent flow for $\mathcal{R}e$>60000.
- Study the effect of the phase-mixer on the results of two-phase flow visualization and pressure drop measurements by using different types of phase-

mixers.

- Investigate the behaviour of the bubbly, stratified, stratified-wavy and dispersed flows through 90° sharp-angled mitre elbows and examine their effect on the pressure drop across the elbow for horizontal and vertical orientations.

- Study the length, the velocity and the frequency of the elongated bubbles and the phase slugs in these regimes.

- Examine the effect of 90° sharp-angled elbows on two-phase flow patterns and pressure drop for different vertical orientations, like horizontal to vertical with downward flow, vertical to horizontal with upward flow and vertical to horizontal with downward flow.

- Measure the gas-phase void fraction for upward two-phase flow in vertical straight pipes to obtain more accurate calculations of the frictional pressure drop component.

- Investigate the effect of the gas-phase void fraction on the frictional pressure drop of two-phase flow in vertical straight pipes with upward flow.

Bibliography

[1] J. Mandhane, G. Gregory, and K. Aziz, "A flow pattern map for gas-liquid flow in horizontal pipes," *Int. J. Multiph. Flow*, vol. 1, no. 4, pp. 537–553, 1974.

[2] G. Hewitt and D. Roberts, "Studies of two-phase flow patterns by simultaneous 292 X-ray and flash photography," Atomic Energy Research Establishment, Harwell (England), Tech. Rep., 1969.

[3] W. Al-Tameemi and P. Ricco, "Pattern–based pressure drop of air–water flow across a 90° sharp mitre elbow," *Int. J. Comp. Meth. Exp. Meas.*, vol. 6, no. 1, pp. 198–207, 2018.

[4] W. Al-Tameemi and P. Ricco, "Pressure-loss coefficient of 90 deg sharp-angled miter elbows," *ASME J. Fluids Eng.*, vol. 140, no. 6, p. 061102, 2018.

[5] R. Lockhart and R. Martinelli, "Proposed correlation of data for isothermal two-phase, two-component flow in pipes," *Chem. Eng. Prog.*, vol. 45, no. 1, pp. 39–48, 1949.

[6] L. Cheng, G. Ribatski, and J. Thome, "Two-phase flow patterns and flow-pattern maps: fundamentals and applications," *Applied Mech. Rev.*, vol. 61, no. 5, p. 050802, 2008.

[7] W. Dean, "Note on the motion of fluid in a curved pipe," *The London, Edinburgh, and Dublin Phil. Magazine and J. Science*, vol. 4, no. 20, pp. 208–223, 1927.

[8] S. Sugiyama, T. Hayashi, and K. Yamazaki, "Flow Characteristics in the Curved Rectangular Channels: Visualization of Secondary Flow," *Bulletin JSME*, vol. 26, no. 216, pp. 964–969, 1983.

[9] N. Crawford, G. Cunningham, and P. Spedding, "Prediction of pressure drop for turbulent fluid flow in 90 bends," *Proc. Inst. Mech. Eng., Part E: J. Process Mech. Eng.*, vol. 217, no. 3, pp. 153–155, 2003.

[10] N. Crawford, G. Cunningham, and S. Spence, "An experimental investigation into the pressure drop for turbulent flow in 90 elbow bends," *Proc. Ins. Mech. Part E: J. Process. Mech. Eng.*, vol. 221, no. 2, pp. 77–88, 2007.

[11] B. Schmandt and H. Herwig, "A standard method to determine loss coefficients of conduit components based on the second law of thermodynamics," in *ASME Conference Proceedings, Paper No. ICNMM2012-73249*, 2012.

[12] B. Schmandt and H. Herwig, "Loss coefficients for periodically unsteady flows in conduit components: illustrated for laminar flow in a circular duct and a 90 degree bend," *ASME J. Fluids Eng.*, vol. 135, no. 3, p. 031204, 2013.

[13] H. Ito, "Pressure losses in smooth pipe bends," *ASME J. Fluids Eng.*, vol. 82, no. 1, pp. 131–140, 1960.

[14] R. Wilson, W. McAdams, and M. Seltzer, "The flow of fluids through commercial pipe lines," *Ind. Eng. Chem.*, vol. 14, no. 2, pp. 105–119, 1922.

[15] K. Beij, *Pressure Losses for Fluid Flow in 90° Pipe Bends*. National Bureau of Standards, 1938.

[16] J. Perry, "Chemical Engineers' Handbook," *J. Chem. Educ.*, vol. 27, no. 9, p. 533, 1950.

[17] P. Spedding, E. Benard, and G. McNally, "Fluid flow through 90 degree bends," *Develop. Chem. Eng. Mineral Proc.*, vol. 12, no. 1-2, pp. 107–128, 2004.

[18] H. Kirchbach, "Loss of energy in miter bends," *Trans. Munich. Hydraulic Institute, American Soc. Mech. Eng.*, vol. 3, 1935.

[19] W. Schubart, "Energy loss in smooth-and rough-surfaced bends and curves in pipe lines," *Trans. Hydraul. Inst. Munich Tech. Univ*, vol. 3, pp. 81–99, 1935.

[20] N. Haidar, "Prediction of compressible flow pressure losses in 30–150 deg sharp-cornered bends," *ASME J. Fluids Eng.*, vol. 117, no. 4, pp. 589–592, 1995.

[21] S. Moujaes and S. Aekula, "Cfd predictions and experimental comparisons of pressure drop effects of turning vanes in 90 duct elbows," *J. Energy Eng.*, vol. 135, no. 4, pp. 119–126, 2009.

[22] B. Munson, D. Young, and T. Okiishi, "Fundamentals of Fluid Mechanics, John Wiley & Sons," *John Wiley & Sons, Inc.*, 2006.

[23] F. White, "Fluid mechanics. 7th," *Boston: McGraw-Hill Book Company*, 2011.

[24] D. Rennels and H. Hudson, *Pipe Flow: A Practical and Comprehensive Guide*. John Wiley & Sons, 2012.

[25] Crane, *Flow of fluids through valves, fittings, and pipes*. Crane Co., 1988.

[26] C. Brennen, *Fundamentals of multiphase flow*. Cambridge University Press, 2005.

[27] K. Usui, S. Aoki, and A. Inoue, "Flow behavior and pressure drop of two-phase flow through c-shaped bend in vertical plane,(i) upward flow," *J. Nuclear Science and Technology*, vol. 17, no. 12, pp. 875–887, 1980.

[28] K. Usui, S. Aoki, and A. Inoue, "Flow behavior and pressure drop of two-phase flow through c-shaped bend in vertical plane,(ii) downward flow," *J. Nuclear Science and Technology*, vol. 18, no. 3, pp. 179–190, 1981.

[29] K. Usui, S. Aoki, and A. Inoue, "Flow behavior and phase distribution in two-phase flow around inverted u-bend," *J. Nuclear Science and Technology*, vol. 20, no. 11, pp. 915–928, 1983.

[30] T. Takemura, K. Roko, M. Shiraha, and S. Midoriyama, "Dryout characteristics and flow behavior of gas-water two-phase flow through u-shaped and inverted u-shaped bends," *Nuclear Engineering and Design*, vol. 95, pp. 365–373, 1986.

[31] C. Wang, Y. Chen, Y. Yang, and Y. Chang, "Two-phase flow pattern in small diameter tubes with the presence of horizontal return bend," *Int. J. heat and mass transfer*, vol. 46, no. 16, pp. 2975–2981, 2003.

[32] C. Wang, Y. C.I., Y. Yang, and R. Hu, "Influence of horizontal return bend on the two-phase flow pattern in small diameter tubes," *Exp. Therm. Fluid Sc.*, vol. 28, no. 2, pp. 145–152, 2004.

[33] R. Da Silva Lima, "Experimental and visual study on flow patterns and pressure drops in u-tubes," 2011.

[34] M. Padilla, R. Revellin, J. Wallet, and J. Bonjour, "Flow regime visualization and pressure drops of hfo-1234yf, r-134a and r-410a during downward two-phase flow in vertical return bends," *Int. J. Heat Fluid Flow*, vol. 40, pp. 116–134, 2013.

[35] L. Wojtan, T. Ursenbacher, and J. Thome, "Investigation of flow boiling in horizontal tubes: part I. A new diabatic two-phase flow pattern map," *Int. J. Heat and Mass Transfer*, vol. 48, no. 14, pp. 2955–2969, 2005.

[36] P. De Oliveira, E. Strle, and J. Barbosa, "Developing air–water flow downstream of a vertical 180◦ return bend," *Int. J. Multiph. Flow*, vol. 67, pp. 32–41, 2014.

[37] F. Saidj, R. Kibboua, A. Azzi, N. Ababou, and B. Azzopardi, "Experimental investigation of air–water two-phase flow through vertical 90° bend," *Exp. Therm. Fluid Sc.*, vol. 57, pp. 226–234, 2014.

[38] L.-C. Hsu, Y. Chen, C.-M. Chyu, and C.-C. Wang, "Two-phase pressure drops and flow pattern observations in 90° bends subject to upward, downward and horizontal arrangements," *Exp. Therm. Fluid Sci.*, vol. 68, pp. 484–492, 2015.

[39] X. Ma, M. Tian, J. Zhang, L. Tang, and F. Liu, "Flow pattern identification for two-phase flow in a u-bend and its contiguous straight tubes," *Exp. Ther. Fluid Sc.*, 2017.

[40] Z. Dang, Z. Yang, X. Yang, and M. Ishii, "Experimental study of vertical and horizontal two-phase pipe flow through double 90 degree elbows," *Int. J. Heat and Mass Trans.*, vol. 120, pp. 861–869, 2018.

[41] R. Da Silva Lima and J. Thome, "Two-phase flow patterns in u-bends and their contiguous straight tubes for different orientations, tube and bend diameters," *Int. J. Refrig.*, vol. 35, no. 5, pp. 1439–1454, 2012.

[42] J. Luo and X. Wu, "Influence of small imperfections on the stability of plane Poiseui," *Int. J. heat and mass transfer*, vol. 48, no. 112004, pp. 2342–2346, 2005.

[43] C.-C. Wang, Y. Chen, Y.-T. Lin, and Y.-J. Chang, "A visual observation of the air–water two-phase flow in small diameter tubes subject to the influence of vertical return bends," *Chem. Eng. Res. Des.*, vol. 86, no. 11, pp. 1223–1235, 2008.

[44] I. Chen, Chi-Chung, and Y. Yang, "Influence of horizontal return bend on the two-phase flow pattern in a 6.9 mm diameter tube," *The Canadian J. Chemical Eng.*, vol. 80, no. 3, pp. 478–484, 2002.

[45] I. Chen, Y.-S. Wu, Y.-J. Chang, and C.-C. Wang, "Two-phase frictional pressure drop of r-134a and r-410a refrigerant–oil mixtures in straight tubes and u-type wavy tubes," *Exp. Therm. Fluid Sc.*, vol. 31, no. 4, pp. 291–299, 2007.

[46] C. Wang, C. Youn, and H. Shyu, "Frictional performance of R-22 and R-

410a inside a 5.0 mm wavy diameter tube," *Int. J. Heat Mass Transfer*, vol. 46, no. 4, pp. 755–760, 2003.

[47] M. Milan, N. Borhani, and J. Thome, "A new type of flow structure in cocurrent adiabatic vertically downward air–water flow: Membrane flow," *Int. J. Multiph. Flow*, vol. 58, pp. 246–256, 2014.

[48] S. Kim, J. Park, G. Kojasoy, J. Kelly, and S. Marshall, "Geometric effects of 90-degree elbow in the development of interfacial structures in horizontal bubbly flow," *Nuclear Eng. Design*, vol. 237, no. 20, pp. 2105–2113, 2007.

[49] K. De Kerpel, B. Ameel, H. Huisseune, C. Ta Joen, H. Canière, and M. De Paepe, "Two-phase flow behaviour and pressure drop of r134a in a smooth hairpin," *Int. J. Heat and Mass Transfer*, vol. 55, no. 4, pp. 1179–1188, 2012.

[50] P. De Oliveira and J. Barbosa, "Pressure drop and gas holdup in air–water flow in 180 return bends," *Int. J. Multiph. Flow*, vol. 61, pp. 83–93, 2014.

[51] M. Yadav and S. Kim, "Effects of 90° vertical elbows on the distribution of local two-phase flow parameters," *Nuclear Tech.*, vol. 181, no. 1, pp. 94–105, 2013.

[52] M. Yadav, S. Kim, K. Tien, and S. Bajorek, "Experiments on geometric effects of 90-degree vertical-upward elbow in air water two-phase flow," *Int. J. Multiph. Flow*, vol. 65, pp. 98–107, 2014.

[53] E. Graf and S. Neti, "Two-phase flow pressure drop in right angle bends," *ASME J. fluids eng.*, vol. 122, no. 4, pp. 761–768, 2000.

[54] D. Chisholm, "Two-phase flow in bends," *Int. J. Multiph. Flow*, vol. 6, no. 4, pp. 363–367, 1980.

[55] I. Chen, J. Huang, and C. Wang, "Single-phase and two-phase frictional characteristics of small u-type wavy tubes," *Int. Comm. Heat Mass Trans.*, vol. 31, no. 3, pp. 303–314, 2004.

[56] Y. Chen, C.-C. Wang, and S. Lin, "Measurements and correlations of frictional single-phase and two-phase pressure drops of r-410a flow in small u-type return bends," *Int. J. Heat Mass Trans.*, vol. 47, no. 10, pp. 2241–2249, 2004.

[57] S. Benbella, M. Al-Shannag, and Z. Al-Anber, "Gas-liquid pressure drop in vertical internally wavy 90 bend," *Exp. Therm. Fluid Sc.*, vol. 33, no. 2, pp. 340–347, 2009.

[58] F. Sánchez Silva, J. Luna Resendiz, I. Carvajal Mariscal, and R. Tolentino Eslava, "Pressure drop models evaluation for two-phase flow in 90 degree horizontal elbows," *Ingeniería mecánica, tecnología y desarrollo*, vol. 3, no. 4, pp. 115–122, 2010.

[59] M. Padilla, R. Revellin, P. Haberschill, and J. Bonjour, "Two-phase pressure drop in return bends: Experimental results for r-410a," *Int. J. refrigeration*, vol. 34, no. 8, pp. 1854–1865, 2011.

[60] C. Tran, "A study of refrigerant void fraction and pressure drop in return bends and development of a new two-phase experimental apparatus," Air Conditioning and Refrigeration Center. College of Engineering. University of Illinois at Urbana-Champaign., Tech. Rep., 2000.

[61] P. Spedding and E. Bénard, "Gas-liquid two phase flow through a vertical 90 elbow bend," *Exp. Therm. Fluid Sc.*, vol. 31, no. 7, pp. 761–769, 2007.

[62] P. Domanski and C. Hermes, "An improved correlation for two-phase pressure drop of r–22 and r–410a in 180 return bends," *Appl. Ther. Eng.*, vol. 28, no. 7, pp. 793–800, 2008.

[63] D. Geary, "Return bend pressure drop in refrigeration systems," *Ashrae Trans.*, vol. 81, no. 1, pp. 250–264, 1975.

[64] H. Müller-Steinhagen and K. Heck, "A simple friction pressure drop correlation for two-phase flow in pipes," *Chem. Eng. and Proc.: Process Intensification*, vol. 20, no. 6, pp. 297–308, 1986.

[65] I. Chen, Y.-S. Wu, J.-S. Liaw, and C.-C. Wang, "Two-phase frictional pressure drop measurements in u-type wavy tubes subject to horizontal and vertical arrangements," *Appl. Therm. Eng.*, vol. 28, no. 8, pp. 847–855, 2008.

[66] R. C. Bowden and S. Yang, "Experimental investigation of two-phase bubbly flow pressure drop across a horizontal pipe containing 90 bends," *CNL Nuclear Review*, vol. 6, no. 1, pp. 55–69, 2016.

[67] J. Thome, *Engineering data book III*, 2004.

[68] V. Carey, "Liquid-vapor phase-change phenomena," 1992.

[69] G. Hetsroni, "Handbook of multiphase systems," 1982.

[70] J. Collier and J. Thome, *Convective boiling and condensation*. Oxford university press, 1994.

[71] O. Baker, "Simultaneous flow of oil and gas," *Oil and Gas J.*, vol. 53, pp. 185–195, 1954.

[72] Y. Taitel and A. Dukler, "A model for predicting flow regime transitions in horizontal and near horizontal gas-liquid flow," *AIChE J.*, vol. 22, no. 1, pp. 47–55, 1976.

[73] L. Troniewski and R. Ulbrich, "The analysis of flow regime maps of two-phase gas-liquid flow in pipes," *Chemical engineering science*, vol. 39, no. 7, pp. 1213–1224, 1984.

[74] G. E. Alves, "Cocurrent liquid-gas flow in a pipe-line contactor," *Chem. Eng. Progress*, vol. 50, no. 9, pp. 449–456, 1954.

[75] R. Jenkins, "Two-phase two-component flow of air and water," Ph.D. dissertation, MS thesis, University of Delaware, 1947.

[76] O. P. Bergelin and C. Gazley, "Cocurrent gas-liquid flow, i. flow in horizontal tubes," *Heat Transf. and F. Mech. Inst., Berkeley, California*, pp. 5–18, 1949.

[77] H. Blasius, *Das Ähnlichkeitsgesetz bei Reibungsvorgängen in Flüssigkeiten.* Springer, 1913.

[78] D. Chisholm, "A theoretical basis for the Lockhart-Martinelli correlation for two-phase flow," *Int. J. Heat and Mass Transfer*, vol. 10, no. 12, pp. 1767–1778, 1967.

[79] K. Mishima and T. Hibiki, "Some characteristics of air-water two-phase flow in small diameter vertical tubes," *Int. J. Multiphase flow*, vol. 22, no. 4, pp. 703–712, 1996.

[80] T. Zhao and Q. Bi, "Pressure drop characteristics of gas–liquid two-phase flow in vertical miniature triangular channels," *Int. J. of Heat and Mass Transfer*, vol. 44, no. 13, pp. 2523–2534, 2001.

[81] H. Lee and S. Lee, "Pressure drop correlations for two-phase flow within horizontal rectangular channels with small heights," *Int. J. Multiphase Flow*, vol. 27, no. 5, pp. 783–796, 2001.

[82] S. Kim, J. Park, G. Kojasoy, and J. Kelly, "Local interfacial structures in horizontal bubbly flow with 90-degree bend," *Int. Conf. Nuclear Eng.*, vol. 2, pp. 219–226, 2006.

[83] R. Kong and S. Kim, "Characterization of horizontal air–water two-phase flow," *Nuclear Eng. Design*, vol. 312, pp. 266–276, 2017.

[84] S. Qiao, D. Mena, and S. Kim, "Inlet effects on vertical-downward air–water two-phase flow," *Nuclear Eng. Des.*, vol. 312, pp. 375–388, 2017.

[85] D. Chisholm, "Pressure gradients due to friction during the flow of evaporating two-phase mixtures in smooth tubes and channels," *Int. J. Heat and Mass Transfer*, vol. 16, no. 2, pp. 347 – 358, 1973.

[86] L. Friedel, "Improved friction pressure drop correlations for horizontal and vertical two-phase pipe flow," in *European two-phase flow group meeting, Paper E*, vol. 2, 1979, p. 1979.

[87] P. Sookprasong, J. Brill, and Z. Schmidt, "Two-phase flow in piping components," *J. Energy Res. Tech.*, vol. 108, no. 3, pp. 197–201, 1986.

[88] E. Lemmon, M. Huber, and M. McLinden, "NIST Standard Reference Database 23: Reference Fluid Thermodynamic and Transport Properties - REFPROP. 9.0." 2010.

[89] L. Liu, "The phenomenon of negative frictional pressure drop in vertical two-phase flow," *Int. J. Heat Fluid Flow*, vol. 45, pp. 72–80, 2014.

[90] P. Griffith, C. Lau, P. C. Hon, and J. Pearson, "Two phase pressure drop in inclined and vertical pipes," Cambridge: Heat Transf. Lab., 1973, Tech. Rep., 1973.

[91] P. L. Spedding and J. J. J. Chen, "Holdup in two phase flow," *Int. J. Multiph. Flow*, vol. 10, no. 3, pp. 307–339, 1984.

[92] C. J. Baroczy, "A systematic correlation for two-phase pressure drop." in *Chem. Eng. Progr., Symp. Ser., 62: No. 64, 232-49 (1966).* Atomics International, Canoga Park, Calif., 1966.

[93] J. Taylor, *An Introduction to Error Analysis.* University Science Books, 1997.

[94] S. Churchill, "Friction-factor equation spans all fluid-flow regimes," *Chem. Eng.*, vol. 84, no. 24, pp. 91–92, 1977.

[95] S. E. Haaland, "Simple and explicit formulas for the friction factor in turbulent pipe flow," *ASME J. Fluids Eng.*, vol. 105, no. 1, pp. 89–90, 1983.

[96] B. McKeon, C. Swanson, M. V. Zagarola, R. Donnelly, and A. Smits, "Friction factors for smooth pipe flow," *J. Fluid Mech.*, vol. 511, pp. 41–44, 2004.

[97] J. den Toonder and F. M. Nieuwstadt, "Reynolds number effects in a turbulent pipe flow for low to moderate Re," *Phys. Fluids*, vol. 9, no. 11, pp. 3398–3409, 1997.

[98] C. Swanson, B. Julian, G. Ihas, and R. Donnelly, "Pipe flow measurements over a wide range of Reynolds numbers using liquid helium and various gases," *J. Fluid Mech.*, vol. 461, pp. 51–60, 2002.

[99] X. Wu and P. Moin, "A direct numerical simulation study on the mean velocity characteristics in turbulent pipe flow," *J. Fluid Mech.*, vol. 608, pp. 81–112, 2008.

[100] P. Spedding and V. Nguyen, "Regime maps for air water two phase flow," *Chem. Eng. Sc.*, vol. 35, no. 4, pp. 779–793, 1980.

[101] M. Wang and F. Mayinger, "Post-dryout dispersed flow in circular bends," *Int. J. Multiph. Flow*, vol. 21, no. 3, pp. 437–454, 1995.

[102] S. Kim, G. Kojasoy, and T. Guo, "Two-phase minor loss in horizontal bubbly flow with elbows: 45-degree and 90-degree elbows," *Nuclear Eng. Design*, vol. 240, no. 2, pp. 284–289, 2008.

[103] C. Tang, S. Tiwari, and A. J. Ghajar, "Effect of void fraction on pressure drop in upward vertical two-phase gas-liquid pipe flow," *J. Eng. Gas Turb. Power*, vol. 135, no. 2, p. 022901, 2013.

[104] P. Spedding, G. Woods, R. Raghunathan, and W. J.K., "Vertical two-phase flow: Part iii: Pressure drop," *Chem. Eng. Res. Des.*, vol. 76, no. 5, pp. 628–634, 1998.

[105] P. Spedding, G. Woods, R. Raghunathan, and J. Watterson, "Flow pattern, holdup and pressure drop in vertical and near vertical two-and three-phase upflow," *Chem. Eng. Res. Des.*, vol. 78, no. 3, pp. 404–418, 2000.

[106] H. Liu, C. Vandu, and R. Krishna, "Hydrodynamics of taylor flow in vertical capillaries: flow regimes, bubble rise velocity, liquid slug length, and pressure drop," *Indust. & Eng. Chem. Res.*, vol. 44, no. 14, pp. 4884–4897, 2005.

[107] S. Z. Rouhani and M. S. Sohal, "Two–phase flow patterns: A review of research results," *Prog. in Nuc. Ener.*, vol. 11, no. 3, pp. 219–259, 1983.

[108] R. Lima and J. Thome, "Two–phase pressure drops in adiabatic horizontal circular smooth u-bends and contiguous straight pipes (rp-1444)," *Hvac&R Research*, vol. 16, no. 3, pp. 383–397, 2010.

[109] C. Colebrook, "Turbulent flow in pipes, with particular reference to the transition region between the smooth and rough pipe laws." *J. ICE*, vol. 11, no. 4, pp. 133–156, 1939.

[110] X. Fang, Y. Xu, and Z. Zhou, "New correlations of single-phase friction factor for turbulent pipe flow and evaluation of existing single-phase friction factor correlations," *Nuclear Engineering and Design*, vol. 241, no. 3, pp. 897–902, 2011.

[111] P. Sookprasong, *Two-phase flow in piping components*. University of Tulsa, Fluid Flow Projects, 1980.

Appendices

Appendix A

Prediction results

This Appendix reviews the prediction results of single-phase Darcy friction factor in straight pipes, the pressure loss coefficient of 90° round elbows, two-phase pressure drop in straight pipes and across 90° round elbows. Many prediction models were employed to obtain these results for different flow conditions and pipes diameters which are listed in Table A.1.

Table A.1: Flow conditions and pipes specifications that were employed in the prediction calculations.

Pipe diameter D^* (mm)	11	16	21
Ambient pressure (bar)	1	1	1
Temperature °C	25	25	25
j_L^* (m/s)	0.68 - 1.015	0.34 - 0.68	0.297 - 0.495
j_G^* (m/s)	0.51 - 26	0.25 - 26	0.1485 - 26
Pipe surface roughness	smooth	smooth	smooth

Lemmon et al. [88] was used to evaluate the physical properties of air and water at the given ambient pressure and temperature. The prediction analysis waswas conducted to examine the effective factors on two-phase pressure drop in straight pipes and across 90° elbows, like the superficial velocities and pipes diameters.

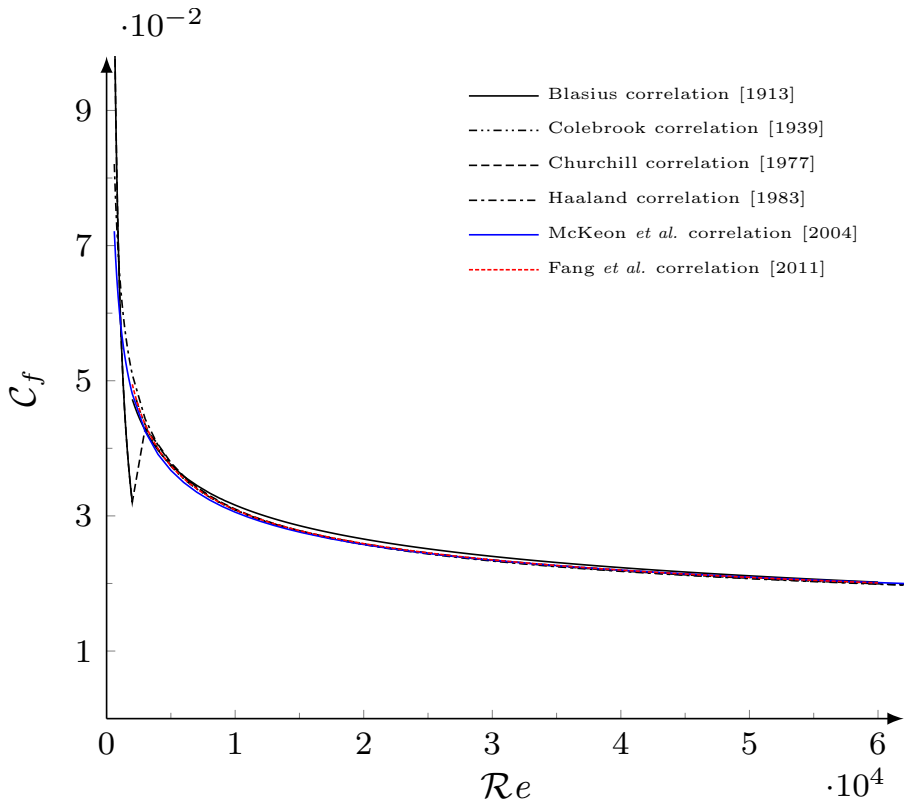

Figure A.1: Prediction values of single-phase friction factor of pipe flow by using Blasius, Colebrook, Churchill, Haaland, McKeon et al. and Fang et al. formulas for different conditions as listed in Table A.1.

Single-phase Darcy friction factor and pressure loss coefficient

The prediction of single-phase pressure drop across the elbow is crucial because most of the two-phase pressure drop prediction models are employing the single-phase pressure drop and a two-phase multiplier.

Numerous implicit and explicit formulas have been proposed to express the single-phase Darcy friction factor in terms of Reynolds number $\mathcal{R}e$ by Blasius [77], Colebrook [109], Churchill [94], Haaland [95], McKeon et al. [96] and Fang et al. [110]. Figure A.1 shows the single-phase friction factor which is computed by using different correlations for $\mathcal{R}e$<60000. Although there is some deviation between the predicted values of $\mathcal{C}_f$ which are computed by different formulas, any one of these formulas can be employed to evaluate the single-phase friction factor $\mathcal{C}_f$ with acceptable percentage of error.

In addition to the frictional losses in straight pipe flow, the flow across pipe

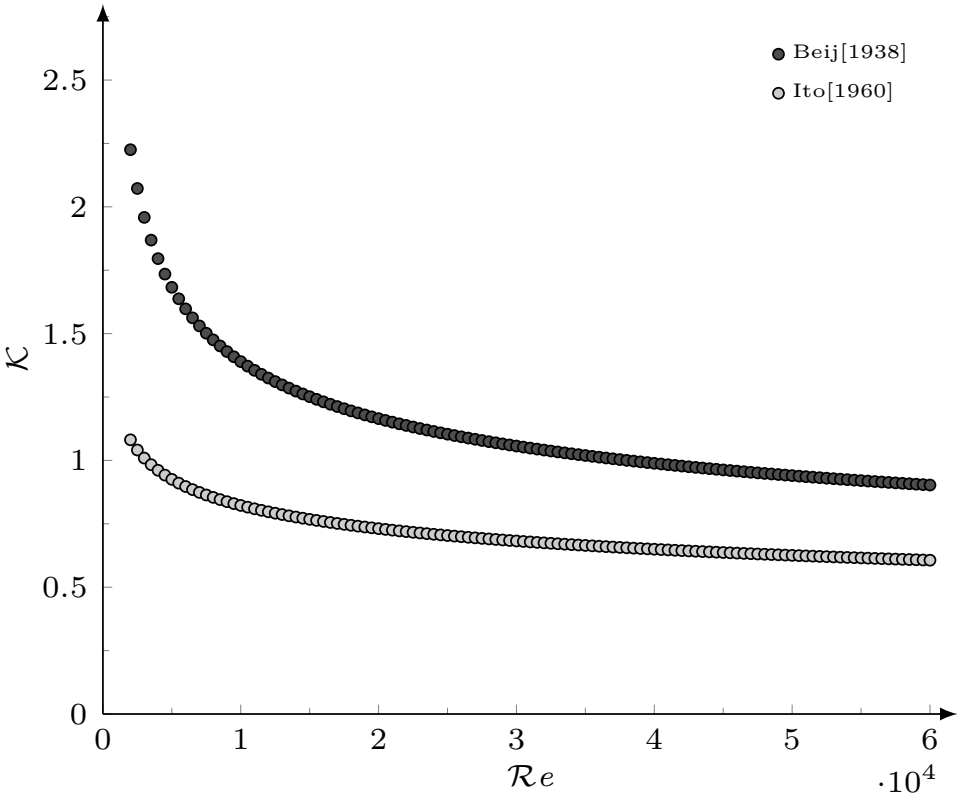

Figure A.2: Predicted values of single-phase pressure loss coefficient $\mathcal{K}$ of 90° round elbows with $C = 1$ in terms of $\mathcal{R}e$ by using Beij [15] and Ito [13] methods.

bends and elbows includes further losses as a consequence of the secondary flow and the flow separation. Two well known methods were proposed by Beij [15] and Ito [13] to express the pressure drop across elbows and pipe bends in terms of equivalent length to diameter ratio $\mathcal{L}$ and pressure loss coefficient $\mathcal{K}$ respectively. Figure A.2 shows a single-phase pressure loss coefficient of 90° round bends $\mathcal{K}$ in terms of $\mathcal{R}e$ by using Beij [15]'s and Ito [13]'s approaches. There is a remarkable deviation between the predicted values of $\mathcal{K}$ by the models and this deviation could be related to the difference in the assumptions that were used to propose the models.

Two-phase pressure drop

This section includes the prediction values of air-water frictional pressure drop in straight pipes and across 90° round elbows by using many well known prediction models.

Two-phase pressure drop in straight pipes

Three prediction models of two-phase pressure drop, Lockhart and Martinelli [5], Friedel [86], Chisholm [85], Müller-Steinhagen and Heck [64], were used to examine the effect of the phase velocities and the pipe diameter on the frictional pressure drop of air-water flow for the flow conditions which are listed in Table A.1.

Effect of air and water superficial velocities

Figure A.3 illustrates the predicted pressure drop per unit length $\Delta p^*_{tp}/\Delta l^*$ for different j^*_L and j^*_G by using Lockhart and Martinelli [5], Friedel [86], Chisholm [85] and Müller-Steinhagen and Heck [64] models. The prediction results show that the pressure drop in straight pipes $\Delta p^*_{tp}/\Delta l^*$ increases as the air and water superficial velocities increase as mentioned by many studies which were reviewed in Chapter 3. Although the predicted values of pressure drop by different models follow the same trend, a remarkable deviation between the values of different models can be noticed as illustrated in Figure A.4.

Effect of pipe diameter

Pipe diameter D^* represents an effective factor on two-phase frictional pressure drop. Figure A.5 show the predicted values of pressure drop per unit length $\Delta p^*_{tp}/\Delta l^*$ in therms of j^*_G and D^* for j^*_L= 0.396 m/s by using Lockhart and Martinelli [5], Friedel [86], Chisholm [85] and Müller-Steinhagen and Heck [64] models. The predicted pressure drop per unit length $\Delta p^*_{tp}/\Delta l^*$ increases as D^* decreases for same flow conditions as mentioned by many studies in the literature as clarified in Chapter 3.

Pressure drop across 90° round elbows

The effect of superficial velocities of the working fluids and pipes inside diameters on air-water pressure drop across 90° round elbows are presented in this section.

Effect of superficial velocities

Figure A.6 shows the predicted values of air-water pressure drop across 90° round elbows $\Delta p^*_{tp,e}$ by using Chisholm [54] and Sookprasong [111] models in terms of air

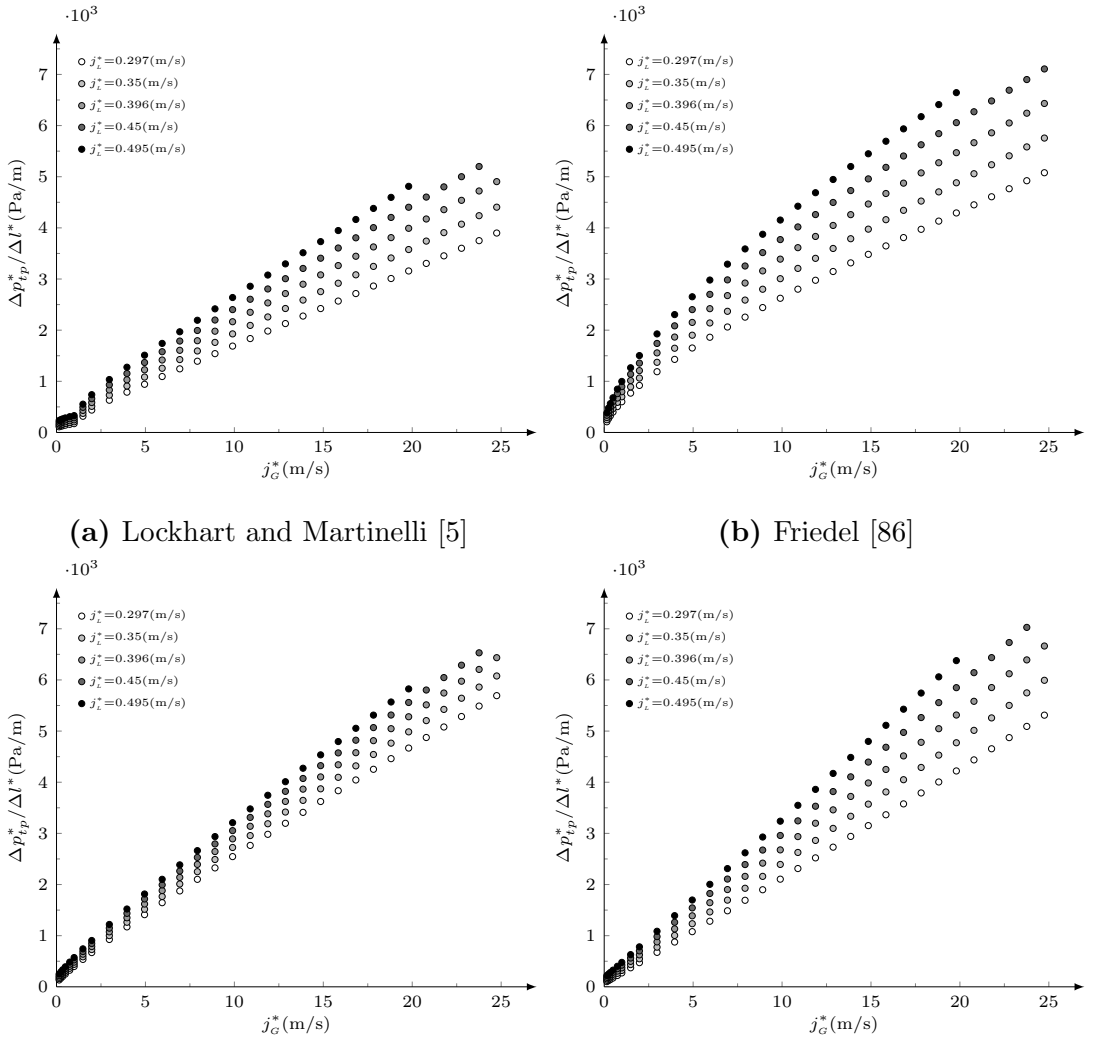

(a) Lockhart and Martinelli [5]

(b) Friedel [86]

(c) Chisholm [85]

(d) Müller-Steinhagen and Heck [64]

Figure A.3: Air-water two-phase frictional pressure drop per unit length $\Delta p_{tp}^*/\Delta l^*$ predictions in terms of j_G^* for T^*=25°C, D^*=21mm and p^*=1 bar and different j_L^*.

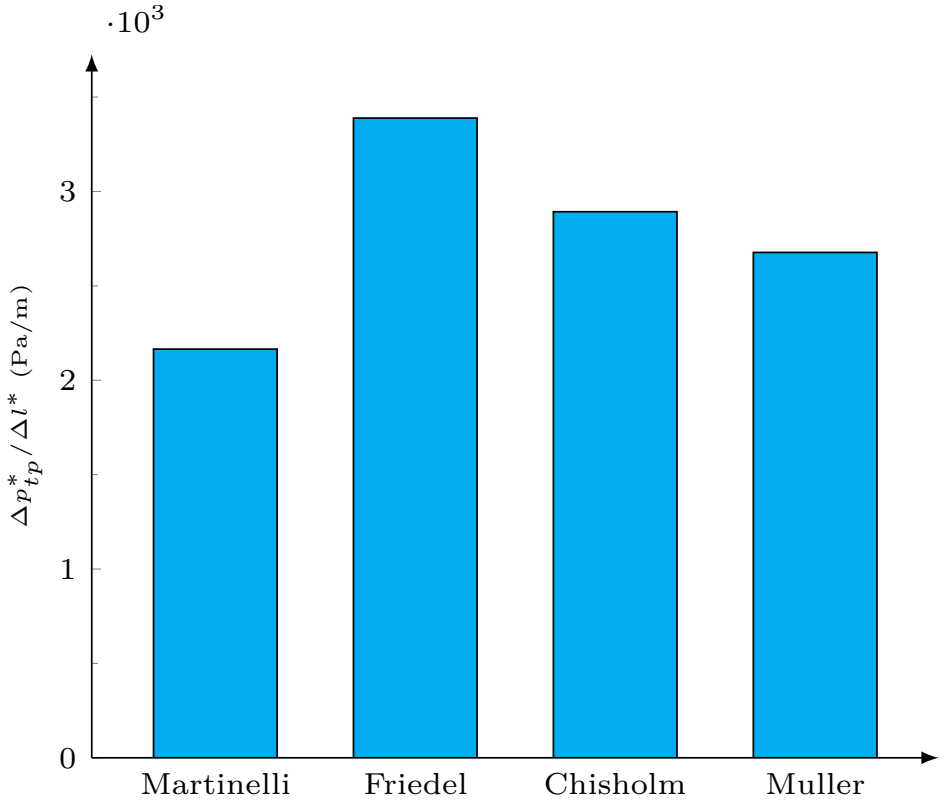

Figure A.4: Comparison between the predicted pressure drop in straight pipes by using Lockhart and Martinelli [5], Chisholm [85], Müller-Steinhagen and Heck [64] for D^*=21mm, j^*_L=0.396 m/s and j^*_G=9.9 m/s.

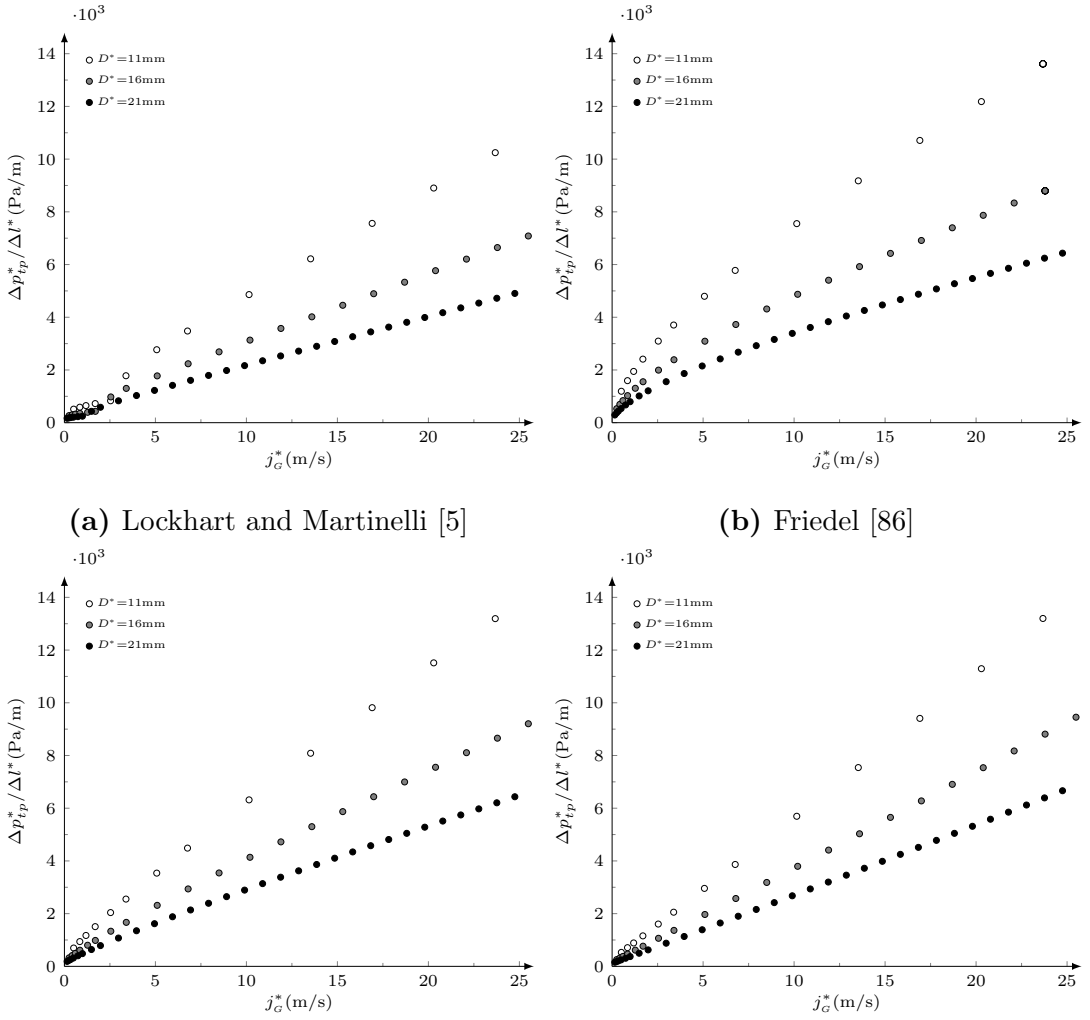

(a) Lockhart and Martinelli [5]

(b) Friedel [86]

(c) Chisholm [85]

(d) Müller-Steinhagen and Heck [64]

Figure A.5: Air-water two-phase frictional pressure drop per unit length $\Delta p^*_{tp}/\Delta l^*$ predictions in terms of j^*_G for T^*=25°C, p^*=1 bar, j^*_L 0.396 m/s and different D^*.

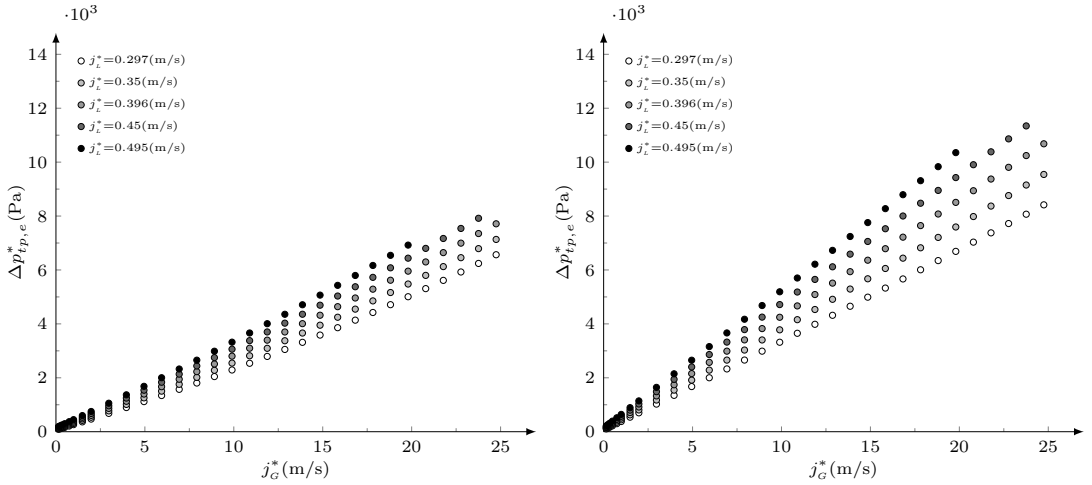

(a) Sookprasong [111] **(b)** Chisholm [54]

Figure A.6: Predicted values of air-water pressure drop across 90° round elbows by using Chisholm [54], Sookprasong [111] models for T^*=25°C, D^*=21mm and p^*=1 bar.

and water superficial velocities for D^*=21mm. The prediction results show that the pressure drop increases as the superficial velocities increase for both models. Although the models predict different values of pressure drop for the same flow conditions as clarified in Figure A.7, the pressure drop results follow the same trend.

Effect of pipe diameter:

Figure A.8 shows the predicted pressure drop across 90° round elbows by using Chisholm [54] and Sookprasong [111] models in terms of j_G^* for different D^* at j_L^*=0.396 m/s. The predicted results show mild effect of the pipe diameter D^* on the pressure drop across 90° elbows. These results agree with many studies, in the literature, which are reported that the pressure drop across the elbows is a function of the elbow curvature ratio C rather than the pipe diameter D^*.

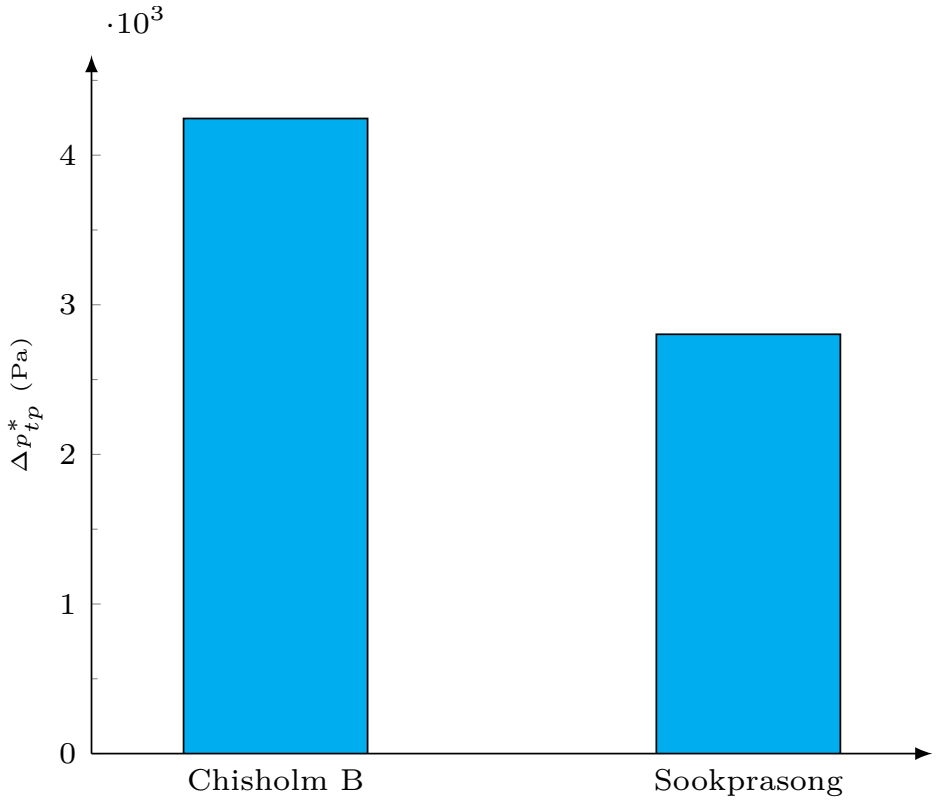

Figure A.7: Predicted two-phase pressure drop across 90° round elbows by using Chisholm [54] and Sookprasong [111] models for D^*=21mm, j_L^*=0.396 m/s and j_G^*=9.9 m/s.

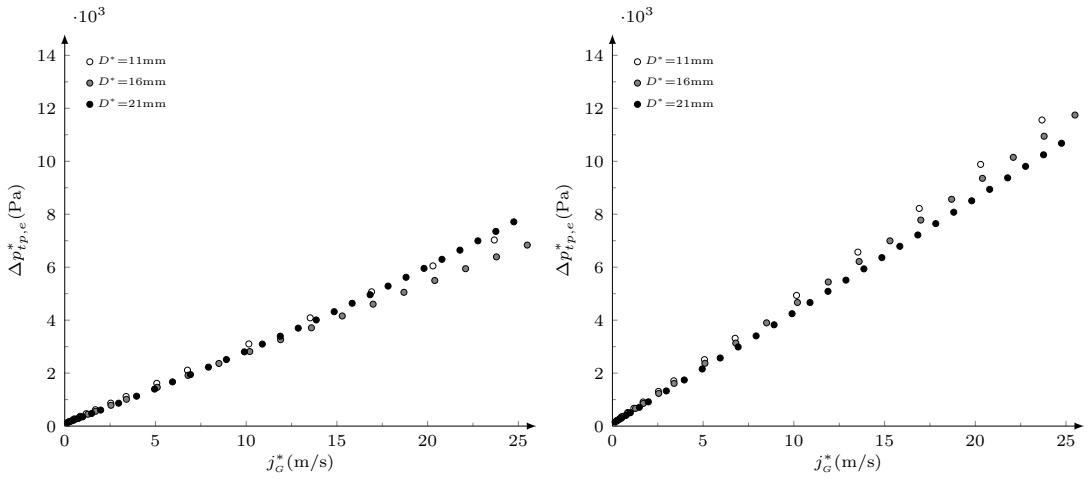

(a) Sookprasong [111] **(b)** Chisholm [54]

Figure A.8: Predicted values of air-water pressure drop across 90° round elbows by using Chisholm [54] and Sookprasong [111] models for T^*=25°C, p^*=1 bar and j_L^*=0.396 m/s.

Appendix B

Calibration of measurement instruments

All of the measurement instruments were calibrated either by the manufacturer or in the lab against accurate standards. The calibration of the instruments has been included in the calculations of the experimental data. This Appendix presents the details of the measurement instruments calibration certificates and data.

Pressure measurements instruments

Differential pressure Instruments

A differential pressure transducer was employed to measure the high-range (0-17.23kPa) pressure drop of single-phase water and two-phase flows along the test sections. Figures B.1 and B.2 depict the calibration certificate and data of the differential pressure transducer respectively. A differential pressure transmitter was used to measure the low-range of pressure drop (0-2.5 kPa) of single-phase water and two-phase flows. The calibration certificate and data of the differential pressure transmitter are shown in Figures B.3 and B.4 respectively.

Absolute pressure

An absolute pressure transducer was used in this work to measure the absolute pressure. The transducer was calibrated by the manufacturer and supplied with

O M E G A E N G I N E E R I N G I N C.

PRESSURE TRANSDUCER
FINAL CALIBRATION

0.00 - 2.50 PSID
Excitation 24.000 Vdc

Job: WHS0004391 Serial: 454777
Model: PX409-2.5DWU10V Tested By: KSM
Date: 10/31/2015 Temperature Range: 0 to 185 F
Calibrated: 0.00 - 2.50 PSID Specfile: PX409V10>1G

Pressure PSID	Unit Data Vdc
0.00	0.006
1.25	5.001
2.50	10.002
1.25	5.002
0.00	0.005

Balance 0.006 Vdc
Sensitivity 9.996 Vdc

ELECTRICAL LEAKAGE: PASS
PRESSURE CONNECTION/FITTING: 1/4-18 NPT Male
ELECTRICAL WIRING/CONNECTOR: Integral Cable 4-Cond
BLACK = - EXCITATION
WHITE = + OUTPUT
GREEN = N/C
RED = + EXCITATION

This Calibration was performed using Instruments and Standards that are traceable to the United States National Institute of Standards Technology.

S/N	Description	Range	Reference	Cal Cert
801	PPC3 30 PSI AUTO	0 - 2.50 PSID	C-1952	C-1952
US37026070	HP 34970A	Unit Under Test	C-2492	C-2492

Q.A. Representative : Kapeme Manyuanh Date: 10/31/2015

This transducer is tested to & meets published specifications. After final calibration our products are stored in a controlled stock room & considered in bonded storage. Depending on environment & severity of use factory calibration is recommended every one to three years after initial service installation date.

Omega Engineering Inc., One Omega Drive, Stamford, CT 06907
http://www.omega.com email: info@omega.com phone (800) 826-6342

Figure B.1: Calibration certificate of the differential pressure transducer.

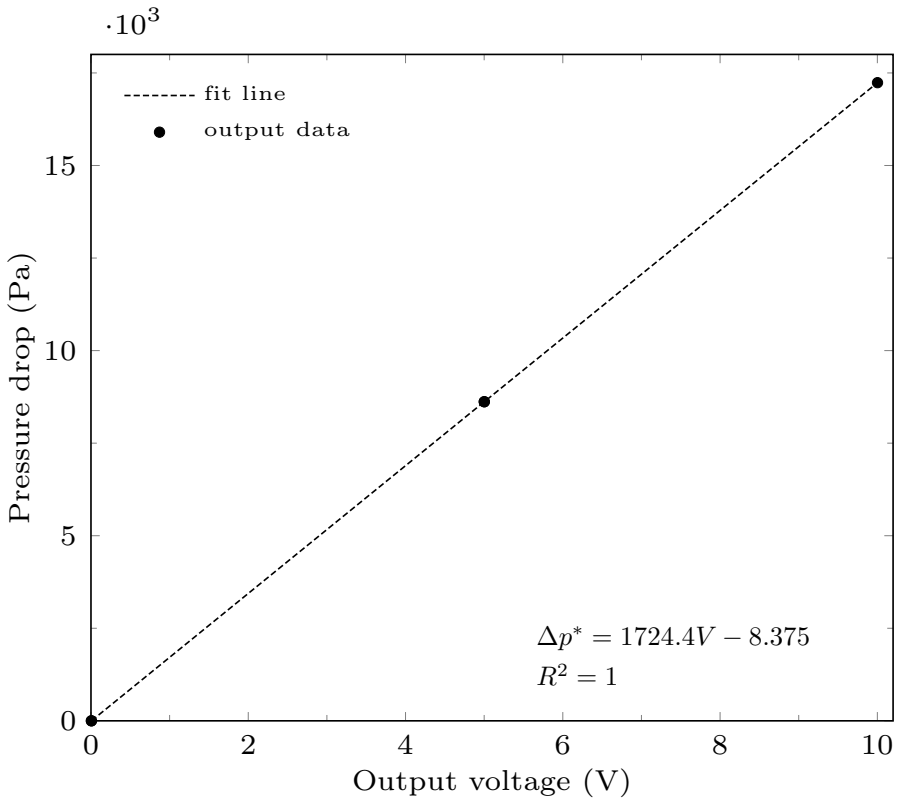

Figure B.2: Calibration data of the differential pressure transducer, range 0 - 17.23kPa.

a signed certificate. Figures B.5 and B.6 depict the calibration certificate and data of the absolute pressure transducer respectively.

Flow measurements

Water flow measurements

Two different turbine flow meters (FTB-101 and FTB-104) with six digits rateme-ter (Omega DPF-702) were employed for water flow measurements in the ranges of (1.3-13.2 and 6.6-60) LPM, respectively. The flow meters were calibrated by the manufacturer with $\pm 0.5\%$ reading error and the calibration certificates and data for the water flow meters are shown in Figures B.7, B.8, B.9 and B.10.

Air flow measurement

An air mass flow meter was used to measure the air flow rate. The flow meter was calibrated by the manufacturer and supplied with a signed certificate. The calibration certificate and data are illustrated in Figures B.11 and B.12 respectively.

O M E G A E N G I N E E R I N G I N C.

PRESSURE TRANSDUCER
FINAL CALIBRATION

0.00 - 10.00 in H2O D
Excitation 24.000 Vdc

Job: R11116 Serial: 449898
Model: PX409-10WDWUI Tested By: SS
Date: 3/14/2016 Temperature Range: -17 to +85 C
Calibrated: 0.00 - 10.00 in H2O D Specfile: PX409I<=1G

Pressure in H2O D	Unit Data mA
0.00	4.021
5.00	12.021
10.00	20.027
5.00	12.016
0.00	4.022

Balance 4.021 mA
Sensitivity 16.006 mA

ELECTRICAL LEAKAGE: PASS
PRESSURE CONNECTION/FITTING: 1/4-18 NPT Male
ELECTRICAL WIRING/CONNECTOR: Integral Cable 4-Cond
BLACK = - SUPPLY
WHITE = N/C
GREEN = N/C
RED = + SUPPLY

This Calibration was performed using Instruments and Standards that are traceable to the United States National Institute of Standards Technology.

S/N	Description	Range	Reference	Cal Cert
801	PPC3 2.2 PSIG AUTO	0 - 10.00 in H2O	DC-1952	C-1952
US37026070	HP 34970A	Unit Under Test	C-2492	C-2492

Q.A. Representative : Irene Chavez Date: 3/14/2016

This transducer is tested to & meets published specifications. After final calibration our products are stored in a controlled stock room & considered in bonded storage. Depending on environment & severity of use factory calibration is recommended every one to three years after initial service installation date.

Omega Engineering Inc., One Omega Drive, Stamford, CT 06907
http://www.omega.com email: info@omega.com phone (800) 826-6342

Figure B.3: Calibration certificate of the differential pressure transmitter.

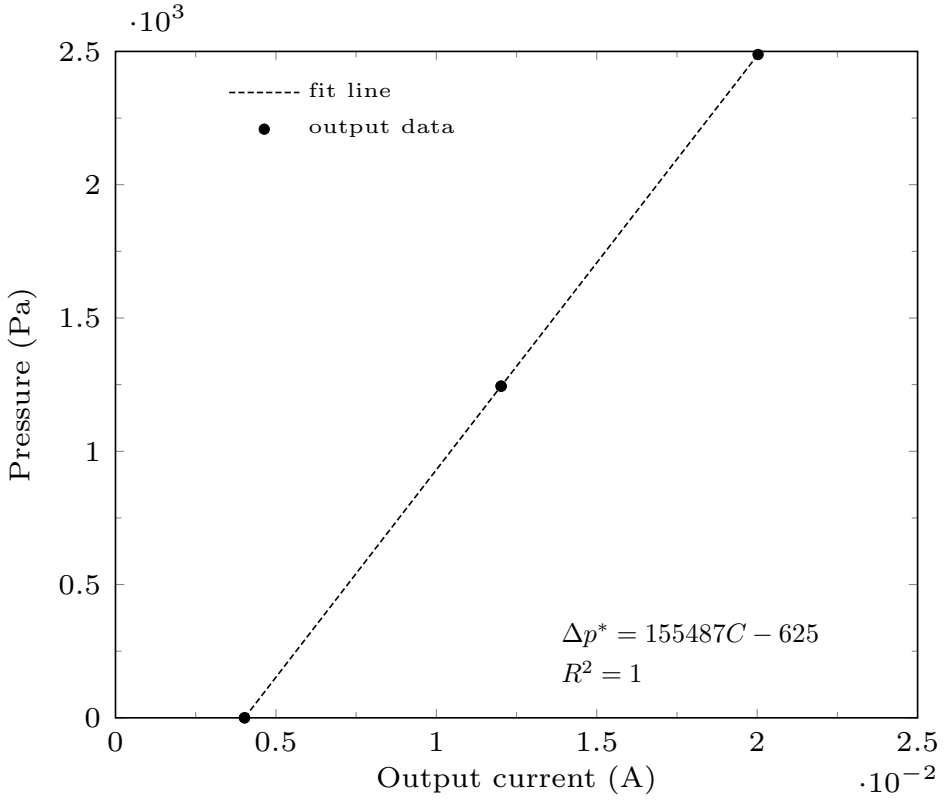

Figure B.4: Calibration data of the differential pressure transmitter, range 0 - 2.5 kPa.

Temperature measurements

A type K thermocouple was used for water temperature measurements with picco data logger. The thermocouple was calibrated in the lab against an accurate thermometer. The calibration data is shown in Figure B.13.

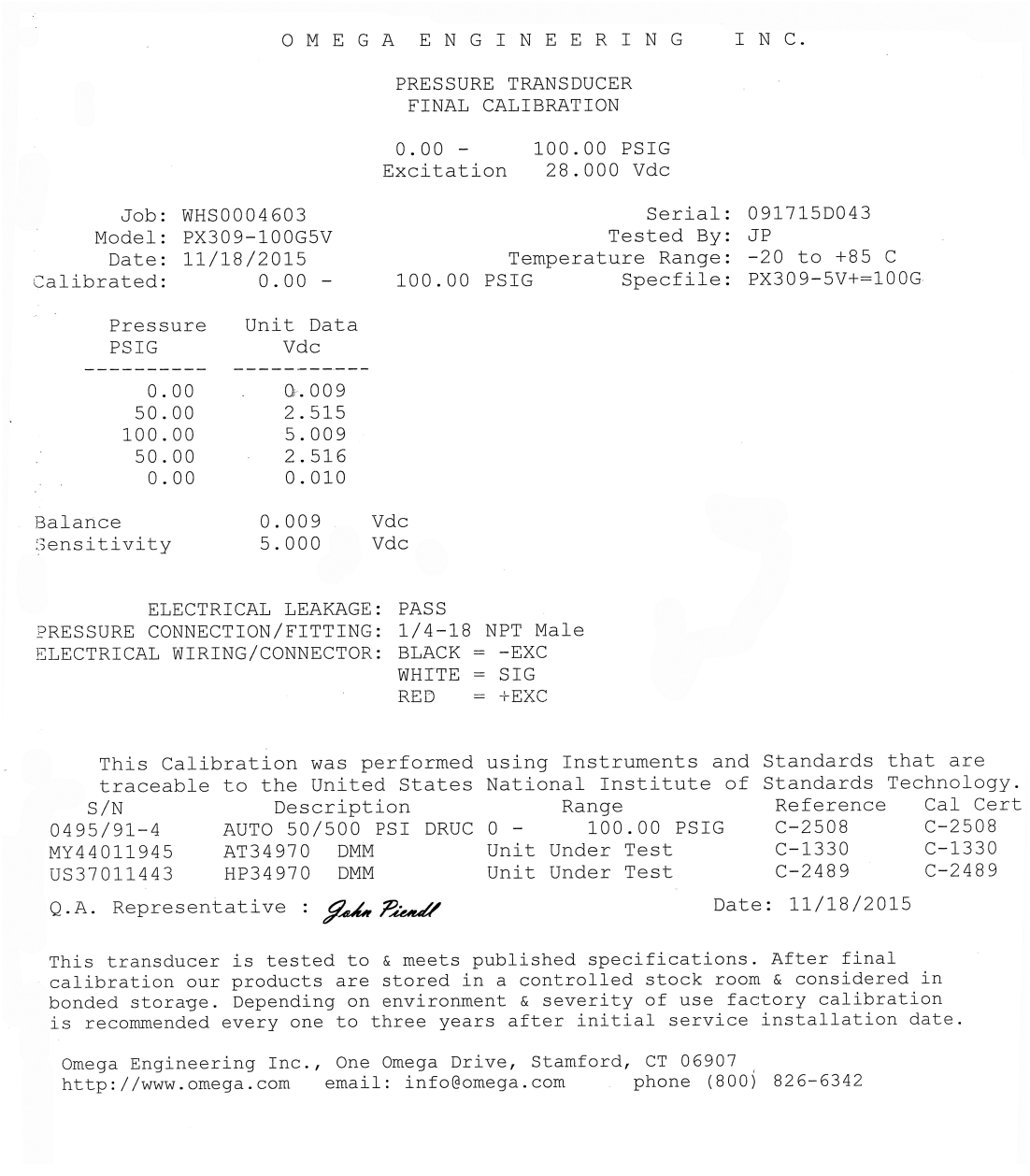

O M E G A E N G I N E E R I N G I N C.

PRESSURE TRANSDUCER
FINAL CALIBRATION

0.00 - 100.00 PSIG
Excitation 28.000 Vdc

Job: WHS0004603 Serial: 091715D043
Model: PX309-100G5V Tested By: JP
Date: 11/18/2015 Temperature Range: -20 to +85 C
Calibrated: 0.00 - 100.00 PSIG Specfile: PX309-5V+=100G

Pressure PSIG	Unit Data Vdc
0.00	0.009
50.00	2.515
100.00	5.009
50.00	2.516
0.00	0.010

Balance 0.009 Vdc
Sensitivity 5.000 Vdc

ELECTRICAL LEAKAGE: PASS
PRESSURE CONNECTION/FITTING: 1/4-18 NPT Male
ELECTRICAL WIRING/CONNECTOR: BLACK = -EXC
WHITE = SIG
RED = +EXC

This Calibration was performed using Instruments and Standards that are traceable to the United States National Institute of Standards Technology.

S/N	Description	Range	Reference	Cal Cert
0495/91-4	AUTO 50/500 PSI DRUC	0 - 100.00 PSIG	C-2508	C-2508
MY44011945	AT34970 DMM	Unit Under Test	C-1330	C-1330
US37011443	HP34970 DMM	Unit Under Test	C-2489	C-2489

Q.A. Representative : John Piendl Date: 11/18/2015

This transducer is tested to & meets published specifications. After final calibration our products are stored in a controlled stock room & considered in bonded storage. Depending on environment & severity of use factory calibration is recommended every one to three years after initial service installation date.

Omega Engineering Inc., One Omega Drive, Stamford, CT 06907
http://www.omega.com email: info@omega.com phone (800) 826-6342

Figure B.5: Calibration certificate of the absolute pressure transducer.

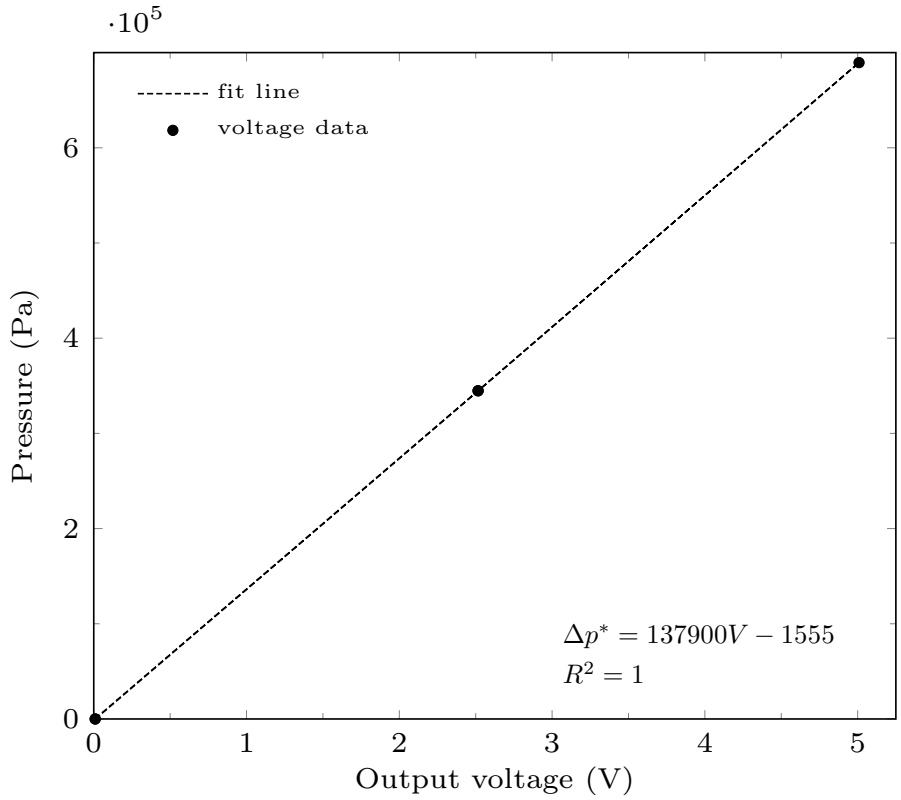

Figure B.6: Calibration data of the absolute pressure transducer, range 0 - 690 kPa.

OMEGA®
An OMEGA Technologies Company
One Omega Drive, Box 4047, Stamford, CT 06907-0047

Flowmeter Calibration Report

Model: FTB-101
Customer:
Customer Addr:
Account:
Cust. PO:
Job Number:
Meter S/N: 170234
Coil: PC24-45S 10MV
Calibration Procedure: WI-760-010
Calibration Tech: BK
Calibration Results: ☑ As Found ☑ As Left

Date: 8/31/2016 Stand 6
Fluid: mil-c
Test range (gpm): 0.348 to 3.519
Linearity (%): +/- 0.82
K' Average (pulses/gal) 16056.289
Lab Temp: 70 °F
Lab RH: 50 %
Customer Re-Calibration Date:

Notes, Adjustments, Interpretations or Repairs:

	Frequency Hz @ 70F	Flowrate GPM	Roshko # Hz/cSt 70F	Strouhal # pul/gal 70F	Fluid Temp Deg. F	Kin. Visc. cSt
1	93.823	0.348	70.321	16169.976	72.099	1.334
2	94.198	0.349	70.607	16173.603	72.107	1.334
3	189.430	0.702	141.983	16187.758	72.102	1.334
4	271.407	1.013	203.523	16069.897	72.163	1.334
5	362.671	1.348	271.713	16141.756	72.045	1.335
6	457.703	1.712	342.894	16045.470	72.039	1.335
7	534.932	2.005	400.682	16007.109	72.017	1.335
8	624.304	2.346	466.832	15965.754	71.798	1.337
9	726.414	2.734	543.245	15944.568	71.812	1.337
10	805.842	3.033	602.660	15940.010	71.815	1.337
11	931.495	3.510	696.628	15924.820	71.815	1.337
12	933.906	3.519	700.129	15925.060	72.128	1.334

Standards Used

Standard #	Description	ReCal Date
TE-652	60 GPM Liquid Calibrator	11/17/2016

The above referenced instrument was calibrated using standards tracible to NIST. The measurement uncertainty are within a best uncertainty of ± 0.05% which represents an expanded uncertainty using a coverage factor, k=2, at a 95% confidence level.

Calibration Report Approval: Mike Hammond (Name) Calibration Engineer (Title) (Signature)

31/08/2016 01:44 PM

Page 1 of 1

Figure B.7: Calibration certificate of the FTB-101 water flow meter.

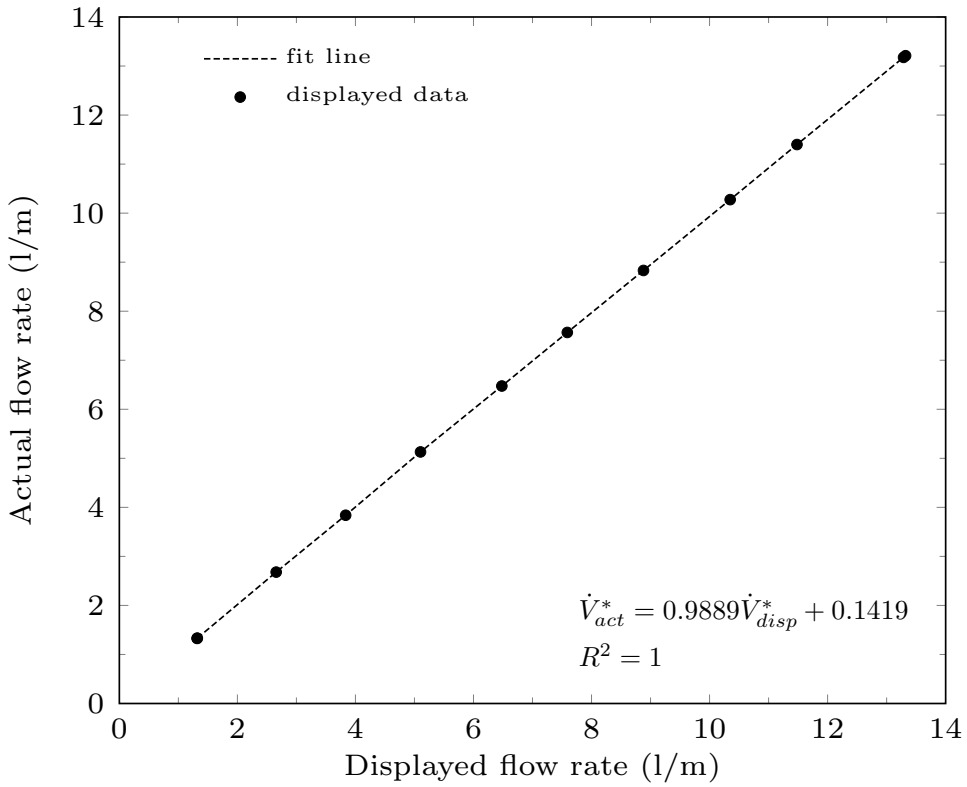

Figure B.8: Calibration data of the FTB-101 water flow meter, range 1.3 - 13.2 LPM.

OMEGA®
An OMEGA Technologies Company
One Omega Drive, Box 4047, Stamford, CT 06907-0047

Flowmeter Calibration Report

Model: FTB-104
Customer:
Account:
Cust. PO:
Job Number:
Meter S/N: 163116
Coil: PC24-45S 130MV

Date: 5/14/2015 Stand 6
Fluid: MIL-C
Test range (gpm): 1.748 to 16.181
Linearity (%): +/- 0.44
K' Average (pulses/gal) 5212.456

	Frequency Hz	Flowrate GPM	Roshko # Hz/cSt 70F	Strouhal # pul/gal 70F	Fluid Temp Deg. F	Kin. Visc. cSt
1	152.428	1.748	115.780	5233.421	73.818	1.317
2	152.526	1.748	115.854	5235.297	73.818	1.317
3	221.901	2.543	168.485	5235.464	73.769	1.317
4	306.938	3.523	233.023	5228.996	73.753	1.317
5	393.286	4.520	298.524	5221.245	73.730	1.318
6	518.103	5.963	392.950	5214.201	73.625	1.319
7	706.994	8.156	536.249	5201.599	73.634	1.319
8	871.419	10.048	660.724	5204.403	73.587	1.319
9	1053.032	12.152	798.216	5200.005	73.553	1.319
10	1221.176	14.113	928.314	5192.354	73.923	1.316
11	1393.280	16.111	1055.140	5189.521	73.431	1.321
12	1399.263	16.181	1063.176	5189.448	73.860	1.316

TEMP=70F HUMIDITY=48%

We certify that all test equipment used in calibrations are traceable to NIST, and that our quality assurance system is certified to ISO 9001-2008.

Operator: BK William C Knauth Final Approval:

Figure B.9: Calibration certificate of the FTB-104 water flow meter.

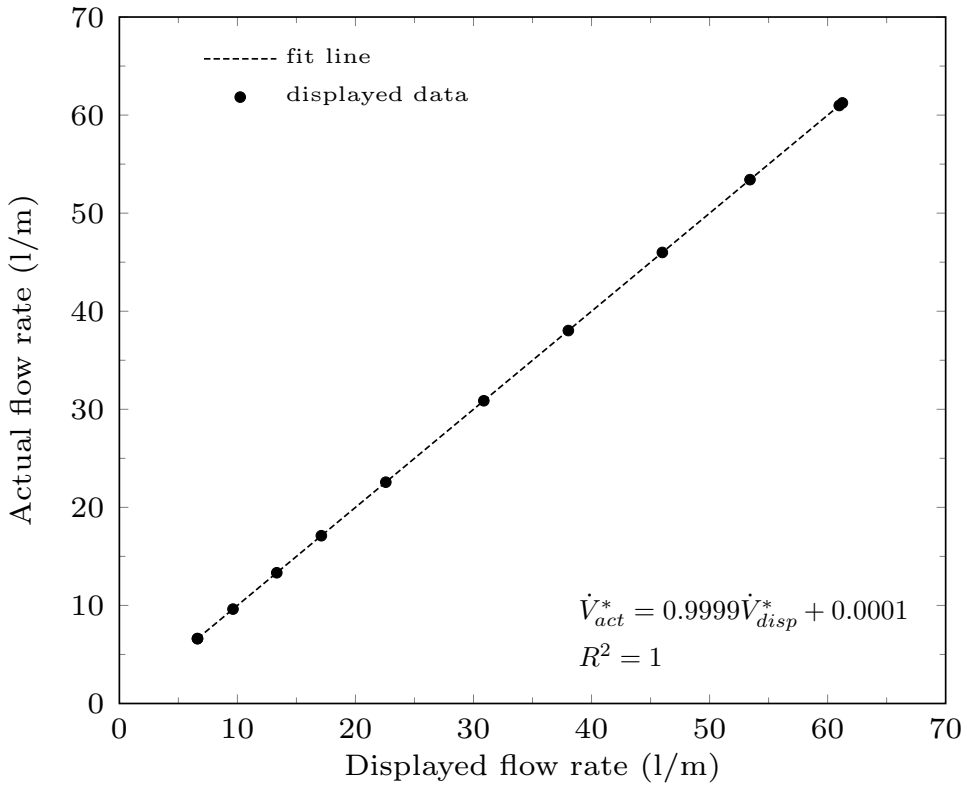

Figure B.10: Calibration data of the FTB-104 water flow meter, range 6.5 - 60 LPM.

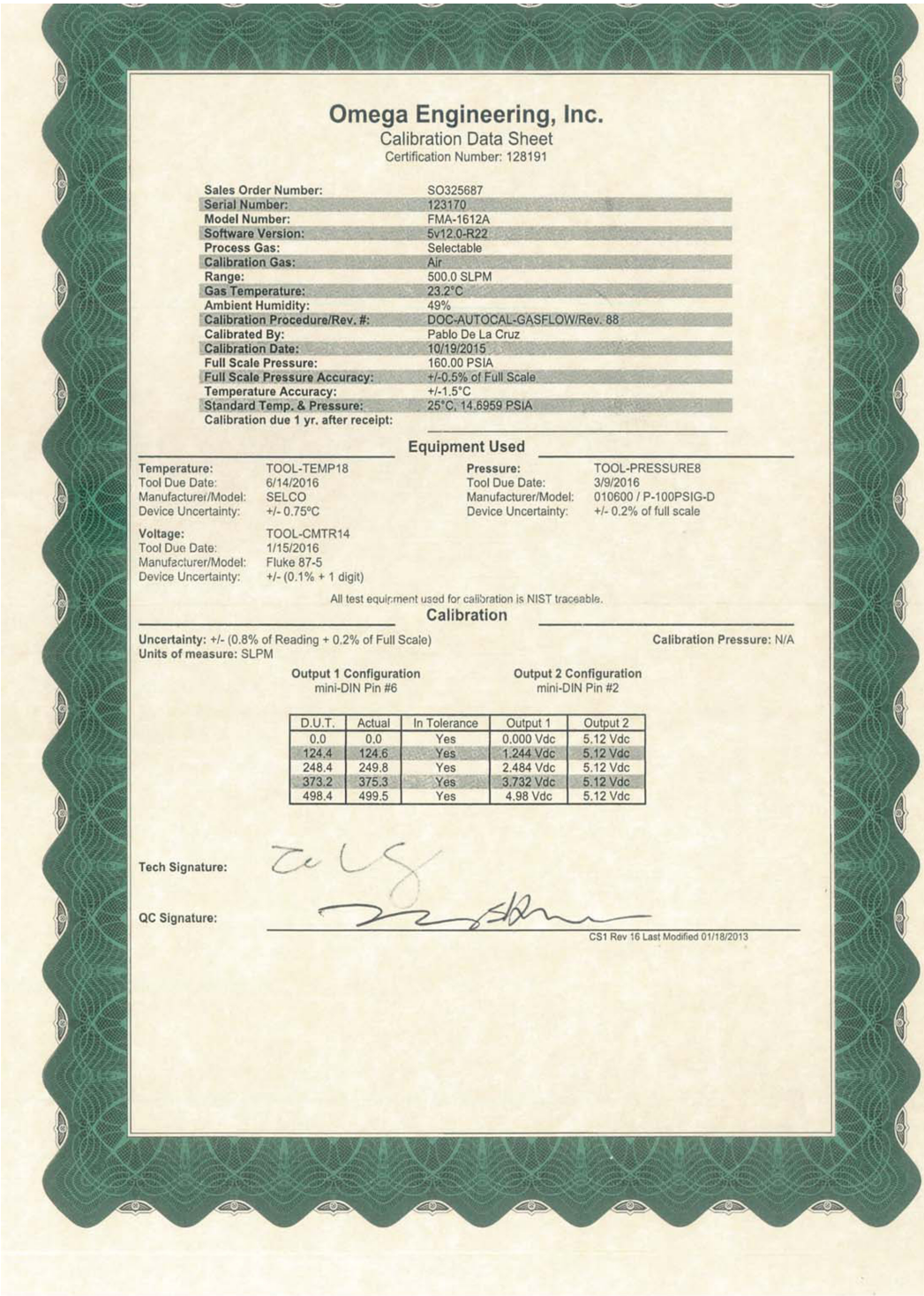

Omega Engineering, Inc.

Calibration Data Sheet

Certification Number: 128191

Sales Order Number:	SO325687
Serial Number:	123170
Model Number:	FMA-1612A
Software Version:	5v12.0-R22
Process Gas:	Selectable
Calibration Gas:	Air
Range:	500.0 SLPM
Gas Temperature:	23.2°C
Ambient Humidity:	49%
Calibration Procedure/Rev. #:	DOC-AUTOCAL-GASFLOW/Rev. 88
Calibrated By:	Pablo De La Cruz
Calibration Date:	10/19/2015
Full Scale Pressure:	160.00 PSIA
Full Scale Pressure Accuracy:	+/-0.5% of Full Scale
Temperature Accuracy:	+/-1.5°C
Standard Temp. & Pressure:	25°C, 14.6959 PSIA
Calibration due 1 yr. after receipt:	

Equipment Used

Temperature:	TOOL-TEMP18	**Pressure:**	TOOL-PRESSURE8
Tool Due Date:	6/14/2016	Tool Due Date:	3/9/2016
Manufacturer/Model:	SELCO	Manufacturer/Model:	010600 / P-100PSIG-D
Device Uncertainty:	+/- 0.75°C	Device Uncertainty:	+/- 0.2% of full scale
Voltage:	TOOL-CMTR14		
Tool Due Date:	1/15/2016		
Manufacturer/Model:	Fluke 87-5		
Device Uncertainty:	+/- (0.1% + 1 digit)		

All test equipment used for calibration is NIST traceable.

Calibration

Uncertainty: +/- (0.8% of Reading + 0.2% of Full Scale) **Calibration Pressure:** N/A

Units of measure: SLPM

Output 1 Configuration mini-DIN Pin #6

Output 2 Configuration mini-DIN Pin #2

D.U.T.	Actual	In Tolerance	Output 1	Output 2
0.0	0.0	Yes	0.000 Vdc	5.12 Vdc
124.4	124.6	Yes	1.244 Vdc	5.12 Vdc
248.4	249.8	Yes	2.484 Vdc	5.12 Vdc
373.2	375.3	Yes	3.732 Vdc	5.12 Vdc
498.4	499.5	Yes	4.98 Vdc	5.12 Vdc

Tech Signature:

QC Signature:

CS1 Rev 16 Last Modified 01/18/2013

Figure B.11: Calibration certificate of air mass flow meter.

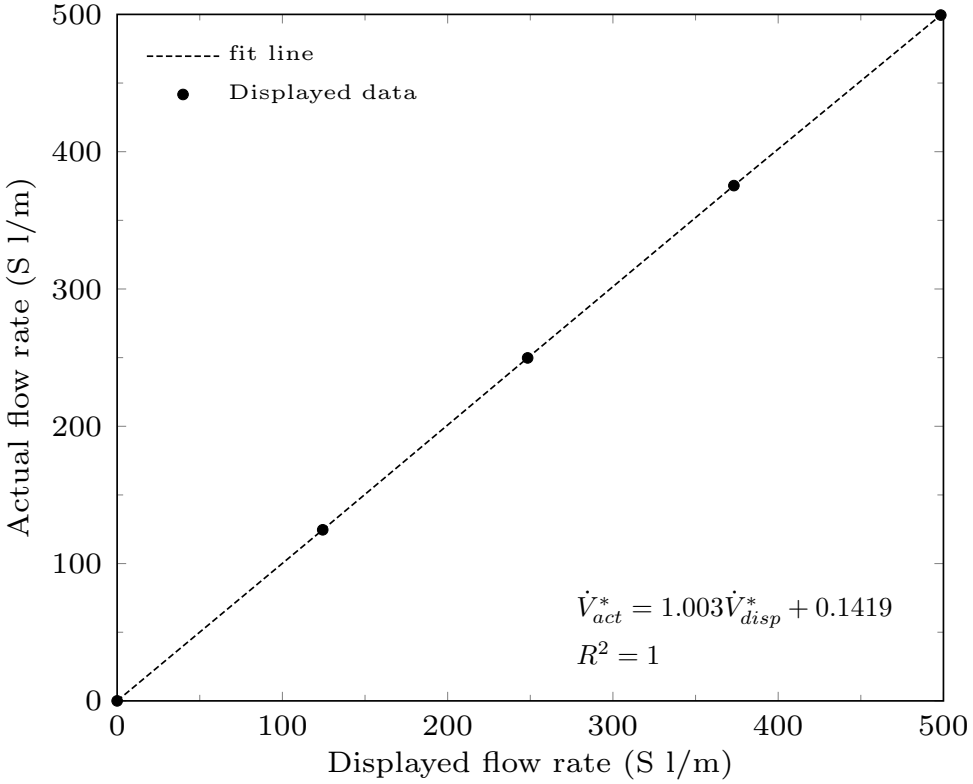

Figure B.12: Calibration data of air mass flow meter, range 2.5 - 500 SLPM.

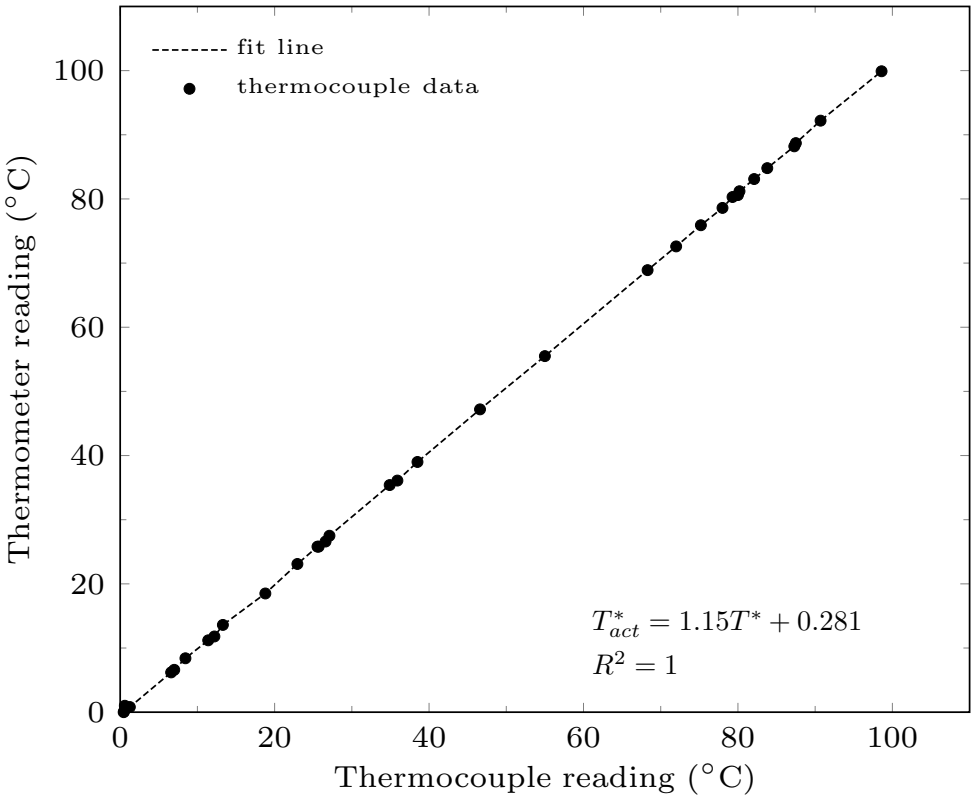

Figure B.13: Calibration data of the type K thermocouple.

Appendix C

Dimensional analysis

A dimensional analysis based on the Π theorem, which was used to obtain the non-dimensional parameters that describe the flow patterns and the two-phase pressure drop, are illustrated in this Appendix.

Dimensional analysis of two-phase flow

The two-phase flow depends on many factors, such as the pipe diameter D^*, fluids densities ρ_k^*, the dynamic viscosities of the fluids μ_k^*, the mass flow rates $\dot{m}_k^*$ (where k=L for water and k=G for air) and the gravitational acceleration g^*. The flow is also dependent on the angle of the pipe inclination with respect to the vertical axis. For mitre elbows, the flow also depends on the flow direction, as explained in Section 6.2. As we operate in regimes at high Reynolds numbers, the effect of the surface tension between air and water is negligible [56, 65].

The number of dimensionless parameters is $\Pi = k' - n$, where k'=8 is the number of the dimensional parameters and n=3 is the number of basic dimensions, i.e. the mass, the length, and the time. It follows that Π=5. As repeating variables, we choose D^*, ρ_L^*, and $\dot{m}_L^*$. We find the following dimensionless parameters:

$$\Pi_1 = \rho_G^* D^{*a} \left(\rho_L^*\right)^b \left(\dot{m}_L^*\right)^c . \tag{C.1}$$

The first parameter, which is obtained by applying a=0, b=-1 and c=0, is the density ratio of the two-phases R:

$$\Pi_1 = R = \frac{\rho_G^*}{\rho_L^*} = \textit{constant in air-water flow.} \tag{C.2}$$

$$\Pi_2 = \mu_{_L}^* D^{*a} \left(\rho_{_L}^*\right)^b \left(\dot{m}_{_L}^*\right)^c . \tag{C.3}$$

The second dimensionless parameter, for a=1, b=0 and c=-1, is the liquid-phase Reynolds number:

$$\Pi_2 = \mathcal{R}e_{_L} = \frac{\dot{m}_{_L}^*}{\mu_{_L}^* D^*} = \frac{\rho_{_L}^* j_{_L}^* D^* \pi}{4\mu_{_L}^*}. \tag{C.4}$$

$$\Pi_3 = \mu_{_G}^* D^{*a} \left(\rho_{_L}^*\right)^b \left(\dot{m}_{_L}^*\right)^c . \tag{C.5}$$

The third non-dimensional parameter, for a=1, b=0 and c=-1, is the gas-phase Reynolds number:

$$\Pi_3 = \mathcal{R}e_{_G} = \frac{\dot{m}_{_G}^*}{\mu_{_G}^* D^*} = \frac{\rho_{_G}^* j_{_G}^* D^* \pi}{4\mu_{_G}^*}. \tag{C.6}$$

$$\Pi_4 = \dot{m}_{_G}^* D^{*a} \left(\rho_{_L}^*\right)^b \left(\dot{m}_{_L}^*\right)^c . \tag{C.7}$$

By applying a=0, b=0 and c=-1, the fourth dimensionless parameter is the mass flow rates ratio:

$$\Pi_4 = \mathcal{M}_{ass} = \frac{\dot{m}_{_G}^*}{\dot{m}_{_L}^*} = \frac{\mu_{_L}^*}{\mu_{_G}^*} \frac{\mathcal{R}e_{_L}}{\mathcal{R}e_{_G}} = \mathcal{M}_u \frac{\mathcal{R}e_{_L}}{\mathcal{R}e_{_G}}. \tag{C.8}$$

$$\Pi_5 = g^* D^{*a} \left(\rho_{_L}^*\right)^b \left(\dot{m}_{_L}^*\right)^c . \tag{C.9}$$

The fifth parameter is defined by using a=5, b=2 and c=-2 as:

$$\Pi_5 = \frac{\dot{m}_{_L}^{*2}}{g^* D^{*5} \rho_{_L}^{*2}} = Fr_{_L}^2. \tag{C.10}$$

Note that the Π_4 parameter found directly from the analysis is Π_4=$\dot{m}_{_G}^*/\dot{m}_{_L}^*$, which can be written as Π_4= $\left(\mu_{_L}^*/\mu_{_G}^*\right) \mathcal{R}e_{_L}/\mathcal{R}e_{_G}$. The Reynolds numbers already belong to the dimensionless group of parameters and therefore the ratio of viscosity $\mathcal{M}_u$ is a more convenient choice for Π_4.

For a specified geometry and flow direction, the flow patterns can therefore be expressed in terms of $\mathcal{R}e_{_L}$, $\mathcal{R}e_{_G}$, $Fr_{_L}, R$, and $\mathcal{M}_u$. For an incompressible and isothermal air-water flow, R and $\mathcal{M}_u$ are constants, and thus flow pattern maps can be obtained in the two-dimensional space ($\mathcal{R}e_{_L}$, $\mathcal{R}e_{_G}$) for a given $Fr_{_L}$.

Dimensional analysis of two-phase pressure drop

A dimensional analysis based on the Π theorem is employed to find the non-dimensional parameters the friction coefficient $\mathcal{C}_{_L}$ and the scaled pressure drop of the elbow $\mathcal{K}_{_L}$ depend on. The flow depends on the diameter D^*, the densities and

the viscosities of the fluids, ρ_k^* and μ_k^*, the mass flow rates $\dot{m}_k^*$ (where k=L for water and k=G for air), and the gravitational acceleration g^*. The flow is also dependent on the angle of the pipe inclination with respect to the vertical axis. For mitre elbows, the flow also depends on the flow direction, that is, whether the vertical pipe is located upstream or downstream of the elbow. The effect of the surface tension between air and water is negligible because the interest is in high-Reynolds-number regimes [56, 65].

The number of dimensionless parameters is Π=$k' - n$, where k'=8 is the number of the dimensional parameters and n=3 is the number of basic dimensions, i.e. the mass, the length, and the time. It follows that Π=5. As repeating variables, D^*, $\rho_{_L}^*$, and $\dot{m}_{_L}^*$ are chosen. We find the following dimensionless independent parameters:

$$\Pi_1 = R = \frac{\rho_{_G}^*}{\rho_{_L}^*} = \textit{constant in air-water flow.} \tag{C.11}$$

$$\Pi_2 = \mathcal{R}e_{_L} = \frac{\dot{m}_{_L}^*}{\mu_{_L}^* D^*} = \frac{\rho_{_L}^* j_{_L}^* D^* \pi}{4\mu_{_L}^*}. \tag{C.12}$$

$$\Pi_3 = \mathcal{R}e_{_G} = \frac{\dot{m}_{_G}^*}{\mu_{_G}^* D^*} = \frac{\rho_{_G}^* j_{_G}^* D^* \pi}{4\mu_{_G}^*}. \tag{C.13}$$

$$\Pi_4 = \mathcal{M}_{ass} = \frac{\dot{m}_{_G}^*}{\dot{m}_{_L}^*} = \frac{\mu_{_L}^*}{\mu_{_G}^*}\frac{\mathcal{R}e_{_L}}{\mathcal{R}e_{_G}} = \mathcal{M}_u \frac{\mathcal{R}e_{_L}}{\mathcal{R}e_{_G}}. \tag{C.14}$$

$$\Pi_5 = \frac{\dot{m}_{_L}^{*\,2}}{g^* D^{*5} \rho_{_L}^{*2}} = Fr_{_L}^2. \tag{C.15}$$

Note that the Π_4 parameter found directly from the analysis is Π_4=$\dot{m}_{_G}^*/\dot{m}_{_L}^*$, which can be written as Π_4=$(\mu_{_L}^*/\mu_{_G}^*)\,\mathcal{R}e_{_L}/\mathcal{R}e_{_G}$. The Reynolds numbers already belong to the dimensionless group of parameters and therefore the ratio of viscosity is a more convenient choice for Π_4. The pressure drop coefficients $\mathcal{C}_{_L}$ scale as:

$$\mathcal{C}_{_L} = \frac{\Delta p_{\text{tp}}^*|_{\text{f}}}{\Delta l^*}\frac{D^{*5}\rho_{_L}^*}{\dot{m}_{_L}^{*\,2}}, \tag{C.16}$$

and

$$\mathcal{K}_{_L} = \Delta p_{\text{tp}}^*|_{\text{e}}\,\frac{D^{*4}\rho_{_L}^*}{\dot{m}_{_L}^{*\,2}}. \tag{C.17}$$